



Skolkovo Institute of Science and Technology

Skolkovo Institute of Science and Technology

OXYGEN REDUCTION REACTION MECHANISM ON METAL OXIDES/CARBON  
COMPOSITE MATERIALS

*Doctoral Thesis*

by

ALEKSANDR KURILOVICH

DOCTORAL PROGRAM IN MATERIALS SCIENCE AND ENGINEERING

Supervisor  
Professor Keith J. Stevenson

Moscow - 2020

© Aleksandr Kurilovich 2020

I hereby declare that the work presented in this thesis was carried out by myself at Skolkovo Institute of Science and Technology, Moscow, except where due acknowledgement is made, and has not been submitted for any other degree.

Candidate (Aleksandr Kurilovich)

Supervisor (Prof. Keith J. Stevenson)

## Abstract

The efficiency of the next-generation energy storage and conversion technologies, such as low-temperature fuel cells, regenerative fuel cells, and metal-air batteries, is highly influenced by the kinetics of the electrocatalytic oxygen reduction reaction (ORR). Its complexity and slow kinetics even on the most active commercial Pt-based catalysts was addressed by extensive research over the last few decades to find cost-effective alternatives. The carbon-supported transition metal oxides (TMO/C) attract significant interest as catalysts for ORR in alkaline media. However, the further optimal catalyst search requires the knowledge of the ORR mechanism in order to be facilitated.

In this work, the ORR mechanism on TMO/C composite materials was targeted by the multiscale modeling approach comprising the experimental data, macroscale, and *ab initio* calculations. The first insights on the ORR mechanism were obtained within the rationalization of the pronounced difference of ORR and hydroperoxide reduction/oxidation reactions (HPRR/HPOR) on  $\text{Mn}_2\text{O}_3$  and  $\text{MnOOH}$ . The possibility of the outer-sphere regime for the first two electron transfer steps was shown. The observed limitations on each level of description led the study to the elucidation of the particular aspects of the multiscale modeling approach. As such, the next part was devoted to studying the connection between the macroscale simulations and experimental data they aim to reproduce. The required level of complexity of the ORR mechanism, which is capable to reproduce the experimental data (ORR, HPRR/HPOR on  $\text{La}_{1-x}\text{Sr}_x\text{CoO}_{3-\delta}$  ( $0 < x < 1$ ) /Vulcan XC-72, nitrogen-doped carbons) was estimated. Only the rather complicated model with the  $\text{O}_2$  spillover described the complete experimental dataset. It led to the conclusion that the uncertainty arising from experimental data and its propagation within the multiscale modeling approach are crucial to quantify in order to find the accessible level of detailing for the ORR mechanism based on the accuracy of simulation approaches and diversity of the experimental data. The last two chapters of the thesis addressed this issue by the construction of the quantitative framework for ORR mechanism selection and improvement of the macroscale models consistency with the elementary mechanisms addressed by *ab initio* calculations.

## Publications

- 1 A.A. Kurilovich, K. J. Stevenson, “Oxygen Reduction Reaction Mechanism Study Via Mean-Field Microkinetic Modeling and Uncertainty Quantification of Model Parameters,” *ECS Trans.*, vol. 97, no. 7, pp. 757-762, Jul. 2020, doi: 10.1149/09707.0757ecst.
- 2 A. A. Kurilovich, C. T. Alexander, E. M. Pazhetnov, and K. J. Stevenson, “Active learning-based framework for optimal reaction mechanism selection from microkinetic modeling: a case study of electrocatalytic oxygen reduction reaction on carbon nanotubes,” *Phys. Chem. Chem. Phys.*, vol. 22, no. 8, pp. 4581–4591, 2020, doi: 10.1039/C9CP06190H.
- 3 J. T. Mefford, A. A. Kurilovich, J. Saunders, W. G. Hardin, A. M. Abakumov, R. P. Forslund, A. Bonnefont, S. Dai, K. P. Johnston, K. J. Stevenson, “Decoupling the roles of carbon and metal oxides on the electrocatalytic reduction of oxygen on La<sub>1-x</sub>Sr<sub>x</sub>CoO<sub>3-δ</sub> perovskite composite electrodes,” *Phys. Chem. Chem. Phys.*, vol. 21, no. 6, pp. 3327–3338, 2019, doi: 10.1039/C8CP06268D.
- 4 V. A. Nikitina, A. A. Kurilovich, A. Bonnefont, A. S. Ryabova, R. R. Nazmutdinov, E. R. Savinova, G. A. Tsirlina, “ORR on Simple Manganese Oxides: Molecular-Level Factors Determining Reaction Mechanisms and Electrocatalytic Activity,” *J. Electrochem. Soc.*, vol. 165, no. 15, pp. J3199–J3208, Oct. 2018, doi: 10.1149/2.0261815jes.

## **Acknowledgements**

I would like to thank my supervisor Keith Stevenson for his mentorship and support and Victoria Nikitina for the valuable discussions and introducing to the field of electrocatalysis.

I would also like to thank my collaborators and the people, who helped me during the work on thesis through the discussions, support, and teaching: Caleb Alexander, Tyler Mefford, Antoine Bonnefont, Elena Savinova, Galina Tsirlina, Egor Pazhetnov, Sergey Matveev, Andriy Zhugayevych, Artem Nikitin, Sergey Porokhin, and Elena Kurilovich.

## Table of Contents

Abstract.....	3
Publications.....	4
Acknowledgements.....	5
Table of Contents.....	6
List of Symbols, Abbreviations.....	8
List of Figures.....	10
List of Tables.....	12
Chapter 1. Introduction.....	13
Chapter 2. Literature review. Multiscale modeling approach for the oxygen reduction reaction.....	18
2.1. Oxygen reduction reaction.....	18
2.1.1. Fuel cells as energy storage and conversion devices.....	18
2.1.2. ORR mechanism.....	21
2.1.2.1. ORR pathways in acidic media.....	21
2.1.2.1.1. Carbon materials.....	22
2.1.2.1.2. Platinum-based materials.....	22
2.1.2.2. ORR pathways in alkaline media.....	23
2.1.2.2.1. Carbon materials.....	24
2.1.2.2.2. Platinum-based materials.....	25
2.1.2.2.3. Transition metal oxides.....	26
2.1.3. Summary.....	29
2.2. Multiscale modeling approach.....	30
2.2.1. Mean-field microkinetic modeling approach.....	31
2.2.1.1. Mathematical description.....	31
2.2.1.2. Approximations.....	34
2.2.1.3. Charge-transfer step description.....	36
2.2.1.4. Simulation of a rotating ring-disk electrode.....	37
2.2.1.5. History and applications.....	39
2.2.2. Density functional theory.....	42
2.2.2.1. The aspects of DFT study of ORR mechanism.....	44
2.2.3. Uncertainty quantification.....	48
2.2.3.1. Uncertainty sources classification.....	48
2.2.3.2. Forward uncertainty propagation problem.....	50
2.2.3.3. Inverse uncertainty propagation problem.....	52
2.2.4. Summary.....	54
2.3. Thesis outline.....	55
Chapter 3. Multiscale Modeling for ORR Mechanism on Manganese Oxides.....	57
3.1. Materials and methods.....	57
3.1.1. Chemicals.....	57
3.1.2. Electrochemical characterization.....	58
3.2. Theoretical basis.....	58
3.2.1. Periodic DFT calculations.....	58

3.2.2. Cluster DFT calculations .....	62
3.2.3. Mean-field microkinetic modeling details .....	63
3.3. Results and discussion .....	64
3.4. Conclusions.....	77
Chapter 4. Assessment of ORR Mechanism Complexity for Decoupling the Roles of Carbon and Metal Oxides on $\text{La}_{1-x}\text{Sr}_x\text{O}_{3-\delta}$ / C Composite Materials Within the MF-MKM Approach.....	79
4.1. Materials and methods .....	79
4.1.1. Chemicals.....	79
4.1.2. Electrochemical characterization .....	80
4.2. Theoretical basis .....	81
4.3. Results and discussion .....	88
4.4. Conclusions.....	103
Chapter 5. Uncertainty Quantification for Quantitative ORR Mechanism Selection.....	105
5.1. Materials and Methods.....	106
5.1.1. Chemicals.....	106
5.1.2. Carbon Nanotube Synthesis.....	106
5.1.3. Surface Area Characterization .....	107
5.1.4. Material Characterization.....	107
5.1.5. Electrochemical Characterization .....	107
5.2. Theoretical Basis.....	109
5.2.1. Experimental error calculation.....	109
5.2.2. Modeling details.....	110
5.2.3. Model equations.....	112
5.3. Results and Discussion .....	116
5.4. Conclusions.....	132
Chapter 6. Model Form Uncertainty Reduction Based on RDS Approximation for the Effective Multi-Electron Steps. ....	134
6.1. Materials and methods .....	134
6.1.1. Experimental data. ....	134
6.1.2. Modeling details.....	135
6.2. Results and Discussion .....	136
6.3. Conclusions.....	140
Chapter 7. Conclusions and Future Directions .....	141
Bibliography .....	145

## List of Symbols, Abbreviations

ORR – oxygen reduction reaction  
OER – oxygen evolution reaction  
HPRR – hydroperoxide reduction reaction  
HPOR – hydroperoxide oxidation reaction  
MF-MKM – mean-field microkinetic modeling  
KMC – kinetic Monte-Carlo  
DFT – density functional theory  
CFD – computational fluid dynamics  
ODE – ordinary differential equation  
PDE – partial differential equation  
LDA – local density approximation  
GGA – generalized gradient approximation  
PBE – Perdew-Burke-Erzenhof functional  
RPBE – revised Perdew-Burke-Erzenhof functional  
PW91 – Perdew-Wang 91 functional  
PW – plane-wave basis  
ZPE – zero-point energy correction  
PAW – projector-augmented wave method  
TST – transition state theory  
ET – electron transfer  
PFR – plug-flow reactor  
CSTR – continuous-flow stirred tank reactor  
PCE – polynomial chaos expansion  
TPE – Tree-structured Parzen estimator algorithm  
PDF – probability density function  
MCMC – Markov chain Monte Carlo  
BET – Brunauer-Emmett-Teller analysis  
BJH – Barrett-Joyner-Halenda method

XRD – X-ray diffraction  
XPS – X-ray photoelectron spectroscopy  
PGM – platinum group metal  
TMO – transition metal oxide  
LCO –  $\text{LaCoO}_3$   
LSCO –  $\text{La}_{1-x}\text{Sr}_x\text{CoO}_{3-\delta}$   
VC – Vulcan carbon XC-72  
NC – mesoporous nitrogen-doped carbon  
GC – glassy carbon  
CNTs – multiwalled carbon nanotubes  
PEMFC – proton-exchange membrane fuel cell  
AEMFC – anion-exchange membrane fuel cell  
AFC – alkaline fuel cell  
RDE – rotating disk electrode  
RRDE – rotating ring-disk electrode  
RHE – reversible hydrogen electrode  
CV – cyclic voltammogram  
MSE – mean-squared error  
CHE – computational hydrogen electrode  
RDS – rate-determining step  
PDS – potential-determining step

## List of Figures

Figure 1.1 .....	13
Figure 1.2 .....	16
Figure 2.1 .....	20
Figure 2.2 .....	26
Figure 2.3 .....	44
Figure 2.4 .....	46
Figure 2.5 .....	47
Figure 3.1 .....	64
Figure 3.2 .....	65
Figure 3.3 .....	67
Figure 3.4 .....	70
Figure 3.5 .....	72
Figure 3.6 .....	73
Figure 3.7 .....	74
Figure 3.8 .....	76
Figure 4.1 .....	89
Figure 4.2 .....	90
Figure 4.3 .....	90
Figure 4.4 .....	92
Figure 4.5 .....	94
Figure 4.6 .....	96
Figure 4.7 .....	98
Figure 4.8 .....	99
Figure 4.9 .....	100
Figure 4.10 .....	101
Figure 5.1 .....	116
Figure 5.2 .....	117
Figure 5.3 .....	118

Figure 5.4 .....	120
Figure 5.5 .....	121
Figure 5.6 .....	122
Figure 5.7 .....	123
Figure 5.8 .....	125
Figure 5.9 .....	126
Figure 5.10 .....	128
Figure 5.11 .....	129
Figure 5.12 .....	130
Figure 5.13 .....	131
Figure 6.1 .....	135
Figure 6.2 .....	137
Figure 6.3 .....	138
Figure 6.4 .....	139

## List of Tables

Table 2.1 .....	19
Table 2.2 .....	40
Table 3.1. ....	61
Table 3.2 .....	62
Table 3.3 .....	67
Table 4.1 .....	86
Table 5.1 .....	115

## Chapter 1. Introduction

The progress has been always associated with the growth in energy generation demand. Being fulfilled with the traditional fossil fuel-based technologies, it is unavoidably leading to environmental problems such as air pollution and greenhouse gas production (see Figure 1.1). According to the International Energy Agency's Global Energy Review 2020 [1], the total CO<sub>2</sub> emissions in 2020 are expected to be 30.6 Gt.

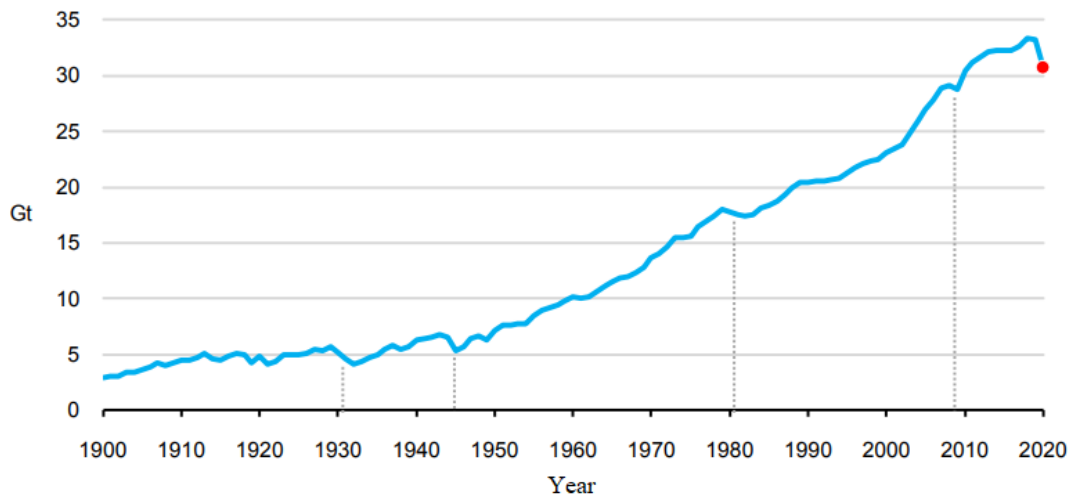


Figure 1.1 Global energy-related CO<sub>2</sub> emissions [1].

CO<sub>2</sub> emission should be reduced to less than 20 Gt by 2030 in order to prevent the major negative climate changes [2]. The temporal decrease by 8% is observed in CO<sub>2</sub> emissions due to the ~4-6% lowered energy demand compared with 2019 because of the pandemic situation in the world. It is correlated with the decrease in the coal, oil, and natural gas consumption by 8, 5, and 2% respectively (Q1 2020 vs. Q1 2019). However, the long term trends for energy demand growth are unlikely to change. The transport applications have a huge share of ~30% for global CO<sub>2</sub> emissions [3]. Therefore, a special effort should be made to replace the combustion engine-based technology with more environmentally friendly alternatives. The low-temperature fuel cell technology [4], typically operating on hydrogen fuel, can be used to address this problem. It provides the generation of the electric energy with high efficiency of 40-80% and the lower or absent emission of hazardous

substances, such as SO<sub>2</sub>, NO<sub>x</sub>, CO, and CO<sub>2</sub>, being compared with the combustion engines operating on the fossil fuels. CO<sub>2</sub> is generated in the full lifecycle of hydrogen production/consumption, as it is mainly produced from the fossil fuels. However, its amount is significantly lower than that for production/combustion lifecycle of gasoline, diesel, and natural gas fuels [5]. Nevertheless, the further optimization of fuel cell efficiency is required, as it indirectly reduces the amount of generated CO<sub>2</sub> per mile through the lowered consumption of hydrogen fuel.

One of the major bottlenecks for commercial application of low-temperature fuel cells and other promising energy storage and conversion technologies (e.g. regenerative fuel cells and metal-air batteries) is the sluggish kinetics of cathodic oxygen reduction reaction (ORR) even on the most active Pt group-based catalysts together with their expensiveness. This issue was addressed by extensive research over the last few decades. The transition metal oxide (TMO) materials attract significant interest as a cost-efficient alternative for ORR electrocatalysis in alkaline media. Due to the low electronic conductivity, they are usually intermixed with the carbon material to provide good electric contact. The complexity of the ORR on TMO/C catalysts is further increased by the fact that the carbon is active for ORR electrocatalysis in alkaline media. Given the variety of the TMO materials and approaches to tune their catalytic activity, one needs to evaluate the factors which determine it. In order to do it, the knowledge about the ORR pathway on the catalyst surface is needed. It is worth noting that the ORR mechanism in alkaline media is far from being well-understood even on single-crystal metal surfaces [6], while it can be even more complex on TMO/C. It has been suggested in several works, that the rate-limiting step for the ORR in alkaline media is the first step of charge transfer to the O<sub>2</sub> molecule [7], [8]. However, even the mechanism of the first electron transfer to O<sub>2</sub> (outer-sphere or inner-sphere) is still under debate.

The first insight on the ORR mechanism can be gained from the high-quality experimental data (most often obtained using the rotating ring-disk electrode (RRDE) technique). It can give some ideas on the reaction steps and the involvement of hydrogen peroxide (HO<sub>2</sub><sup>-</sup> in alkali) as an intermediate species of the reaction. A great deal of

experimental work has been reported in this area, and numerous reaction mechanisms have been suggested. The major problem is that multiple mechanisms demonstrating a similar level of agreement can be proposed for a given set of experimental data. It is impossible to formulate solid conclusions on the reaction pathways using experimental data and basic chemical intuition alone for the multistep ORR reaction, as the only reaction intermediate reliably detected is the hydrogen peroxide.

A higher level of reliability for the reaction mechanism can be achieved in the framework of the mean-field microkinetic modeling (MF-MKM) approach. In this approach, the data is fit by the microkinetic model to determine a set of model parameters, such as rate constants of the key proposed reaction steps. However, the proposed reaction steps are usually not the elementary ones but comprise the combination of the elementary steps. Therefore, further specification is required to refine the microkinetic model.

For such detailed investigations, one can use molecular modeling methods. As relatively large ensembles should be modeled to mimic the reaction centers on an oxide surface, density functional theory methods (DFT) are most typically applied to address the adsorption of the intermediates and to calculate the reaction activation barriers. The most popular approach which can be used to obtain the geometries of surfaces covered with adsorbates is periodic DFT. This powerful methodology allows computing free energies of the catalytic surfaces, which are represented by relatively large supercells (100 – 500 atoms). It is also possible to include the effects of pH and adsorbate coverage in this type of calculations. However, computing activation free energies for the elementary reactions involving the charge transfer is problematic in the framework of periodic DFT calculations. Therefore, the Gibbs free energy changes for the proposed elementary steps are usually calculated without the consideration of activation barriers. Unfortunately, such an approach can only provide rough qualitative conclusions on the nature of the limiting step [9], [10].

On the other hand, calculations based on the cluster representation (10 – 100 atoms) can be used to assess the reaction activation barriers for electron transfer steps. Rate constants of the respective elementary reactions can be evaluated and compared, providing information on the preferential steps in the reaction pathways. Despite cluster

representation has its own shortcomings (e.g. artificial border effects), it enables a more detailed study of the electron transfer steps (i.e. by accessing their kinetics), comparing to the periodic DFT methods. Due to the system size limitations, the most advantageous approach should include computing activation barriers on oxide surfaces by cluster DFT, with the geometry evaluated in parallel computations by periodic DFT. This would ensure the beneficial combination of the two computational approaches described.

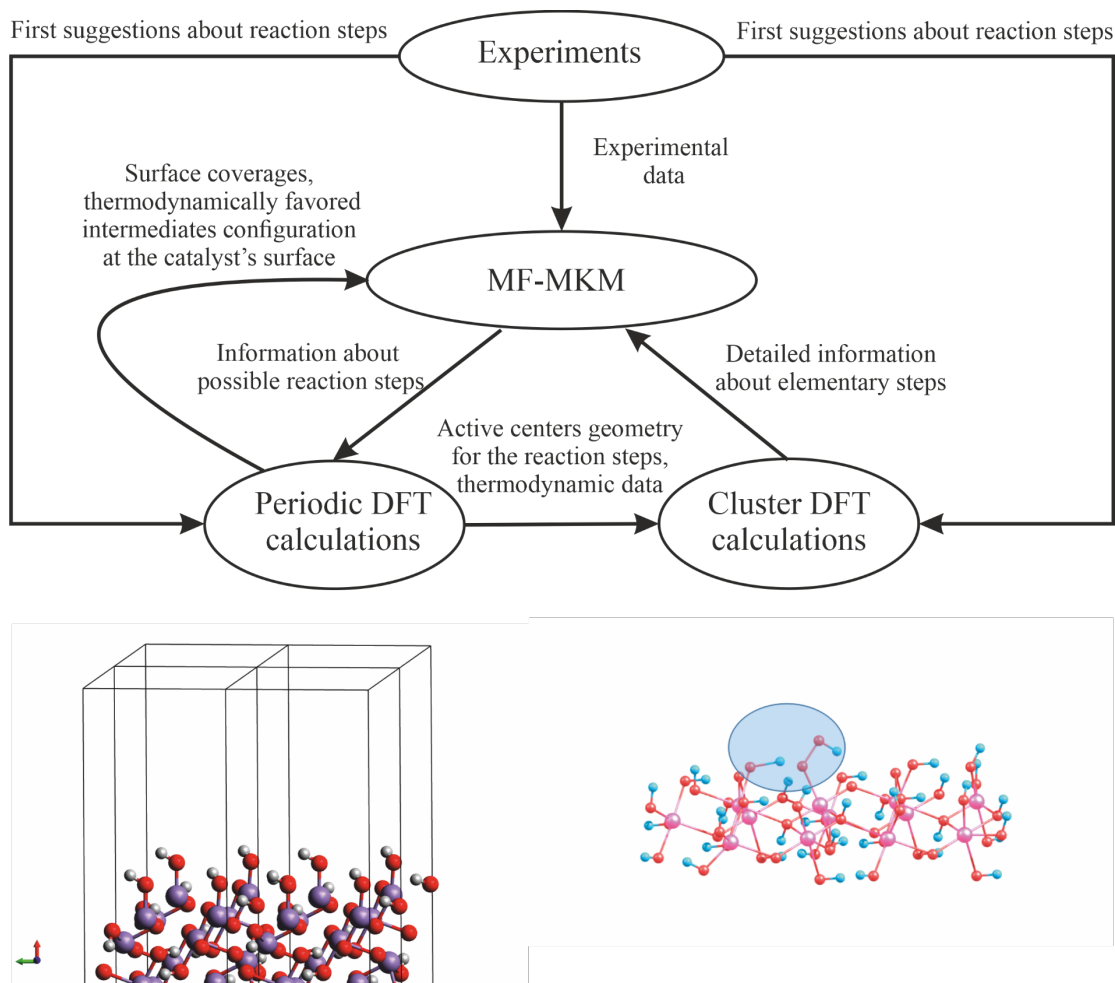


Figure 1.2 Multiscale modeling approach for ORR pathway evaluation.

Given the limitations of the computational and experimental approaches, a more reliable understanding of the complex reaction mechanisms is only possible when *ab initio* computations and MF-MKM approach are combined in a self-consistent data treatment

procedure and applied to a set of reliable experimental data within the multiscale modeling approach (Figure 1.2). The multiscale modeling approach is a powerful semi-quantitative tool for the elucidation of complex electrocatalytic reaction mechanisms, but it inherits the uncertainties of approximations from all the embedded methods. They set up the maximum level of details this approach can provide for the reaction mechanism. The achievable detailing level should be determined quantitatively to understand what predictive capability the elucidated ORR mechanism has together with its estimated macroscale/microscale parameters. It requires the modification of a multiscale modeling approach by the quantification of uncertainties arising from all sources and uncertainty propagation between them.

This work is aimed to elucidate the ORR mechanism on TMO/C catalysts in alkaline media using the multiscale modeling approach. The additional efforts are dedicated to the study of the uncertainties propagation arising from experimental errors. Its quantitative treatment is crucial to determine the level of insights that can be experimentally verified, thus providing better coupling of the methods within the multiscale modeling approach. These results should facilitate further search for more active and cost-efficient ORR catalysts, which would enhance the performance of related energy storage and conversion devices. It should help to solve the problem of huge CO<sub>2</sub> emissions from the transport applications, as efficient low-temperature fuel cells should reduce the hydrogen consumption per mile and thus the overall CO<sub>2</sub> generation.

## **Chapter 2. Literature review. Multiscale modeling approach for the oxygen reduction reaction**

### **2.1. Oxygen reduction reaction**

The ORR is the crucial process in the low-temperature fuel cells, regenerative fuel cells, and metal-air batteries. Its sluggish kinetics even on the most active Pt-containing catalysts is the major source of efficiency losses, which calls for the development of cost-effective and durable catalysts for ORR. This section reviews the principles and types of energy storage and conversion devices which depend on the ORR, the progress in ORR mechanism study, and the current challenges in this process.

#### *2.1.1. Fuel cells as energy storage and conversion devices*

The fuel cell produces the electricity by coupled oxidation of the fuel at the anode (e.g. H<sub>2</sub>) and reduction of the oxidant at the cathode (e.g. O<sub>2</sub>). The anodic and cathodic half-reactions are separated by the electrolyte which has only ionic but not electronic conductivity. The electrons generated on the anode are forced to flow through the external circuit, thus generating the direct current.

Fuel cells have the following advantages in addition to the abovementioned ones: (i) Silent operation and potential mechanical durability due to the lack of the moving parts; (ii) Independent scaling of power (fuel cell size) and capacity (fuel-tank size); (iii) Quick recharge by the refueling. Therefore, they can operate in the wide power range for the portable, automotive, and immobile grid applications.

The drawbacks of fuel cells addressed by the extensive research are (i) High cost, e.g. due to the use of expensive catalysts; (ii) Mediocre gravimetric and volumetric power densities, in comparison with batteries and combustion engines; (iii) Low volumetric energy density of the hydrogen fuel and its storage complications, (iv) Difficulties in the direct use of alternative fuels (e.g. formic acid, methanol, gasoline), which are leading to the necessity of their reforming; (v) Susceptibility to the environmental poisons; (vi) Limited operational temperature compatibility; (vii) Durability issues during the start-stop cycling [11].

Several types of fuel cells exist, depending on the fuel and electrolyte type (see Table 2.1). The fuel cells operating at the high temperature, such as solid oxide fuel cell (SOFC), molten carbonate fuel cell (MCFC), and phosphoric acid fuel cell (PAFC), are utilized for the stationary applications. The transport, portable, and small-scale stationary applications require low operating temperature and can be fulfilled by proton-exchange membrane fuel cells (PEMFC), alkaline fuel cells (AFC), and emerging anion-exchange membrane fuel cells (AEMFC).

Table 2.1 Properties of major fuel cell types

	PEMFC	AFC	AEMFC	PAFC	MCFC	SOFC
Electrolyte	Polymer membrane	Liquid KOH (immobilized)	Alkaline anion exchange membrane	Liquid H <sub>3</sub> PO <sub>4</sub> (immobilized)	Molten carbonate	Ceramic
Charge carrier	H <sup>+</sup>	OH <sup>-</sup>	OH <sup>-</sup>	H <sup>+</sup>	CO <sub>3</sub> <sup>-</sup>	O <sup>2-</sup>
Operating temperature	<90 °C	60-250 °C	<80 °C	180-210 °C	650 °C	600-1000 °C
Catalyst	Pt	Pt	Pt, PGM-free catalysts	Pt	Ni	Perovskites, (ceramic)
Fuel compatibility	H <sub>2</sub> , CH <sub>3</sub> OH	H <sub>2</sub>	H <sub>2</sub> , CH <sub>3</sub> OH, C <sub>2</sub> H <sub>6</sub> O	H <sub>2</sub>	H <sub>2</sub> , CH <sub>4</sub>	H <sub>2</sub> , CH <sub>4</sub> , CO

The principal component of the single fuel cell in the fuel cell stack is a membrane electrode assembly (MEA). MEA consists of electrolyte, anodic and cathodic active layers, and gas diffusion layers (GDL). Electrolyte, which is either a cation/anion exchange membrane or flowing/immobilized electrolyte, separates the anodic and cathodic active layers. They usually have a thickness of 10-100 $\mu$ m and comprise the highly dispersive nanoparticles of active catalyst materials on the stable porous support. The latter prevents the sintering of the catalyst nanoparticles, provides electronic connection and gas fuel

transport to the triple-phase boundaries (TPB), which are the reaction sites in the fuel cells. The anode/electrode layer thickness is optimized to provide the compromise between the gas diffusion; catalyst utilization, and catalyst loading.

The catalyst layer is usually supported by the thicker 100-400 $\mu\text{m}$  gas diffusion layer (GDL), which provides the mechanical strength, collects the current, allows the gas fuel transport to the catalytic layer, and also prevents the flooding by the liquid water removal from the low-temperature fuel cells. For the PEMFC of “electrode Los-Alamos Type”, the microporous layer is inserted between the GDL and the electrode layer to reduce the contact resistance and improve the liquid water wicking.

One can see the schemes of PEMFC and AEMFC in Figure 2.1

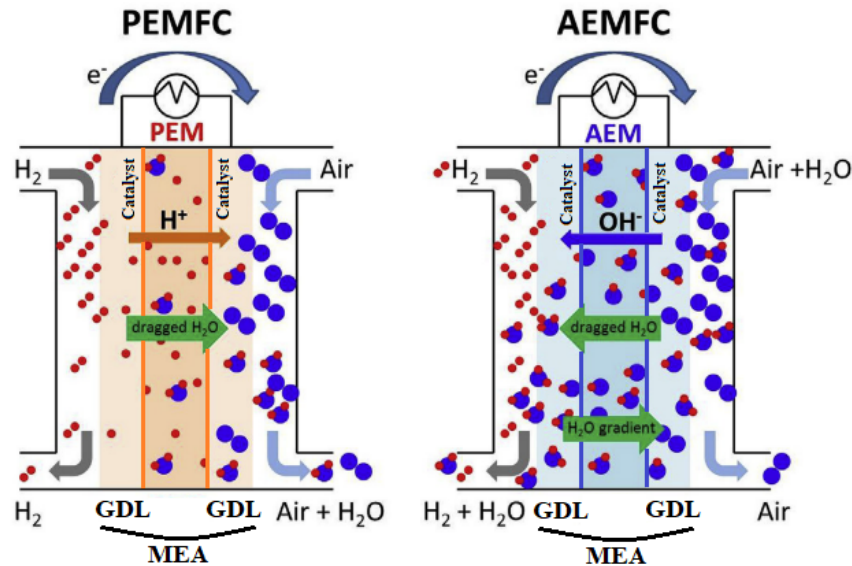


Figure 2.1 Schematic representation of AEMFC and PEMFC. [12]

Nowadays the PEMFC is the most widely used technology, due to the availability of high-quality proton exchange membranes, e. g. Nafion. However, acidic media and the sluggish oxygen reduction reaction (ORR) on the cathode require the expensive platinum group metal (PGM) catalysts, which hampers their commercial applications. The lifetime (the time for 10% of power loss) of PEMFC stack under the ideal operating conditions (constant-load operation, 100% relative humidity, 75 °C) is ~40000h. However, in real-

world applications, the lifetime is reduced mainly due to the membrane and catalytic layer degradation. The mechanisms for the latter are: (i) Pt nanoparticle growth; (ii) Pt dissolution at intermediate potentials; (iii) Corrosion of carbon-based support [13].

The AFC enables the use of the cheaper PGM-free catalysts, which are stable in the alkaline environment. The KOH electrolyte (flowing or immobilized in the asbestos separator) is also cheaper than the proton exchange membranes. Additionally, the ORR has faster kinetics in alkaline than in acidic media. It is one of the oldest commercial fuel cell designs, with the first AFC developed by Francis Bacon in 1958 for the Apollo spacecraft mission. However, the practical applicability of AFC is limited by its extremely low tolerance to CO<sub>2</sub>. Even the atmospheric level of CO<sub>2</sub> carbonizes the electrolyte and irreversibly forms the solid precipitates. This process gradually decreases the electrolyte pH over time and blocks the porous electrodes.

The AEMFC is an emerging technology, significantly improved over the last decade [12], [14], [15]. It is aiming to solve the CO<sub>2</sub> low tolerance issue by the use of anion exchange membrane (AEM) as the electrolyte, thus removing the carbonate precipitation. Despite the many challenges to overcome (e.g. the development of active and stable PGM-free catalyst, AEMs with robust mechanical properties and high anion conductivity, and water management issues [14]), the AEMFC is a promising cost-effective alternative for the PEMFC.

To sum up, one of the critical points for all major types of low-temperature fuel cells is the development of the durable cost-effective catalyst for the ORR. This also applies to the other storage and conversion devices, such as regenerative fuel cells [16], [17] and metal-air batteries [18].

### *2.1.2. ORR mechanism*

#### *2.1.2.1. ORR pathways in acidic media.*

Two general ORR pathways exist in acidic solutions:

- 1) Direct 4-electron pathway

The oxygen is reduced to water without the formation of hydroperoxide as a reaction intermediate. This pathway is also known as “direct 4e<sup>-</sup> pathway”:

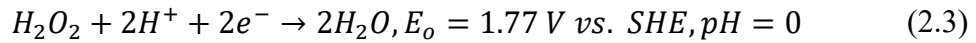


## 2) Peroxide-mediated pathway

The hydroperoxide is formed as a reaction intermediate. This pathway is also known as “series 2e<sup>-</sup> + 2e<sup>-</sup> pathway”:



Depending on the catalyst, the hydroperoxide can either diffuse to the electrolyte bulk from the catalyst surface, further be reduced to water:



or decomposed



### 2.1.2.1.1. Carbon materials

The undoped carbon materials have high overpotential for O<sub>2</sub> reduction to H<sub>2</sub>O<sub>2</sub> [19] and low activity for heterocatalytic H<sub>2</sub>O<sub>2</sub> decomposition in acidic media, being compared with Pt catalysts. Therefore, they are assumed not to participate in ORR catalysis in acidic media. However, doping by heteroatoms (e.g. N) and transition metals (e.g. Fe) makes them active for ORR in acidic media, which proceeds through the apparent direct 4e<sup>-</sup> pathway [20].

### 2.1.2.1.2. Platinum-based materials

In the early experimental works of Damjanovic et. al. [21], Sepa et. al. [22], [23], and Paucirova et. al. [24] the RRDE experimental setup was employed to elucidate the ORR mechanism in acidic media. It is argued that the ORR proceeds by the direct 4e<sup>-</sup> pathway on the pre-reduced oxide-free Pt without the organic contaminants in the electrolyte. The significant amount of H<sub>2</sub>O<sub>2</sub> is generated only in the region of H<sub>2</sub> UPD. The analyzed Tafel slopes at low overpotentials (-120 mV/dec) and high overpotentials (-60 mV/dec) together with current transients suggest the first step to be the rate-limiting. The slope change is attributed to the switch between the Temkin and Langmuir conditions of adsorption for the low and high overpotentials, respectively. The study of ORR mechanism at potentials

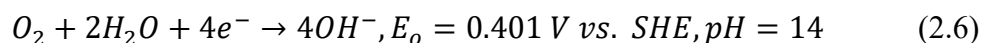
higher than 1.0 V vs RHE is complicated due to the side reactions of electrochemical Pt dissolution and surface phase oxides formation. Still, the oxygen evolution reaction (OER) can be studied on Pt electrodes, since the formation of the anodic surface oxide film reduces the rate of Pt dissolution by several orders of magnitude. The other suggestions on the rate-determining step (RDS) can also be used to explain the observed experimental results. For example, the rupture of the O-O bond via dual-site mechanisms [25], [26], O<sub>2</sub> adsorption step [27], O and OH desorption steps [28]. The more recent works show that the H<sub>2</sub>O<sub>2</sub> is produced on the single Pt particle/carbon filament ultramicroelectrodes [29] or the two-dimensional array of Pt nanoparticles on the glassy carbon (GC) electrode [30]–[32]. The combination of RRDE experimental data for Pt/VACNF in H<sub>2</sub>SO<sub>4</sub> and HClO<sub>4</sub>, elementary step models based on previous experimental findings [33]–[35], and microkinetic modeling has shown that the formation of the H<sub>2</sub>O<sub>2</sub> at low Pt site density is the intrinsic process for ORR on Pt. It leads to suggestions for the dual-path mechanism (i.e. with parallel direct 4e<sup>-</sup> and series 2e<sup>-</sup>+2e<sup>-</sup> pathways) on Pt [36], [37] in acidic media.

### 2.1.2.2. ORR pathways in alkaline media.

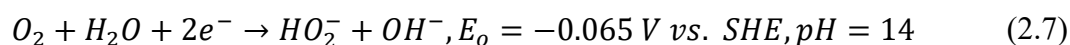
The ORR pathways in alkaline media are similar to the ones in acidic electrolytes. The main differences are the water is consumed during the ORR and H<sub>2</sub>O<sub>2</sub> is transformed to HO<sub>2</sub><sup>-</sup> by the following reaction:



1) Direct 4-electron pathway



2) Peroxide-mediated pathway



The HO<sub>2</sub><sup>-</sup> can either desorb from the catalyst surface, or further be reduced to water:



or decomposed

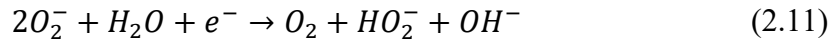


For the progress of development and comparison of most active ORR catalysts in alkaline media, one can refer to the comprehensive reviews of Ge et al. [7] and Cheng et

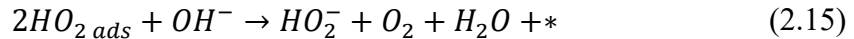
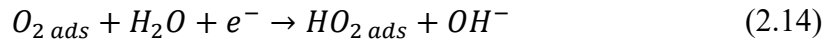
al. [38]. The studies of ORR materials classes described below are crucial for the elucidation of the ORR mechanism in alkaline media.

#### 2.1.2.2.1. Carbon materials

The undoped carbon materials are active for the ORR in alkaline media, thus contributing to the ORR electrocatalysis in the composite catalytic materials. The ORR principally proceeds through the first  $2e^-$  reduction in a series  $2e^-+2e^-$  pathway, with  $O_2$  being reduced only to  $HO_2^-$ . The superoxide  $O_2^-$  is considered as a reaction intermediate. For example, it was detected experimentally on basal planes of stress annealed pyrolytic graphite by Morcos and Yeager [39] using the flow-type thin layer electrochemical cell. The mechanism with outer-sphere electron transfer is suggested in this case [39], [40]:



The ORR currents on the basal planes are far lower than the ones on glassy carbons and ordinary pyrolytic graphites, thus suggesting that the ORR mainly proceeds with the strong interaction of  $O_2$  and surface functional groups with the mechanism provided in [39]:



Zhang et al. [41] showed experimental evidence for the quinone surface groups to be possible active sites for ORR. The mechanistic differences exist for the various carbon materials of different allotropic forms, supported by the difference in the corresponding ORR Tafel slopes and their variation with pH [42]. The pretreatment of carbon catalysts also has a significant influence on their activity for ORR [43], [44] and hence on the reaction mechanism. For example, the mechanisms with  $O_2^-$  surface migration to the active site [45] or two forms of adsorbed  $O_2^-$  [40] were suggested for ORR on GC electrodes. Various ORR mechanisms were suggested for different carbon materials [42], [44], [46]–[50]. It was shown that for the undoped carbon nanofiber and multiwalled carbon nanotubes ORR is likely proceeding through the following mechanism [51], [52]:



The doping of carbon materials by heteroatoms (e.g. N, B, S, P, F) significantly improves their performance for ORR. For example, the ORR on the N-doped carbon nanofibers and multiwalled nanotubes (CNTs) proceeds through the full  $4e^-$  reduction within the series  $2e^-+2e^-$  pathway [51], [53]. N-doping [54] is believed to introduce the electronic states near the Fermi level [55]. Additionally, it adds new active sites (likely the carbon atoms near the pyridinic nitrogen and graphitic nitrogen [55]), and produce edge plane defects [51]–[53], which can also participate in ORR, enhancing the catalytic activity for ORR. Additionally, the Fe oxide particles contained in CNTs due to the synthesis procedure are exposed on the surface after the N-doping [52], [53]. They are highly active for  $HO_2^-$  decomposition leading to the dual-site mechanism within the peroxide-mediated pathway [52].

#### 2.1.2.2.2. *Platinum-based materials*

Damjanovic et. al. [56] and Sepa et. al. [22], [23], [57] demonstrated that the ORR on polycrystalline Pt in alkaline media has the same Tafel slopes at low and high current densities as in acidic media. They are independent on electrode pretreatment, despite ORR has enhanced kinetics on pre-reduced Pt. The observed fractional order of 1/2 with respect to pH at low current densities, the first reaction order with respect to  $O_2$  on the whole potential range, and the linear increase of surface coverage with applied potential suggest that the first electron transfer step is RDS for ORR on Pt, with the Temkin condition of adsorption at low overpotentials and Langmuir condition of adsorption at high overpotentials. The difference in reaction orders with respect to pH in alkaline (1/2) and acidic (3/2) media is attributed to the participation of  $H^+$  in RDS for acidic media, which is opposite to alkaline media. The analysis of the ring/disc currents ratio suggested that ORR is likely to proceed through the series  $2e^-+2e^-$  or dual path (i.e. series  $2e^-+2e^-$  and direct  $4e^-$  pathways in parallel) mechanism. The decoupled currents for  $2e^-$  and  $4e^-$  reduction have the same Tafel slopes, which suggests that the ORR mechanism has the

same RDS and preceding steps for both pathways. The RRDE study of ORR and  $\text{HO}_2^-$  reduction on (100), (110), and (111) Pt single-crystal surfaces carried out by Markovic et al. [58] showed that Pt (111) surface is the most active one for ORR. Despite the negligible amount of  $\text{HO}_2^-$  being detected on the ring, its rapid reduction led to the suggestion of the peroxide-mediated pathway on low-index surfaces.

The general ORR mechanism inspired by the ORR study on PGM and carbons with the possible reaction intermediates in alkaline media is shown in Figure 2.2. The steps are not necessarily elementary.

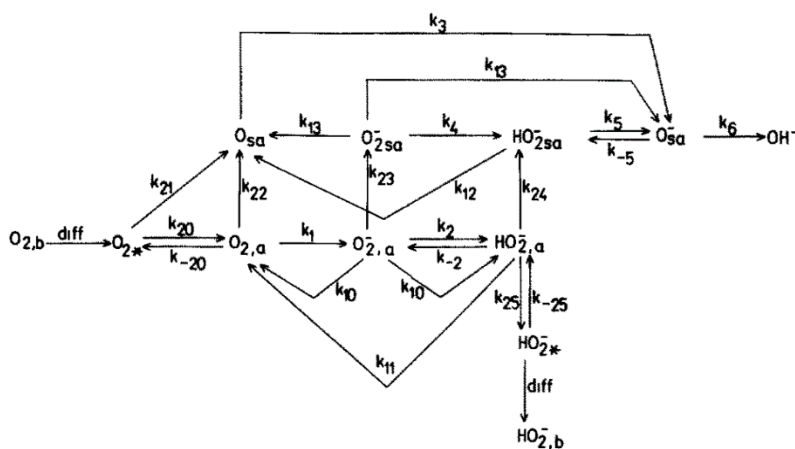


Figure 2.2 General ORR mechanism in alkaline media reproduced from Anastasijevic et al [59].

#### 2.1.2.2.3. Transition metal oxides

Opposite to acidic media, some of the non-noble transition metal oxides are stable in alkaline media at the potentials where ORR occurs. Many of them are highly active for ORR demonstrating the activity close to the one of Pt-based commercial catalysts. However, their relatively low electrical conductivities necessitate the use of conductive support, generally manifested through mixing with high-surface-area carbons. It significantly complicates the analysis and comparison of the intrinsic catalytic activities of different TMO catalysts, as the type and amount of the carbon support, catalyst synthesis and electrode preparation routines, and possible cathodic degradation significantly

influences the overall ORR activity [60], [61]. The most widely studied materials are based on spinels, perovskites, and other oxides (Mn-based).

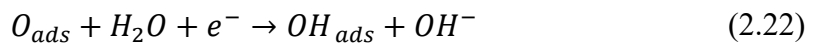
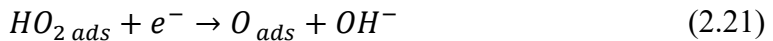
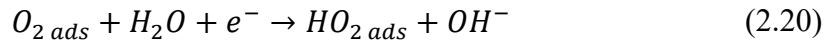
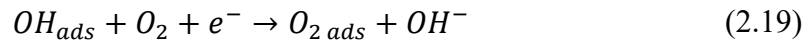
Pure spinels are relatively inert for ORR. However, they demonstrate an excellent catalytic activity for ORR within the spinel/carbon composite materials. It is further enhanced by the N-doping of carbon component and the presence of strong coupling between the spinel and carbon components (i.e. if the spinel nanoparticles are directly grown on carbon instead of physical mixing) [7], [62], [63]. The additional synergistic effects from strong coupling and ORR activity of carbon (or N-doped carbon) components further challenge the ORR mechanistic studies on these materials. Regarding the spinel component, the most active materials are based on  $\text{Co}_3\text{O}_4$  [64],  $\text{Mn}_3\text{O}_4$  [62], and  $\text{Fe}_3\text{O}_4$  [63]. They can be further optimized, e.g. Mn-substituted  $\text{MnCoO}_4$  spinel has higher catalytic activity than  $\text{Co}_3\text{O}_4$  on the same carbon component [65], while  $\text{Mn}_x\text{Cu}_{1-x}\text{Mn}_2\text{O}_4$  compounds with both Mn and Cu atoms demonstrate the highest catalytic activity [66]. These materials show  $\sim 4e^-$  reduction of oxygen with  $<10\%$   $\text{HO}_2^-$  yield and onset potential almost identical to the one for Pt/C, thereby being a promising alternative for ORR in alkaline media.

Perovskites, with the general formula  $\text{ABO}_{3\pm\delta}$ , where A is a large alkali-earth or rare-earth element and B is a transition metal, are an appealing model system because the physico-chemical and electronic properties of these materials can be easily tuned through substitution into the A and B sites, as well as through the formation of oxygen vacancies. For the initial optimization of site A, the La-based perovskites demonstrated the highest catalytic activity for ORR within the  $\text{LnMnO}_3$  series ( $\text{Ln} = \text{La, Pr, Nd, Sm, Gd, Y, Dy, Yb}$ ) [67]. As for the site B, Mn [68], [69], Co [70], [71], and Ni-based [53], [72] perovskites generally provide the highest catalytic activities for ORR. The reported results are highly dependent on the perovskite electrodes preparation method and the methodology of their studies, often being controversial. For example, within the  $\text{LaBO}_3$  ( $\text{B} = \text{Ni, Co, Mn, Ni, Fe, Cr}$ ) bulk perovskites without the conductive additives, the  $\text{LaCoO}_3$  exhibits the highest catalytic activity for ORR [71]. In contrast, the Co-based perovskites show the lower catalytic activity for ORR than the Mn-based ones [73]. Therefore, the mechanistic studies

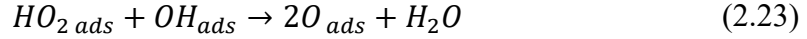
of ORR on perovskite materials require the self-consistent experimental dataset to evaluate and decouple the factors influencing the overall ORR activity.

Many other Mn oxides are active for ORR in alkaline media [74]. Their performance was shown to be connected with the experimentally observed [75] Mn(III)/Mn(IV) surface redox process, with the Mn(III) being the active site for ORR [76]. Mao et. al [77] demonstrated the Nafion-modified Mn /Au electrodes to follow the sequence  $Mn_5O_8 < Mn_3O_4 < Mn_2O_3 < MnOOH$  for ORR activity. Cheng et. al [78] reported catalytic performance of  $MnO_2$  polymorphs to follow the sequence  $\alpha\text{-}MnO_2 > \beta\text{-}MnO_2 > \gamma\text{-}MnO_2$ . Ryabova et. al [79] showed an excellent activity of  $\alpha\text{-}Mn_2O_3$ (byxbyite) for ORR, being the highest within the series of studied Mn oxides:  $\alpha\text{-}Mn_2O_3$ (byxbyite)  $>$   $\beta\text{-}MnO_2$ (pyrolusite)  $>$   $Mn_3O_4$ (spinel)  $>$   $\gamma\text{-}MnOOH$ (manganite). The opposite trend was observed for  $HO_2^-$  yields and the limiting currents for the  $2e^-$  reduction of  $HO_2^-$  on these materials. The amount and consistency of these experimental findings make them a good model system to obtain further insights on the ORR mechanism with respect to the TMO component.

The ORR mechanism on transition metal oxides is different from the one on noble metals. The surface cations tend to fulfill their oxygen coordination by the  $H_2O$  so that the hydrogen atoms are distributed across the surface. The protonation of the surface ligand is coupled with the reduction of the metal cation. The hydroxylated cation further interacts with  $O_2$ , thus catalyzing the ORR. Different reaction mechanisms with one-electron steps that account for the different adsorption geometries of reaction intermediates were considered for ORR on metal oxides in alkaline media. The question about the presence of the direct or peroxide-mediated pathway is still open for TMOs. The most widely adopted mechanism with the formation of  $HO_2^-$  as a surface intermediate was suggested by Cushing and Goodenough [80]:



The reaction mechanism with  $\text{HO}_2^-$  disproportionation on the catalyst surface was also shown to be in good agreement with the experimental observations for perovskite oxides [68] and simple Mn oxides [79].



Additionally, the TMOs typically have low electronic conductivity and are mixed with carbon materials to provide good electric contact. The carbon materials are active for  $\text{O}_2$  reduction to  $\text{HO}_2^-$ . The  $\text{HO}_2^-$  can be produced on carbon component and then readsorbed on TMO to undergo further reduction:



It can be one of the many possible explanations for complex synergistic effects observed in TMO/C composite materials [60], [61], [68], [73], [79].

Therefore, further insights for the ORR mechanism and the catalytic activity trends for the TMO/C components require the self-consistent dataset (i.e. the same electrode composition, mass loadings, methodology of experimental measurements, etc.). The  $\alpha\text{-Mn}_2\text{O}_3$  -...-  $\gamma\text{-MnOOH}$  series [79] can be used to study the ORR mechanism with respect to the TMO component due to the pronounced difference in ORR and  $\text{HO}_2^-$  reduction and availability of high-quality experimental data. The influence of the carbon type (including the N-doping effects) can be probed on  $\text{LaCoO}_3/\text{C}$  materials, which are stable above 0.4 V vs. RHE [81], provide flexibility in further modification of their properties, and exhibit the synergy for ORR within the composite.

### 2.1.3. Summary

ORR is a complex surface-sensitive reaction. Its mechanism strongly depends on the catalyst. The ORR elementary-step mechanism is ambiguous and cannot be completely determined based on the electrochemical characterization even on the excessively studied Pt catalysts. Its complexity requires precise experimental data combined with the insights from numerical macroscale and/or *ab initio* techniques in order to be elucidated on TMO/C composite materials, which are the matter of active research for AEMFC, metal-air batteries, and regenerative fuel cells. The  $\alpha\text{-Mn}_2\text{O}_3$  -...-  $\gamma\text{-MnOOH}$  and  $\text{LaCoO}_3/\text{C(N-}$

doped C) can be used as good model systems for the further elucidation of the ORR mechanism with respect to TMO and carbon components, respectively. The uncertainty in the ORR mechanism calls for the uncertainty quantification on each level of description to understand whether the elementary step (or at least one-electron step) mechanism can be determined based on the available experimental data and accuracy of approximations together with employed numerical methods.

## 2.2. Multiscale modeling approach

The process of reaction mechanism study can be started either in the top-down or bottom-up design. The top-down design starts from the generalization of experimental observations, such as Tafel slopes, redox potentials, the effective number of transferred electrons at mass-transfer limiting regime, etc. together with the insights from the materials characterization techniques [53], [82]–[84]. Then the initial hypothesis about the reaction mechanism is made based on the interplay of theory, prior chemical knowledge, and modeling/simulation of experiments. The latter is performed using the macroscale phenomenological or elementary step models by extracting the model parameters to precisely fit the experiments (the so-called inverse problem) [20], [79], [85], [86]. Finally, the reaction mechanism is verified by *ab initio* molecular level simulations [87]–[91]. The bottom-up design follows the opposite route starting from molecular level insights, e.g. relevant surface structures, active sites, and free energy diagrams for the reaction under study. These insights are further validated by experimental results through the mean-field models or kinetic Monte Carlo simulations (KMC) [92]. However, the experiments for the complex heterogeneous reactions cannot be directly fitted by molecular-level models in their current stage of development [91], [93]–[96]. The mean-field models play an integral role in connecting molecular level insights and observable experimental findings by linking the macroscale model parameters (rate constants, etc.) with the other parameters estimated on the molecular level (such as activation energies, etc.). Nowadays, the most valuable insights are obtained from the interplay of top-down and bottom-up designs within the multiscale modeling approach [97], [98].

### 2.2.1. Mean-field microkinetic modeling approach

Mean-field microkinetic models are deduced from the formal reaction rate equations (kinetic level of description) via the incorporation of the basic surface chemistry. It enables their application for the elucidation of the heterogeneous catalytic reactions. The surface processes are reflected through the addition of the average surface coverages for adsorbed reaction intermediates and the corresponding active sites surface densities for the reaction under study. This is done under the assumption that all surface active sites are equal and local coverage effects are negligible. The adsorbate-adsorbate interactions are either neglected (Langmuir adsorption isotherm) or accounted on average (e.g. Frumkin, Temkin adsorption isotherms), influencing the surface coverages.

#### 2.2.1.1. Mathematical description

The general mathematical formulation of MF-MKM can be expressed as follows. Consider the arbitrary net heterocatalytic reaction with  $N$  reactants and  $M$  products:



Where  $X_j, \nu_j |_{j=1,N} / X_j, \nu_j |_{j=N+1,N+M}$  are reactant/product species and the corresponding stoichiometric numbers. Assuming that

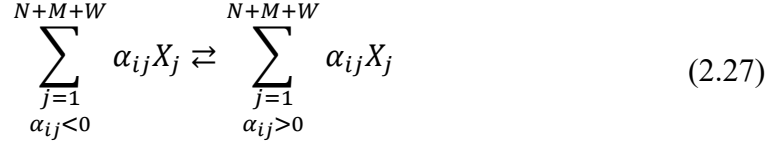
- The reaction proceeds through  $L$  elementary steps including the surface adsorption and reactions via the Langmuir-Hinshelwood or Eley-Rideal mechanisms [99]. The elementary step may be repeated several times giving the same amount of identical rows in  $\alpha$ .
- There are  $W$  reaction intermediates, including the adsorbed reactants/products and free active sites available for the adsorption.

One can define the stoichiometric matrix (all values are integers):

$$\alpha = \begin{pmatrix} \alpha_{11} & \dots & \alpha_{1N} & \dots & \alpha_{1(N+M)} & \dots & \alpha_{1(N+M+W)} \\ \dots & \dots & \dots & \dots & \dots & \dots & \dots \\ \alpha_{L1} & \dots & \alpha_{LN} & \dots & \alpha_{L(N+M)} & \dots & \alpha_{L(N+M+W)} \end{pmatrix} \quad (2.26)$$

Each  $i^{\text{th}}$  row of the matrix represents the stoichiometric coefficients in the corresponding elementary step. In most cases, only a few species participate in each elementary step

giving  $\alpha_{ij} = 0$  for others.  $\alpha_{ij} < 0$  if  $X_j$  is a reactant for step  $i$ ,  $\alpha_{ij} > 0$  if  $X_j$  is a product for the  $i^{\text{th}}$  step. For the elementary step attributed to the  $i^{\text{th}}$  row of the matrix:



The reaction rate can be expressed as follows:

$$r_i = r_{+i} - r_{-i} = k_i \prod_{\substack{j=1 \\ \alpha_{ij}<0}}^{N+M+W} \hat{X}_j^{|\alpha_{ij}|} - k_{-i} \prod_{\substack{j=1 \\ \alpha_{ij}>0}}^{N+M+W} \hat{X}_j^{|\alpha_{ij}|} \quad (2.28)$$

Here  $\hat{X}_j$  is either surface or bulk activity  $a_j$ /molar concentration  $c_j$  {mol cm<sup>-3</sup>} in solution, partial pressure  $\frac{p_j}{p_0}$  {1} in a gas phase, or coverage on the surface  $\theta_j$  {1},  $\theta_j \in [0, 1]$ . It depends on the experimental conditions and the suggested reaction mechanism.  $r_{+i} / r_{-i}$  {mol s<sup>-1</sup> per active site} are forward/backward reaction rates.  $k_i / k_{-i}$  are forward/backward rate constants. Their units are specified by  $\alpha_{ij}$  and  $\hat{X}_j$  to give correct units of  $r_{+i} / r_{-i}$ .

For the elementary step,  $k_i$  and  $k_{-i}$  have Arrhenius form and are connected through the equilibrium constant  $K_i$ :

$$k_{-i} = \frac{k_i}{K_i} \quad (2.29)$$

Defining the  $\widehat{X}^0$  as the equilibrium surface activities/bulk activities/partial pressures/surface coverages:

$$r_i(\widehat{X}^0) = 0, i \in [1, L] \quad (2.30)$$

One can express  $K_i$  as follows:

$$K_i = \prod_{\substack{j=1 \\ \alpha_{ij}<0}}^{N+M+W} \widehat{X}_j^{-|\alpha_{ij}|} \prod_{\substack{j=1 \\ \alpha_{ij}>0}}^{N+M+W} \widehat{X}_j^{|\alpha_{ij}|} \quad (2.31)$$

The thermodynamic consistency implies that the unique non-trivial  $\widehat{X}^0$  should exist to simultaneously provide the equilibrium for all elementary steps within the proposed reaction mechanism.

The stoichiometric matrix has the following properties:

- In the absence of surface poisoning effects, the number of surface active sites is conserved, all reaction intermediates form products to satisfy the net reaction (stoichiometric consistency):

$$\sum_{\substack{i=1 \\ j \in [N+M+1, N+M+W]}}^L \alpha_{ij} = 0 \quad (2.32)$$

- For the inert species, irreversibly adsorbed on the active sites under the experimental conditions, that do not participate in the reaction but reduce the number of active sites available for adsorption:

$$\alpha_{ij} = 0, i \in [1, L], X_j - \text{inert} \quad (2.33)$$

- The proposed reaction elementary steps should be consistent with the net reaction in terms of products and reactants:

$$\sum_{\substack{i=1 \\ j \in [1, N+M]}}^L \alpha_{ij} = \nu_j \quad (2.34)$$

The system of mass-balance equations to be solved to calculate the transients  $\hat{X}_j(t)$  can be formulated as follows:

$$\frac{d\hat{X}_j}{dt} = A_{\hat{X}_j} \sum_{i=1}^L \alpha_{ij} r_i + B_{\hat{X}_j} (F_j^{in} - F_j^{out}) \quad (2.35)$$

Here,  $A_{\hat{X}_j}$ ,  $B_{\hat{X}_j}$  are coefficients whose dimensionality depends on the  $\hat{X}_j$  and experimental design.  $F_j^{in}$ ,  $F_j^{out}$  {mol s<sup>-1</sup>} are respectively input and output flows of the j<sup>th</sup> species, reflecting the transport effects. Generally, the  $\hat{X}_j$ ,  $F_j^{in}$ ,  $F_j^{out}$  also depend on the space coordinates and corresponding partial derivatives (e.g. diffusion due to concentration gradients). The corresponding system of partial differential equations, which is to be added to the (2.35) (e.g. based on Navier-Stokes and Nernst-Planck equations), does not have an analytical solution in the general form [83], [100]. It brings the necessity either to use the

advanced methods from computational fluid dynamics (CMD) [101] or to employ the special experimental setup, which enables simpler mathematical treatment.

The numerical/analytical solution for the system of ordinary differential equations (ODE) or partial differential equations (PDE) (2.35) provides the  $\widehat{X}_j(t)$ , which is fitted to the available experimental data by the independent model parameters. One should select the model parameter as the independent one if it cannot be estimated based on the theory and available experimental data. Typically, some of  $k_i$  and  $k_{-i}$  are selected as the independent model parameters, while the active sites surface densities, kinematic viscosities, and diffusion coefficients in the solution are estimated.

As the simplest case, if  $\widehat{X}_j$  is a molar concentration in the ideal batch reactor, then

$$A_{\widehat{X}_j} = \frac{S_R}{V_R}, B_{\widehat{X}_j} = \frac{1}{V_R}, F_j^{out} = F_j^{in} = 0 \quad (2.36)$$

Where  $V_R$  {cm<sup>3</sup>} is the volume of an ideal batch reactor,  $S_R$  {mol} – the number of active sites in the reactor. The detailed mathematical description of easier to implement but more complex to describe adiabatic and isothermal plug-flow reactors (PFR) and continuous-flow stirred tank reactor (CSTR) can be found in the excellent review by P. Stoltze [102].

The solution of (2.35) is a complicated procedure that should be simplified by the introduction of physically meaningful constraints to reduce the number of mass-balance equations for reaction species and independent model parameters. These may include the conservation of active sites, thermodynamic consistency through the known equilibrium constants, additional restrictions provided by the experimental design (e.g. energy balance in adiabatic PFR [102]), the combination of transition state theory (TST) with *ab initio* simulations, and appropriate approximations for the reaction mechanism.

#### 2.2.1.2. Approximations

- Steady-state approximation

If the experimental setup operates in a steady-state regime, where the net rate of formation of all reaction intermediates is zero, then their transient behavior can be

eliminated. It simplifies the further simulations as the corresponding ODEs are reduced to the system of algebraic equations (the situation is more complicated for PDEs).

$$\frac{d\hat{X}_j}{dt} = A_{\hat{X}_j} \sum_{i=1}^L \alpha_{ij} r_i + B_{\hat{X}_j} (F_j^{in} - F_j^{out}) = 0, \quad j \in [N + M + 1, N + M + W] \quad (2.37)$$

This approximation does not imply that  $\hat{X}_j$  is small.

- Quasi-equilibrium approximation

If the reaction step is fast comparing to the ones which determine the net reaction rate, then it is assumed to be in equilibrium. Therefore, the corresponding equilibrium equation can be used (2.31) to eliminate either forward or backward rate constant as a model parameter. Quasi-equilibrium approximation is often applied to all but one step, assuming that the latter one is governing the net reaction rate. This approximation is known as the RDS approximation. It provides great simplification and enables the analytical treatment of a model under study. However, the information on the change in RDS and transient behavior is lost.

- Irreversible step approximation

If the reaction step is far from equilibrium, then the forward or backward rate is negligible and can be approximated to be zero. This is a rather rough approximation, that cannot be used to describe the reaction near the equilibrium.

$$\begin{aligned} r_{+i} &\ll r_{-i} \rightarrow r_{+i} \approx 0 \\ r_{+i} &\gg r_{-i} \rightarrow r_{-i} \approx 0 \end{aligned} \quad (2.38)$$

- MARI

The most-abundant reaction intermediate (MARI) approximation implies that the most stable reaction intermediate  $A^*$  is dominating in the active site's balance, and the contributions of less-abundant reaction intermediates can be neglected:

$$\theta_* + \theta_{A^*} \approx 1 \quad (2.39)$$

- Almost-empty surface approximation

This further approximation implies that surface coverage by all reaction intermediates is negligible compared to the free active sites. Hence,

$$\theta_* \approx 1 \quad (2.40)$$

This approximation cannot be used to provide insights about the effects of surface coverage on the reaction kinetics.

### 2.2.1.3. Charge-transfer step description

Consider the elementary step that involves the electron transfer (ET) on the electrode-electrolyte interface



The simultaneous transfer of multiple electrons in one elementary step is a statistically unlikely event, so it is usually assumed that  $n = 1$  for the elementary ET step. The kinetics of the ET step can be also described by the rate equation considering the dependence of the activation energies in the Arrhenius-like formula for forward/backward rate constants on the potential difference across the interface. Assuming that the electric potential is constant in the solution bulk and changes only in the vicinity of an electrode, the Butler-Volmer formalism can be used to incorporate the dependence of activation energy on the applied potential:

$$r_{CT} = k_{CT} \widehat{X}_O \exp \frac{-\alpha n F (E - E_{eq})}{RT} - k_{-CT} \widehat{X}_R \exp \frac{(1 - \alpha) n F (E - E_{eq})}{RT} \quad (2.42)$$

Here  $k_{CT}/k_{-CT}$  are forward/backward rate constants at standard conditions,  $\alpha \in [0,1]$ ,  $\alpha \approx 0.5$  – cathodic transfer coefficient,  $F$  – Faraday constants,  $T$  – temperature,  $R$  – universal gas constant,  $E$  - applied potential vs. reference electrode,  $E_{eq}$ - equilibrium potential.  $E_{eq}$  can be calculated for the reaction conditions from the Nernst equation for the (2.42) in equilibrium:

$$E_{eq} = E^{0'} + \frac{RT}{nF} \ln \frac{\widehat{X}_O}{\widehat{X}_R} \quad (2.43)$$

$E^{0'}$  – is equilibrium potential at standard conditions. The same approximations described above can be applied for the chemical-electrochemical reaction mechanism. The key difference is that for the effective steps which include several elementary ET steps the dependence of the activation energy on the applied potential is determined by the position of RDS within the quasi-equilibrium approximation. Accurate derivation can be found

elsewhere [103]. Briefly, if n-electron RDS repeated  $\nu$  times with  $\vec{\gamma}/\tilde{\gamma}$  electrons transferred before/after the RDS within the reaction steps in quasi-equilibrium, then the cathodic  $\vec{\alpha}$  and anodic  $\tilde{\alpha}$  transfer coefficients will be different and equal to:

$$\vec{\alpha} = \begin{cases} \frac{1}{n} \left( \frac{\vec{\gamma}}{\nu} + n \alpha \right), n > 0 \\ \frac{\vec{\gamma}}{\nu}, n = 0 \end{cases} \quad (2.44)$$

$$\tilde{\alpha} = \begin{cases} \frac{1}{n} \left( -\frac{\tilde{\gamma}}{\nu} + n \alpha \right), n > 0 \\ 1 - \frac{\tilde{\gamma}}{\nu}, n = 0 \end{cases} \quad (2.45)$$

#### 2.2.1.4. Simulation of a rotating ring-disk electrode

The rotating ring-disk electrode experiment provides known reproducible mass-transfer conditions. The corresponding solution of Navier-Stokes and convective-diffusion equations with the appropriate boundary conditions were derived by Levich [100] and provided the concentration gradients for the reacting species in the vicinity of the electrode surface.

$$\left( \frac{\partial c_j}{\partial x} \right)_{x=0} = \frac{c_j - c_j^*}{\delta_j} \quad (2.46)$$

Here,  $c_j$  and  $c_j^*$  are molar concentrations of the  $j^{\text{th}}$  species on the vicinity of electrode and in the solution bulk, respectively;  $\delta_j$  is the diffusion layer thickness. The latter is estimated as follows:

$$\delta_j = 1.61 D_i^{1/3} \omega^{1/2} \nu^{1/6} \quad (2.47)$$

$D_j$  {cm<sup>2</sup> s<sup>-1</sup>} – diffusion coefficient of the  $j^{\text{th}}$  species in the solution,  $\omega$  {rad s<sup>-1</sup>} – electrode rotation rate, and  $\nu$  {cm<sup>2</sup> s<sup>-1</sup>} – kinematic viscosity.

So the great simplification of the mass balance equations (2.35) is provided. For the reaction species adsorbed on the surface  $F_j^{\text{in}} = F_j^{\text{out}} = 0$ . Hence, the corresponding mass-balance equation can be depicted as follows:

$$\frac{d\hat{\theta}_j}{dt} = \sum_{i=1}^L \alpha_{ij} r_i \quad (2.48)$$

For the surface concentrations, the mass-balance equation can be derived under the assumption of a linear concentration profile in the diffusion layer:

$$\frac{dc_j}{dt} = \frac{2}{\delta_j} \sum_{i=1}^L \Gamma_i \alpha_{ij} r_i + \frac{2D_j}{\delta_j^2} (c_j^* - c_j) \quad (2.49)$$

Here,  $\Gamma_i$  {mol cm<sup>-2</sup>} is an active site surface density for the  $i^{\text{th}}$  reaction step which occurs on the electrode surface. One can find the detailed derivation of (2.49) in the paper of M.T.M. Koper and J. H. Sluyters [104].

The charge transfer steps make the right part of the ODEs system (2.48), (2.49) non-autonomous since the applied potential on the electrode is typically dependent on time in RDE experimental design. For the linear sweep, the applied potential should be substituted by  $E_{start} + vt/E_{start} - vt$  for anodic/cathodic scan. Here,  $v$  {V/s} is the scan rate and  $E_{start}$  {V} is starting potential. One can exclude the time dependence of the right part of the ODEs system by an addition of the following ODE:

$$\begin{cases} \frac{dE}{dt} = v, \text{ anodic scan} \\ \frac{dE}{dt} = -v, \text{ cathodic scan} \end{cases} \quad (2.50)$$

The current, which is recorded vs. applied potential in the RDE experiment, can be calculated from the solution  $\widehat{X}^{sol}(t)$ ,  $E^{sol}(t)$  of ODEs (2.48), (2.49), (2.50):

$$j_{disk}(E^{sol}(t)) = A_{disk} \sum_{i=1}^L N_i^e F \Gamma_i \alpha_{ij} r_i(\widehat{X}^{sol}(t), E^{sol}(t)) \quad (2.51)$$

Here,  $A_{disk}$  {cm<sup>2</sup>} – area of the disk electrode,  $N_i^e$  {1} – number of transferred electrons in charge-transfer steps on the vicinity of the electrode (zero for the chemical steps).

The ring currents can be easily computed from the known mass-transfer of the reaction intermediates from the disk electrode and analytically or experimentally determined collection efficiency.

#### *2.2.1.5. History and applications*

MF-MKM was extensively used as a part of the microkinetic analysis. The term “microkinetic analysis” is equivalent to the multiscale modeling approach. It was evolved in the pioneering works of P. Stoltze and K. Norskov on high-pressure ammonia synthesis reaction [105]–[108], followed by the water-gas shift reaction study [109], and other applications [110], [111]. The steady-state transients of partial pressures and surface coverages along the PFR were simulated numerically using the MF-MKM. The studied reaction mechanisms have numerous reaction steps, corresponding model parameters, and variables (Table 2.2). The main point of these works is that all model parameters were estimated from the experiments on single-crystals in UHV, underlying theory, and TST. These estimates were then extrapolated to the working conditions of commercial PFRs by the adjustment of temperature and pressures. It was done within the assumption that in the gas phase the change in the latter does not significantly change the reaction mechanism and rate constants on the single active site. Since the sufficient experimental dataset is generally unavailable for accurate determination of surface kinetic and thermodynamic parameters, the rough estimations of model parameters are typically made. In most cases, the obtained set of model parameters should be further adjusted to reproduce available experimental data. For example, in the works of J. Dumesic group on reactions of n-Hexane on Pt and methanol on H-ZSM-5 zeolite [112] and ethane hydrogenolysis [113], the unknown model parameters were roughly estimated through TST, heats of formation of reaction intermediates in a gas phase, experiment fitting, and known surface bonding strengths. In the more recent works [114]–[117], additional experimental insights and/or DFT calculations for model parameters provided better agreement of the microkinetic model with experimental data.

Table 2.2 Details of MF-MKM simulations

Reaction under study	Experimental setup	Catalyst	$N_{\text{reaction steps}} /$ $N_{\text{variables}} /$ $N_{\text{model parameters}} /$ $N_{\text{estimated model parameters}}$	Approximations	Ref.
Ammonia synthesis	PFR, gas phase	Topsoe KMIR (K-doped Fe)	7/3/9/9 8/4/10/10 for O-poisoning study	Steady-state, 1 RDS, no adsorbate-adsorbate interactions, $\Theta_{N_2} \approx 0$	[105]– [108]
Water gas shift reaction	PFR, gas phase	Cu	8/8/12/12	Steady-state, 3 RDS, no adsorbate-adsorbate interactions,	[109]
Ethylene oxidation	PFR, gas phase	Ag	17/20/35/35	Steady-state, no adsorbate-adsorbate interactions	[111]
Reactions of n-Hexane	PFR, gas phase	Pt	17/19/35/32	Steady-state, no adsorbate-adsorbate interactions, CSTR approximation	[112]
Reactions of Methanol	PFR, gas phase	H-ZSM-5 Zeolite	27/22/55/52	Steady-state, no adsorbate-adsorbate interactions, CSTR approximation	[112]
Ethane Hydrogenolysis	PFR, gas phase	Pt, Pd, Ir, Co	8/10/12/7	Steady-state, no adsorbate-adsorbate interactions, CSTR approximation	[113]
Methane Partial Oxidation	PFR, gas phase	Si-supported MoO <sub>3</sub> and V <sub>2</sub> O <sub>5</sub>	12/15/24/24	Steady-state, no adsorbate-adsorbate interactions, CSTR approximation, steps 1-4 in quasi-equilibrium	[114]
Water gas shift reaction	Fixed bed reactor, gas phase	Cu	8/10/17/17	Steady-state, no adsorbate-adsorbate interactions, CSTR, PFR approximations	[115], [117]
ORR/OER	RRDE	Pt/VACNF acidic media, LCO/C alkaline media, Mn-oxides/C, Fe/N/C acidic media	6/7/21/10 – 10/8/30/10, 8/8/26/10, 3/3/13/9	Steady-state approximation, no adsorbate-adsorbate interactions, linear concentration profile in diffusion layer, equally accessible active sites Almost empty surface approximation in the work [20]	[20], [36], [73], [79], [118]
ORR/OER	— RRDE	IrO <sub>2</sub> , RuO <sub>2</sub> , RhO <sub>2</sub> , PtO <sub>2</sub> acidic media, Pt(111) acidic media,	6/0/7/7 12/10/37/37.	Steady-state approximation, no adsorbate-adsorbate interactions, linear concentration profile in diffusion layer, equally accessible active sites, RDS in [119]	[119], [120]

The MF-MKM models are also used to elucidate the reaction mechanism of heterogeneous electrochemical reactions. One can subdivide the common frameworks with MF-MKM into the three types considering the ORR/OER as the example.

1. The analysis of Tafel slopes within the suggested reaction mechanism (Shinagawa et al., Mefford et al.). [121], [122] The corresponding microkinetic model is solved analytically using the RDS approximation for each reaction step. The values of rate constants are not important but should be consistent with the RDS approximations. Mass-transfer effects are neglected. A comparison of calculated and experimental Tafel slopes provides insights on the nature of the RDS. The ambiguous match of the Tafel slope and RDS introduces the uncertainty in this qualitative approach.

2. Fitting of the experimental data (Bonnefont et al., Jaouen et al., Mefford et al.) [20], [37], [68], [79], [118], [122], [123]. RRDE experiment is typically used as a common setup to extract the reaction kinetics on the solid-liquid interface. The parameters, which describe mass-transport on the vicinity of the electrode (diffusion coefficients, kinematic viscosity, bulk concentrations, electrode rotation rate) are estimated from the experiments. Active sites surface densities are usually estimated from BET/BJH, SEM, TEM, XPS. The fitted model parameters (rate constants and transfer coefficients) should semi-quantitatively reproduce all experimental data under varying experimental conditions and have physically-reasonable values. The set of optimized model parameters is used to gain insights into the reaction mechanism. The influence of their variation near the optimal values on the reaction kinetics is used as a guide for the further catalyst search. The uncertainty of the optimal model parameters should be estimated because this is the inverse problem.

3. The experiment is simulated with the microkinetic model parameters, which are calculated on the molecular level (Norskov et. al) [119], [120]. The complex nature of the effects on the solid-liquid interface and insufficient experimental data requires advanced simulation techniques. Typically, the DFT (periodic and local basis) with MD is used to compute the free energy diagrams (including the transition states) for the reaction. The rate constants are further calculated using the TST. The significant solvent, electrostatic-field,

and surface coverage effects should be directly treated by such calculations in order to accurately estimate the rate constants under the working conditions. Because of the methodological and technical complications (especially for ET steps), the rough approximations are typically used (BEP, linear scaling relations) to estimate the activation energies bringing the errors to the computed model parameters.

### 2.2.2. Density functional theory

The study of the reaction mechanism on the molecular level requires the solution of the Schrodinger equation. The wavefunctions for the N-electron system are 3N dimensional. The electrode surface reactions require big molecular ensembles to correctly describe the catalyst surface, solvent effects, and reaction under study. Therefore, the dimensionality of the problem should be reduced in order to study the ORR on the molecular level. The *ab initio* methods are preferred as they do not depend on the experimental data comparing with semiempirical methods. Therefore, they can be applied to the study of unknown reaction mechanisms avoiding the errors from the inadequate parametrization from available experimental data [124].

The state of the art *ab initio* method, extensively used in electrocatalysis is the density DFT. It provides highly reduced computational efforts, which enables the simulation of the surface reactions. DFT is the method of electronic structure calculations within the Born-Oppenheimer approximation [125]. It numerically evaluates the electronic ground state for the chosen molecular system. DFT is based on the first principle of quantum mechanics, thereby called an *ab initio* technique in case of employed non-empirical functional. The computational cost is significantly decreased due to the use of 3-dimensional electronic density instead of 3N-dimensional wave functions. This transition is possible due to the Hohenberg and Kohn theorem [126], which shows that the ground state energy is the unique functional of the electronic density. The exact form of functional is unknown, so many approximate expressions are provided. They usually give an accuracy of 5-10% for the computed ground state energy, which is sufficient for the surface reaction simulations.

In practice, electronic density is calculated from one-electron wave functions using the Kohn-Sham equations [127] (2.52):

$$\left[ \frac{\hbar^2}{2m} \nabla^2 + V(\vec{r}) + V_H(\vec{r}) + V_{XC}(\vec{r}) \right] \psi_i(\vec{r}) = \varepsilon_i \psi_i(\vec{r}) \quad (2.52)$$

The terms in brackets define, in order, kinetic energy, interaction energy between each electron and the collection of the atomic nuclei, Hartree potential (Coulomb repulsion between the electron and the total electron density), and the exchange and correlation contributions to the one-electron equation. Usually, the core electrons are implicitly treated via the pseudopotentials [128]–[130], as their explicit simulation will not considerably affect the computed physical/chemical quantities. The DFT-based approximate solution of the time-dependent Schrodinger equation can be also obtained using the *ab initio* molecular dynamics [131].

Various functionals were developed for  $V_{XC}(\vec{r})$ . The simplest ones are based on the local density approximation (LDA). The exchange-correlation potential is treated as the exchange-correlation potential of the spatially uniform electron gas. The latter has the same density as the local electron density. The next level of the  $V_{XC}$  treatment is the generalized gradient approximation (GGA). It approximates nonuniformity of the electron density by including the dependence of the  $V_{XC}$  on the electron density gradient. The two most popular nonempirical GGA functionals are Perdew-Wang 91 (PW91) [132] and Perdew-Burke-Ernzerhof (PBE) [133]. The latter showed good accuracy for the estimation of the binding energies. Its improved version is called Revised Perdew-Burke-Ernzerhof (RPBE). It provides even better accuracy for the computed binding energies [134], thus being preferable for the surface reaction studies.

The surfaces and even nanoparticles are very large from the atomistic point of view. There are two general approaches to their simulation. The first approach is to model the surface by the small cluster of atoms, using the localized basis set. However, affordable for calculations size of these clusters are much smaller than the size of the actual nanoparticles. The second one is based on surface modeling as a slab, using a supercell, periodic in three

dimensions with applied periodic boundary conditions. These systems are typically simulated using the plane wave (PW) basis sets.

### 2.2.2.1. The aspects of DFT study of ORR mechanism

The periodic supercell approach is preferred to study the ORR as it gives better quantitative results in binding energies and can be used to simulate the reaction on the realistic liquid-solid interfaces. The ORR electron transfer steps require the direct simulation of the charged surfaces, which is hampered by the periodic charge imaging effects. Additionally, the applied potential (U) on the liquid-solid interface should be accounted for. In the first approximation, these problems were addressed by the computational hydrogen electrode model (CHE) [9]. CHE provides pH and U corrections from the equilibrium of half-reaction (2.53), which by definition has the potential of 0 V at 1atm H<sub>2</sub> and 1M H<sup>+</sup> solution.



The free energy diagram for the ORR mechanism is calculated from the DFT binding energies of reaction intermediates (with zero-point energy and entropic corrections) and a sequence of chemical and electrochemical steps (H<sup>+</sup>+e<sup>-</sup>, OH<sup>-</sup>-e<sup>-</sup>)[135], which conserves the neutral charge of the periodic slab. The relevant surface coverage is estimated from the computed surface Pourbaix diagram [136] (see Figure 2.3).

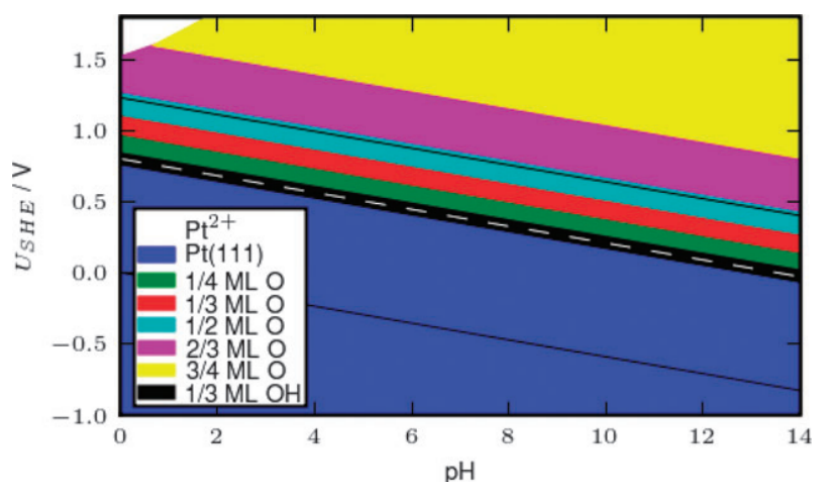


Figure 2.3 Computed surface Pourbaix diagram for Pt (111) [136].

The solvent layers can be explicitly added [137], [138] to study its effect on the ORR free energy diagram. It was shown to be significant. For example, the ORR reaction intermediates on Pt (111) namely the  $\text{OH}_{\text{ads}}$ ,  $\text{OOH}_{\text{ads}}$ ,  $\text{O}_{\text{ads}}$ ,  $\text{H}_{\text{ads}}$  are stabilized ca.  $\sim 0.6$ ,  $\sim 0.6$ ,  $\sim 0.1$ ,  $\sim 0.1$  eV respectively [139], [140]. The CHE cannot be used to compute the activation barriers for electrochemical steps. The empirically observed Brønsted–Evans–Polanyi (BEP) principle [141] is used instead. It suggests the linear correlation between the Gibbs free energy change and the activation barrier of the reaction step. This assumption also introduces the additional degree of uncertainty in the estimated activation energies. The RDS definition is then replaced by potential determining step (PDS) for the electron transfer step with the highest Gibbs free energy change.

Despite the various limitations incorporated into the thermodynamic DFT approach, it was successfully applied for the ORR study. The observed linear scaling relations between the free energies of adsorption of ORR intermediates [87], [142], together with electronic structure descriptors/free energy of adsorption correlations [72], [143], led to the development of the volcano plot [9], [72] (See Figure 2.4), which was used for the catalyst optimization.

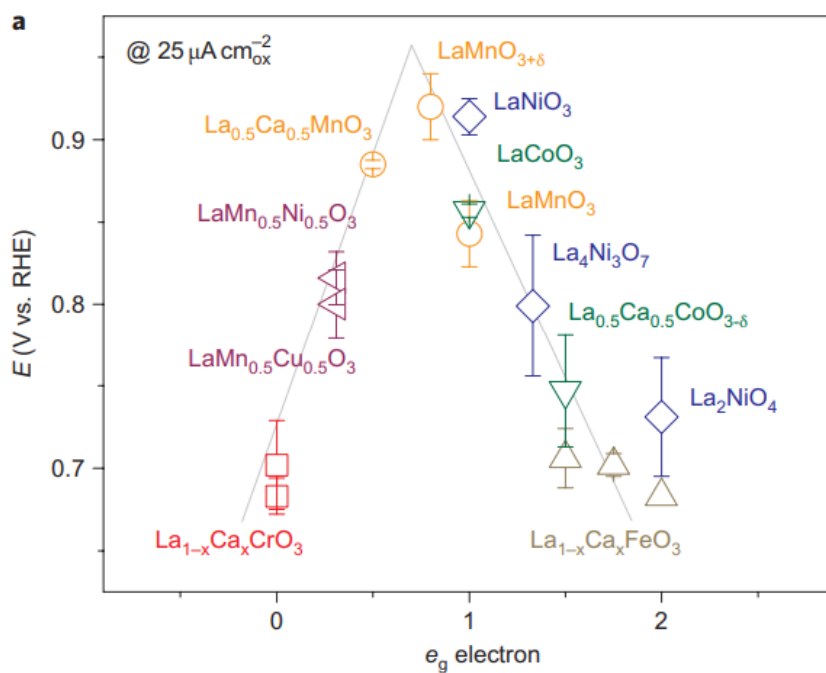


Figure 2.4 ORR volcano plot [72].

The detailed DFT study of the ORR kinetics and mechanisms with electron transfer steps requires the methods beyond the thermodynamic approach. It challenges for the simulation of the reactions at the constant potential, but not at the constant charge. Additionally, the solvent effects should be accurately estimated. The extensive research was targeted at these challenges. The models based on implicit solvent with countercharge placed in the conductor [144], [145] or in the localized planar region [146] near the electrode surface, homogeneous background charge [147], and supercell-size extrapolation [148], [149] were proposed to simulate charged surfaces, having their own limitations [148], [149]. The significant progress in both explicit and implicit continuum solvent models was achieved. The following comprehensive review provides the details [150]. However, the remaining challenges make them difficult for the off-the-shelf implementation to study the ORR kinetics. Therefore, the accurate DFT-level of study of ORR kinetics is far from being achievable and is a matter of further research.

The uncertainty in DFT-based predictions may arise from different sources such as the level of details in solvent simulations [151], the choice of the exchange-correlation functional [152], and core electron treatment [153]. It was shown that the irreducible uncertainty in the ORR reaction intermediates binding energies is ca. 0.2 eV [154]. One can see the uncertainties in bonding energies computed by various DFT software with different exchange-correlation functionals and pseudopotentials in Figure 2.5.

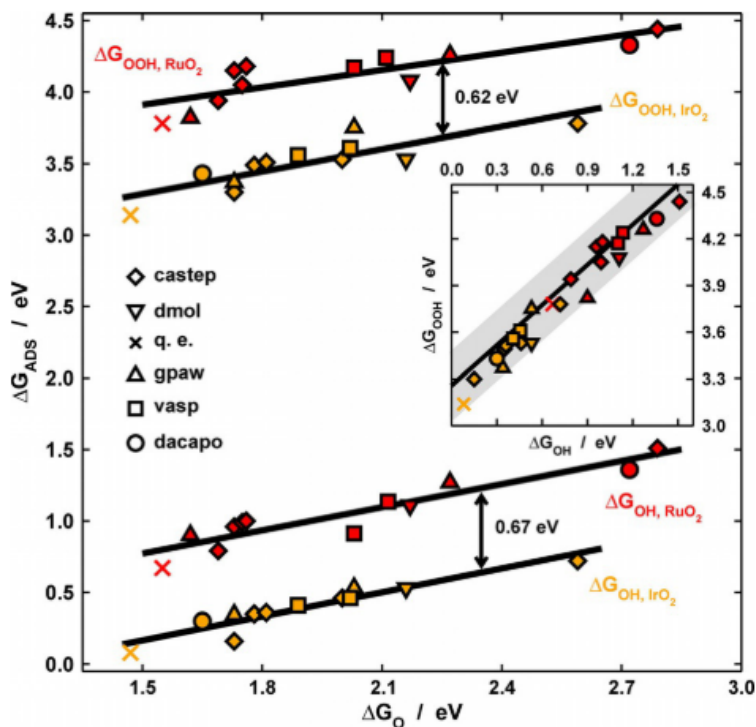


Figure 2.5 Adsorption energies of  $OH_{ads}$  and  $OOH_{ads}$  as a function of adsorption energies of  $O_{ads}$  on  $RuO_2$  and  $IrO_2$ . Grey area covers a range of  $\pm 0.2$  eV [153]

Considering the thermodynamic approach, one can calculate the equilibrium constants for the reaction steps to eliminate either forward or backward rate constant. However, the uncertainty of 0.2 eV in relative bonding energies will cause the uncertainty of  $\sim 10^4$  in fixed rate constant value at room temperature estimated from Arrhenius-type dependence. The DFT-based kinetics study of electrochemical reactions is even more complicated. One can hardly expect that state of the art methods can provide lower uncertainties for the single

rate constants. Therefore, the thermodynamic DFT approach can be useful for comparative catalyst analysis for ORR, but its results should be compared in a quantitative or a qualitative way with experimental data through the mesoscale simulations due to the high inherent uncertainties. Ideally, all sources of uncertainty should be quantified and used to refine the reaction mechanism, guide the further *ab initio* simulations/development of methods, and experimental studies.

### 2.2.3. Uncertainty quantification

#### 2.2.3.1. Uncertainty sources classification

There are many sources and types of uncertainties unavoidably introduced within the multiscale modeling approach from both experimental and modeling sides. According to Oberkampf and Roy [155], one can distinguish the aleatory and epistemic types of uncertainties. The first one is the uncertainty introduced by the inherent randomness and thus irreducible, which brings the necessity of its quantification. The second one is attributed to a lack of knowledge. It represents the bias between our understanding and the actual physical nature of the process under study. In principle, it can be minimized.

As the models are the central part of the multiscale modeling approach, one needs to classify the sources of uncertainties within them to elucidate the limitations they introduce. One of the classification patterns can be represented as follows [155], [156]:

#### 1. Model input uncertainty

It refers to the uncertainty of the data, which was used to build up the model. It can be further subdivided to the parameter and experimental uncertainties:

##### ○ Parameter uncertainty

This is the uncertainty in the input model parameters, which are estimated from additional experiments/calculations and used to perform the simulations (e.g. rate constants, bulk concentrations, diffusion coefficients, kinematic viscosity in MF-MKM). This uncertainty and its influence on the output of the model are usually neglected. However, the lower bound for the uncertainty of some model parameters may be estimated

from the chemical accuracy of thermochemical quantities ( $\sim 1$  kcal/mol), which is the typical error in corresponding experiments.

- Experimental uncertainty

This is the uncertainty of the experimental measurements, which model aims to fit/reproduce (e.g. measured current and potentials values for voltammograms in RRDE experiment), or which are used to constrain the model (e.g. equilibrium potentials). Even in the absence of the systematic bias (e.g. originating from wrong experimental design), it always exists in experiments due to the combination of independent, random sources (e. g. variation in catalyst synthesis procedure, catalyst loadings in ORR RDE experiments,  $\text{CH}_2\text{O}_2$ -in HPRR/HPOR experiments). In principle, it can be minimized by increasing the number of independent measurements and averaging according to the central limit theorem. Still, it is the time-consuming procedure in electrochemistry, so often the triplicate measurements are carried out. Hence, this type of uncertainty is non-negligible and should be taken into account when drawing conclusions from the model.

- 2. Model form uncertainty

It accounts for the uncertainty in assumptions and approximations used to construct the model. Usually, its minimization is of first priority in the multiscale modeling approach. One needs to use the model which describes the essential physics of the process in order to make use of the conclusions from it. But it should be firstly decoupled from the other sources of uncertainty in order to be elucidated. Model form uncertainty can be further divided into the structural and interpolation/extrapolation uncertainties.

- Structural uncertainty

It is due to the lack of knowledge of underlying physics. For example, the missing  $\text{HO}_2^-$  desorption step in simulated ORR mechanism on perovskite composite materials may lead to the wrong ring currents provided by the model. Another example is that the microkinetic model with Langmuir adsorption isotherm for Pt in acidic media at low overpotentials would not be able to reproduce the experimental Tafel slopes [57].

- Interpolation and extrapolation uncertainty

It refers to the lack of experiments in a required condition, so the results of the available experiments should be extrapolated/interpolated. This procedure also introduces uncertainty via the physical models required to accomplish it. One can consider the recalculation of rate constants using the Arrhenius-type equation in chemical kinetics as an example.

At some point, it may be also addressed to the parameter uncertainty.

### 3. Numerical uncertainty

This is the uncertainty provided by the numerical simulation of the given physical problem. Typically, careful convergence tests make it negligible, comparing with other sources of uncertainty.

Various methods are available for the solution of uncertainty quantification (UQ) problems, which are formulated and extensively studied for many practical applications, such as signal processing [157], structural reliability [158], oceanic oil-spill simulations [159], and kinetic modeling of combustion processes [156]. The models employed in the latter are similar to the microkinetic models but typically have a higher number of model parameters. Therefore, the UQ methods, commonly employed in this area, should be applicable to the MF-MKM.

There UQ problems can be subdivided into the two types.

#### *2.2.3.2. Forward uncertainty propagation problem.*

Given the uncertainties and values of model parameters, one needs to estimate the uncertainty it brings to the simulation of the experimental data. Its solution directs the research to refine the model parameters which influence the most the accuracy of the model. After that, the model form uncertainty can be reduced via the analysis of its bias against the experimental data. This approach synergizes with the bottom-up multiscale modeling. The uncertainty propagates from the first-principles calculations to the mesoscale models through the estimated model parameters.

The forward uncertainty propagation treatment for ORR is of the scope of this work. However, one can find below a brief overview of the methods addressed to solve this problem.

### 1. Taylor series-based methods

The model prediction  $y$  is expressed as a Taylor expansion vs. the standardized stochastic model parameters  $\mathbf{x}$  with prescribed uncertainty [156].

$$y = y_0 + \mathbf{g}^T \mathbf{x} + \mathbf{x}^T \mathbf{H} \mathbf{x} + h.o.t \quad (2.54)$$

Here  $\mathbf{g}$  - is the gradient,  $\mathbf{H}$  – Hessian. The uncertainty of the  $y$  can be then recalculated from the uncertainties of  $\mathbf{x}$ . However, this approach works fine only for the uncorrelated or perfectly correlated [160] model parameters.

### 2. Polynomial chaos expansion

The polynomial chaos expansion (PCE) was developed by Wiener [161]. The polynomial chaos basis consists of the set of basis random variables  $\xi$  and basis polynomials  $\psi(\xi)$ , which are orthogonal. In the case if  $\xi$  is a normal random variable with zero mean and unit variance,  $\psi(\xi)$  are Hermite polynomials. Various alternative bases exist [162]. The Taylor expansion is PCE with polynomial basis functions. According to the Cameron-Martin theorem [163], any random variable can be approximated with required precision by PCE with appropriate size  $P$ :

$$y = \sum_{i=0}^P y_i \psi_i(\xi) \quad (2.55)$$

### 3. High-dimensional model representation

It was introduced by Sobol [164] and found its application in chemical kinetics [165]. The model output is expressed as the set of the component functions and believed to better represent the model output than the Taylor series for an arbitrary function.

$$y = y_0 + \sum_{i=0}^n y_i(x_i) + \sum_{i=1}^{n-1} \sum_{j=i-1}^n y_{ij}(x_i x_j) + h.o.t. \quad (2.56)$$

The detailed information on the practical application of this method can be found elsewhere [165].

### 4. Intrusive methods

The intrusive methods require the modification of the governing equations in order to enable the analytical treatment of uncertainty propagation. The common methods from this

class applied to chemical kinetics are stochastic spectral projection [166] and sensitivity-analysis-based [167] methods, which provide the analytical calculations of coefficients in PCE and Taylor expansion respectively.

#### 5. Non-intrusive methods

These methods do not require the reconstruction of the governing equations. The representative non-intrusive methods are solution mapping [168], non-intrusive spectral projection [166], random-sample high-dimensional model representation [165], and Monte-Carlo integration [169].

##### 2.2.3.3. Inverse uncertainty propagation problem

The model is fitted to the experimental data and its uncertainty by the model parameters within their uncertainty bounds. Ideally, this procedure should tighten the bounds for model parameters, given the sufficient experimental dataset. The model parameters which still have high uncertainty are to be selected for further study in the additional experiments/simulations. This uncertainty propagation problem collaborates with the top down multiscale modeling approach. The experimental uncertainty provides the initial structural and parameter uncertainty for the microkinetic model and directs the further *ab initio* studies. The problem is, that there will be never enough experimental data to fully invert the microkinetic models in electrochemistry for the complex multistep reactions. Therefore, the inverse problem may become ill-posed. Even small errors (i.e. uncertainty) in experimental data can cause many orders of magnitude uncertainty for the estimated model parameters. Only simplified but physically correct models can provide reasonably low bounds for the model parameters or their combinations. However, the state of the art *ab initio* methods also provide high uncertainty in estimated model parameters, which is discussed in the corresponding section. Therefore, the both uncertainty propagation problems should be combined in order to elucidate the ORR mechanism.

The inverse uncertainty propagation problems are studied using Bayesian methods [170]. Given the uncertain model parameters  $\boldsymbol{x}$  with assigned prior probability density function (PDF)  $p(\boldsymbol{x})$  on accessible space  $K^n$ , experimental measurements  $\boldsymbol{y}^{obs}$  with their uncertainty  $\boldsymbol{\sigma}^{obs}$ , and the likelihood function  $\pi(\boldsymbol{y}^{obs}, \boldsymbol{\sigma}^{obs} | \boldsymbol{x})$ , one needs to obtain posterior

PDF  $p^*(\mathbf{x}|\mathbf{y}^{obs}, \boldsymbol{\sigma}^{obs})$  for the model parameters. The likelihood represents the probability of the measured experimental data to be observed due to the given model parameters. The posterior PDF gives the probability of the set of model parameters to give the measured experimental data. It can be calculated using the well-known Bayes' theorem:

$$p^*(\mathbf{x}|\mathbf{y}^{obs}, \boldsymbol{\sigma}^{obs}) = \frac{p(\mathbf{x})\pi(\mathbf{y}^{obs}, \boldsymbol{\sigma}^{obs}|\mathbf{x})}{\int_{K^n} p(\mathbf{x})\pi(\mathbf{y}^{obs}, \boldsymbol{\sigma}^{obs}|\mathbf{x})d\mathbf{x}} \quad (2.57)$$

The denominator is called evidence function. It ensures the normalization of the posterior PDF. Equation (2.57) is hard to evaluate. The following classes of methods are used to address this issue.

1. Bayesian analysis

It requires the assumption in the form of prior and likelihood PDFs. [170] In some cases, e.g. if experimental measurements and model parameters are jointly normally distributed and independent, the posterior PDF can be analytically evaluated. Unfortunately, in the practical models, it is often hard to make such assumptions. Therefore, one needs to use the methods which do not directly incorporate them.

2. Markov chain Monte Carlo methods

The Markov chain Monte Carlo (MCMC) methods are used to directly sample from posterior PDF. They generate the Markov chains, which have target distribution as their equilibrium distribution. The principles of MCMC sampling can be explained based on commonly used Metropolis algorithm [171]:

- a. Initialize the initial set of the model parameters  $\mathbf{x}_0$ , chosen (e.g. by random) within the  $K^n$
- b. Evaluate the  $p(\mathbf{x}_0)\pi(\mathbf{y}^{obs}, \boldsymbol{\sigma}^{obs}|\mathbf{x}_0)$
- c. Propose the new model parameters  $\mathbf{x}_1$  from the symmetric distribution  $g(\mathbf{x}_1|\mathbf{x}_0)$  with the center in  $\mathbf{x}_0$  and evaluate  $p(\mathbf{x}_1)\pi(\mathbf{y}^{obs}, \boldsymbol{\sigma}^{obs}|\mathbf{x}_1)$
- d. Accept the new model parameters with the probability of  $\min(1, \frac{p(\mathbf{x}_1)\pi(\mathbf{y}^{obs}, \boldsymbol{\sigma}^{obs}|\mathbf{x}_1)}{p(\mathbf{x}_0)\pi(\mathbf{y}^{obs}, \boldsymbol{\sigma}^{obs}|\mathbf{x}_0)})$ .
- e. Choose the accepted model parameters as the initial ones.

f. Repeat b.-e. until N sets of model parameters are generated.

The use of non-symmetric distribution for the selection of the next point of model parameters was later accounted for within the Metropolis-Hastings algorithm [172]. The MCMC methods require burn-in (i.e. discarding a certain number of first accepted samples to avoid outliers from the low probability region) to reach the equilibrium distribution, which is independent on the  $\mathbf{x}_0$  selection. Additionally, the  $g$  should be selected to minimize both the rejection rate and correlation between the sets of accepted model parameters. The high dimensionality of model parameters space is also leading to the excessive computational costs to converge to the posterior PDF. These issues have been addressed by extensive studies over the last few decades [173]. Still, the MCMC methods are very computationally demanding.

### 3. Data collaboration

These methods [174], [175] do not require the explicit PDF to solve (2.57). It is assumed that both  $p(\mathbf{x})$  and  $\pi(\mathbf{y}^{obs}, \boldsymbol{\sigma}^{obs} | \mathbf{x})$  follow the interval distributions  $K^n$  and  $D^n: \{\mathbf{y}^{obs} - \boldsymbol{\sigma}^{obs} < \mathbf{y}(\mathbf{x}) < \mathbf{y}^{obs} + \boldsymbol{\sigma}^{obs}\}$  respectively. The bond intervals  $F^n$  for model parameters are estimated as  $F^n = K^n \cap D^n$ .

Due to the high dimensionality of the model parameter space, one needs to use the adaptive methods to reduce the computational cost for the estimation of  $D^n$ . One of the promising methods is the non-parametric tree-structured Parzen estimator (TPE) method [176]. It is successfully applied in machine learning as an active learning method for global optimization of model parameters in multiple object tracking [177], the acquisition of the potential energy surfaces by optimized machine learning models [178], and many other applications [179]. TPE is also advantageous for the excessive parameters space sampling because of its linear scaling both with the size of the dataset on preceding attempts during the optimization step and dimensionality of model parameters space [176], [180], [181].

#### 2.2.4. Summary

In conclusion, the multiscale modeling approach is a powerful method to study the mechanism of complex heterogeneous electrochemical reactions. State of the art *ab initio*

numerical methods cannot be used to accurately describe the reaction kinetics due to the high inherent uncertainty of numerical methods and approximations. They still provide valuable insights from the comparative analysis of catalysts. Their combination with the macroscale simulations should provide better bounds on the proposed mechanism. At first approximation it can be achieved by semi-quantitative comparison. The more promising (and complicated) way to gain additional insights is to quantify all sources of uncertainty and its propagation within the multiscale modeling approach. The inverse uncertainty propagation problem solution is crucial to better couple the experiments with the *ab initio* simulation results through the macroscale models. The data collaboration methods are the most promising option for the initial assessment of the model parameters uncertainty since they do not make any assumptions on prior and likelihood PDFs. Their output may be further used as the input for the more computationally-demanding MCMC methods. One may then provide the accurate estimation of the posterior PDF and hence the uncertainty of the model parameters.

### 2.3. Thesis outline

Chapter 3 is dedicated to the rationalization of the catalytic activity difference for ORR between the most ( $\text{Mn}_2\text{O}_3$ ) and the least active ( $\text{MnOOH}$ ) oxides in alkaline media. The capability of the conventional *ab initio* thermodynamics approach to explain the experimentally observed difference is addressed. Combined with the complementary quantum chemical calculations of activation barriers and MF-MKM, the relevance of the outer-sphere ORR mechanism is elucidated. It calls for the uncertainty quantification for all inherent sources in order to reliably determine whether ORR proceeds by the inner or outer-sphere pathways.

Chapter 4 aims to elucidate the individual contributions of the carbon support and the perovskite oxide series  $\text{La}_{1-x}\text{Sr}_x\text{CoO}_{3-\delta}$  (LSCO) in ORR by MF-MKM to understand the required complexity of the overall ORR mechanistic pathway, which should be capable to explain the synergistic effects in the carbon-supported perovskite composite systems.

Chapter 5 shows the framework for the ORR mechanism selection using not only the precision of the experimental data fitting within the MF-MKM but also the uncertainty quantification of the model parameters. The CNTs are used as the model system since they require simpler ORR reaction mechanisms to describe the ORR kinetics, being compared with the TMO/C or Pt/C materials.

Chapter 6 aims to reduce the model form uncertainty for the ORR mechanism on CNTs by linking the microkinetic models, including the effective multi-electron transfer steps with the one-electron step mechanism within the RDS approximation.

Chapter 7 draws the summary and conclusions from Chapters 3-6.

### Chapter 3. Multiscale Modeling for ORR Mechanism on Manganese Oxides

This chapter is based on the results reported in the publication [V. A. Nikitina, A. A. Kurilovich, A. Bonnefont, A. S. Ryabova, R. R. Nazmutdinov, E. R. Savinova, G. A. Tsirlina. ORR on Simple Manganese Oxides: Molecular-Level Factors Determining Reaction Mechanisms and Electrocatalytic Activity. *J. Electrochem. Soc.*, 2018 Jan 1;165(15): J3199-208.]. The work is dedicated to the elucidation of the nature of the ORR elementary steps catalyzed by Mn oxides and the origin of the structure sensitivity. The  $\text{Mn}_2\text{O}_3$  and  $\text{MnOOH}$  samples are used to refine the ORR mechanism with respect to the TMO component due to the pronounced difference in ORR and HPRR and the availability of high-quality experimental data. The ORR RRDE experimental data with a number of complementary computational approaches were used to get the information on the surface composition and structure of the most ( $\alpha\text{-Mn}_2\text{O}_3$ ) and the least ( $\gamma\text{-MnOOH}$ ) active Mn oxides, and to provide comparative analysis regarding adsorption and reactivity of  $\text{O}_2$  and intermediate dioxygen species on their surfaces. The  $\alpha\text{-Mn}_2\text{O}_3$  (111) crystal plane is considered, as it is observed by transmission electron microscopy with atomic resolution [79]. For  $\gamma\text{-MnOOH}$ , the most likely (110) plane is studied. The author's main contribution is the periodic DFT calculations for ORR on  $\alpha\text{-Mn}_2\text{O}_3$  (111) and  $\gamma\text{-MnOOH}$  (110).

#### 3.1. Materials and methods

##### 3.1.1. Chemicals

$\text{MnOOH}$  (manganite, surface  $55 \text{ m}^2\cdot\text{g}^{-1}$  from Brunauer–Emmett–Teller analysis (BET)) was synthesized according to [182] and used as a precursor for the preparation of other Mn oxides. Three samples of  $\text{Mn}_2\text{O}_3$  (bixbyite) were studied. The sample with the BET surface area of  $25 \text{ m}^2\cdot\text{g}^{-1}$  was obtained by the heat treatment of  $\text{MnOOH}$  in air at  $240 \text{ }^\circ\text{C}$ . The sample with the BET surface area of  $27 \text{ m}^2\cdot\text{g}^{-1}$  was obtained by calcination of an amorphous product of comproportionation of  $\text{Mn}(\text{CH}_3\text{COO})_2$  and  $\text{KMnO}_4$  in air at  $550 \text{ }^\circ\text{C}$  for 12 h, [183] its electrochemical and electrocatalytic properties were discussed in [79].  $\text{MnO}_2$  (pyrolusite,  $48 \text{ m}^2/\text{g}$ ) was fabricated by the heat treatment of  $\text{MnOOH}$  at  $600 \text{ }^\circ\text{C}$ .  $\text{Mn}_3\text{O}_4$  (hausmannite,  $13 \text{ m}^2\cdot\text{g}^{-1}$ ) was obtained by the heat treatment of  $\text{MnOOH}$  in argon

atmosphere at 600 °C. According to the XRD data, all samples were pure phases and did not contain crystalline impurities. The synthesis and characterization of the samples of Mn oxides were performed by S.Y. Istomin. Carbon of the Sibunit family with the BET and BJH (Barrett-Joyner-Halenda method) surface areas equal to 65 and 52 m<sup>2</sup>·g<sup>-1</sup>, respectively, was kindly provided by Dr. P.A. Simonov.

### *3.1.2. Electrochemical characterization*

The electrochemical measurements were carried out by A. S. Ryabova. They were performed in 1 M NaOH electrolyte prepared from Acros Organics 50 wt. % aqueous solution in a three-electrode cell at 25 °C using Autolab potentiostat (PGSTAT302N) equipped with an analog scan generator. All parts of the electrochemical cell in contact with the alkaline electrolyte were from Teflon. The RRDE tip comprised a glassy carbon (GC) disc and a Pt ring. Sibunit carbon-oxide compositions with the 1:1 (wt.) ratio were deposited on the GC disc as described in [79] to achieve oxide loadings of 23, 30, and 91 µg per cm<sup>2</sup> of the GC disc. Potentials were measured versus HgO/Hg (IJ Cambria Scientific) in the same solution and recalculated to the reversible hydrogen electrode (RHE) scale (+0.93 V vs. RHE at 25 °C). The area of the Pt counter electrode was ~ 6 cm<sup>2</sup>. The electrolyte resistance determined from the high frequency part of the electrochemical impedance spectra (measured in the 1 Hz to 100 kHz range) was equal to ca. 15 Ω. The experimental curves were not corrected for the uncompensated ohmic resistance, as such correction would not result in any noticeable changes of the current-potential curves. The potential at the ring was +1.23 V. Calibration of the RRDE was performed using ferro-ferricyanide redox couple. Experimental collection factor of 0.25 was in good agreement with the theoretical value.

## **3.2. Theoretical basis**

### *3.2.1. Periodic DFT calculations*

Collinear spin-polarized periodic DFT calculations were performed using the VASP program package [184] with PAW [185] pseudopotentials and the RPBE-GGA functional

[134]. The 3d4s(ZVAL=7), 2s2p(ZVAL=6), and 1s(ZVAL=1) electrons were treated as valence ones for the Mn, O, and H, respectively. The asymmetric four Mn-layer supercells which mimic the MnOOH (110) (8 surface Mn atoms) and Mn<sub>2</sub>O<sub>3</sub> (111) (16 surface Mn atoms) surfaces were constructed from the corresponding bulk structures. The cubic  $Ia\bar{3}$   $\alpha$ -Mn<sub>2</sub>O<sub>3</sub> bulk structure was used as a stable one at experimental conditions [186]. An energy cutoff of 600 eV and 2x2x1 (Mn<sub>2</sub>O<sub>3</sub>) and 3x2x1 (MnOOH) *k*-point meshes were used in all the calculations. The dipole corrections were applied in the direction perpendicular to the surfaces. Only one surface layer together with the adsorbed intermediates were relaxed until the change in the total energy of the system was less than 10<sup>-3</sup> eV. The obtained lattice parameters for cubic  $\alpha$ -Mn<sub>2</sub>O<sub>3</sub> are: a=b=c=9.59205 Å,  $\alpha=\beta=\gamma=90.0^\circ$ . For  $\gamma$ -MnOOH: a=5.44060, b=5.50974, c=5.45707 Å;  $\alpha=90.0^\circ$ ,  $\beta=114.7^\circ$ ,  $\gamma=90.0^\circ$ . These parameters are within 10% to the experimental values [187], [188]. The ferromagnetic ground state was obtained for  $\alpha$ -Mn<sub>2</sub>O<sub>3</sub>, which coincides with the results reported by Franchini et. al. [189]. The ferromagnetic ground state for  $\gamma$ -MnOOH was calculated. The optimized bulk structures were then used to construct the surfaces with the ferromagnetic spin configuration. The more detailed calculations of the  $\alpha$ -Mn<sub>2</sub>O<sub>3</sub> ground state magnetic structure require the DFT+U formalism, which was not adopted in calculations due to the reasons discussed below.

Active surfaces of Mn<sub>2</sub>O<sub>3</sub> (111) and MnOOH (110) oxides were constructed implying 0.5 monolayer (ML) O<sub>ad</sub> and 0.5 ML HO<sub>ad</sub> coverages. Under experimental conditions, these coverages correspond to somewhat different overpotentials. However, this potential shift is not sufficient to explain the pronounced difference in the oxides' electrochemical activities towards oxygen reduction. The possible partial coverage of the surfaces with water molecules was addressed neither in the periodic DFT calculation nor in the MF-MKM, as the primary effect is believed to be related largely to the differences of Mn oxides reactive centers configuration and not to the differences in the specifics of the oxide-water interaction (which is the inevitable assumption on the current stage due to the prohibitive size of the periodic slabs required to study these effects on MnOOH and Mn<sub>2</sub>O<sub>3</sub> surfaces).

In all the calculations a 20 Å vacuum region was introduced to avoid the interaction between the slabs.

The DFT+U approach is not followed in periodic DFT calculations, which in some cases allows for a more accurate account of the oxides' electronic structure and its effect on the geometry of adsorbates and the energetics of adsorption. However, the DFT+U approach is not universal, and has some shortcomings that may cause inaccuracy in computed energies and geometrical parameters (see discussion in [190], [191]). Indeed, for Mn<sub>2</sub>O<sub>3</sub> oxide PBE+U tends to overestimate the equilibrium volumes and also it favors a half-metallic state, rather than an insulating character as derived from the hybrid functional approaches [189].

The long-range van der Waals interactions were not taken into account within the framework of periodic DFT. Different approaches exist to incorporate them, though they have their own shortcomings [192], [193]. They require excessive testing for the studied system, which is beyond the scope of this work. However, one might expect that the introduction of the long-range interactions would stabilize the ORR intermediates on the electrode surface ca. 0.1-0.2eV [194]. The relative change in binding energies is lower than for the absolute values. Therefore, one can believe that it would not qualitatively alter the results presented in this chapter.

The thermodynamics of electrochemical reactions was addressed by means of a computational standard hydrogen electrode approach [9], [10] (3.1).

$$G_{(OH^- - e^-)} = G_{H_2O(g)} - eU - \frac{1}{2}G_{H_2(g)} \quad (3.1)$$

Zero-point energy (*ZPE*) and entropic corrections (*TS*) were introduced to the calculated ground state energy  $E_{DFT}$ . in order to obtain free energies of adsorption  $\Delta G$  for the reactions involving ORR intermediates (3.2):

$$\Delta G = \Delta E_{DFT} + \Delta ZPE - T\Delta S \quad (3.2)$$

The contribution of pV term and configurational entropy was neglected. The *ZPE* was calculated from the vibrational normal modes  $\nu_i$  computed within the harmonic oscillator approximation [195] (3.3):

$$ZPE = \sum_i \frac{h\nu_i}{2} \quad (3.3)$$

The  $TS$  was accounted for the vibrational entropy contribution only for the adsorbed reaction intermediates. For the solvent molecules total entropy values were taken from the standard thermodynamic tables. Then the  $TS$  for adsorbed molecules can be expressed as follows [196]:

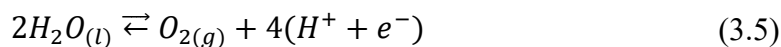
$$TS \approx Tk_b \sum_i \left[ \frac{\frac{h\nu_i}{Tk_b}}{\exp\left(\frac{h\nu_i}{Tk_b}\right) - 1} - \ln\left(1 - \exp\left(\frac{h\nu_i}{Tk_b}\right)\right) \right] \quad (3.4)$$

Here summation goes through all vibrational modes.  $k_b$  - is the Boltzmann constant,  $T$  - temperature in K,  $h$  - Plank constant. The computed  $TS$  and  $ZPE$  corrections are shown in Table 3.1.

Table 3.1 ZPE and TS corrections for the reaction intermediates at 298 K.

Species	TS, eV	ZPE, eV	ZPE - TS, eV
H <sub>2</sub> O(g) at 0.035 bar	0.67	0.57	-0.10
H <sub>2</sub> (g) at 1 bar	0.41	0.27	-0.14
-OH	0.00	0.28	0.28
-O	0.00	0.05	0.05
-OOH	0.01	0.39	0.38
-OO	0.01	0.10	0.09

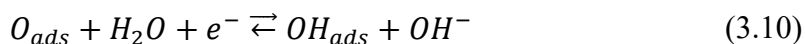
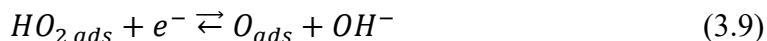
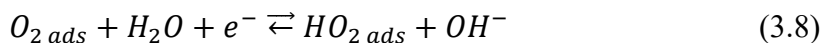
The high-spin ground state of the oxygen molecule is poorly described by DFT [9]. Therefore, the correct value of chemical potential for the oxygen molecule  $\mu_{O_{2(g)}}$  (1 bar, 298 K) was obtained from the free energy change of 4.92eV (pH=0, U = 0 V vs. SHE) for the reaction (3.5):



The equilibrium of the liquid water  $H_2O_{(l)}$  with the gaseous water  $H_2O_{(g)}$  (0.035 bar, 298 K) and CHE (2.53) were used to obtain the expression for  $\mu_{O_{2(g)}}$ :

$$\mu_{O_2(g)} = 4.92eV + 2\mu_{H_2O(g)} - 2\mu_{H_2(g)} \quad (3.6)$$

The following reaction pathway was considered to compute the free energy diagrams:



The adsorption energies for the reaction intermediates are calculated vs.  $H_2O_{(g)}$  (0.035 bar, 298 K) and  $H_{2(g)}$  (1 bar, 298 K):

$$\Delta G_{O_{2 ads}} = G_{O_{2 ads}} - G_* - \mu_{O_2(l)} \quad (3.12)$$

$$\Delta G_{HO_{2 ads}} = G_{HO_{2 ads}} - G_* - \mu_{O_2(g)} - \mu_{(OH^- - e^-)}(U) - \mu_{H_2O(g)} \quad (3.13)$$

$$\Delta G_{O_{ads}} = G_{O_{ads}} - G_* - \mu_{O_2(g)} - 2\mu_{(OH^- - e^-)}(U) - \mu_{H_2O(g)} \quad (3.14)$$

$$\Delta G_{OH_{ads}} = G_{OH_{ads}} - G_* - \mu_{O_2(g)} - 3\mu_{(OH^- - e^-)}(U) - 2\mu_{H_2O(g)} \quad (3.15)$$

The calculated adsorption energies for reaction intermediates are shown in Table 3.2

Table 3.2 Adsorption energies of reaction intermediates on  $Mn_2O_3$  and  $MnOOH$  vs.  $H_2O_{(g)}$  and  $H_{2(g)}$ .

Reaction intermediate	Adsorption energy on $Mn_2O_3$ , eV			Adsorption energy on $MnOOH$ , eV		
	1.0 V vs. RHE	0.9 V vs. RHE	0 V vs. RHE	1.0 V vs. RHE	0.9 V vs. RHE	0 V vs. RHE
-OO	0.07	0.07	0.07	-0.03	-0.03	-0.03
-OOH	0.21	0.11	-0.79	0.34	0.24	-0.66
-O	-0.92	-1.12	-2.92	-0.92	-1.12	-2.92
-OH	-1.15	-1.45	-4.15	-0.90	-1.20	-3.90

### 3.2.2. Cluster DFT calculations

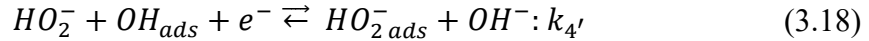
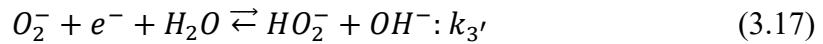
All cluster calculations were performed by V. A. Nikitina. They were carried out at the DFT level using the B3LYP functional as implemented in the Gaussian 09 program suite

[197]. The O and H atoms of the adsorbates and oxide clusters were described by the standard 6-311++G(d,p) basis set. The effect of inner electrons of the Mn atoms was included in a relativistic Effective Core Potential LanL2, while a basis of DZ quality was employed to describe Mn valence electrons. The spin-polarized Kohn-Sham formalism was used to treat the open-shell systems.

The clusters were constructed using the geometry of Mn<sub>2</sub>O<sub>3</sub> (111) and MnOOH (110) surfaces optimized using the periodic DFT. Each cluster contained 8 Mn atoms, with the two central Mn atoms mimicking the reaction center. The closest Mn atoms on the oxide surfaces were chosen as potential candidates for the reaction centers. The geometry of the active center and the positions of Mn and O atoms in the clusters were frozen during the optimization of adsorbates to keep the initial surface structure. A part of the O atoms was saturated by auxiliary hydrogen atoms to achieve electroneutrality at the model clusters. The ground state multiplicities for the Mn oxide clusters were determined to be 16 and 14 for Mn<sub>2</sub>O<sub>3</sub> and MnOOH clusters and 17 and 15 for the “cluster + O<sub>2ads</sub>” systems. The spin densities of the Mn atoms correspond to the anti-ferromagnetic state of the model clusters.

### 3.2.3. Mean-field microkinetic modeling details

The MF-MKM was carried out by A. Bonnefont for both inner-sphere and outer-sphere mechanisms. The MF-MKM with the inner-sphere mechanism is described in [79]. The outer-sphere mechanism was simulated using the following steps:



The carbon contribution was neglected due to the high catalytic activity of Mn<sub>2</sub>O<sub>3</sub> and MnOOH for ORR. The model assumes Langmuir adsorption/desorption of HO<sub>2</sub><sup>-</sup> on the surface of Mn oxides and Butler-Volmer kinetics for the electron transfer steps. The model considers the escape of O<sub>2</sub><sup>-</sup> and HO<sub>2</sub><sup>-</sup> from the diffusion layer in order to simulate the RRDE

current-potential curves. One can see the additional details on the model parameters and equations in [198]

### 3.3. Results and discussion

The experimental RRDE data was obtained by A. S. Ryabova (Figure 3.1). At all potentials and loadings, the hydroperoxide yield increases in the following order  $\text{Mn}_2\text{O}_3 < \text{MnO}_2 < \text{Mn}_3\text{O}_4 < \text{MnOOH}$ . It coincides with the HPRR limiting currents on these materials. As it was previously reported by Ryabova et. al. [79], the HPRR limiting currents below the diffusion-limiting ones were observed on  $\text{MnOOH}$  and  $\text{Mn}_3\text{O}_4$  at the broad potential range (Figure 3.2 (b-d)). They were explained by the chemical RDS for the hydroperoxide decomposition on those materials.

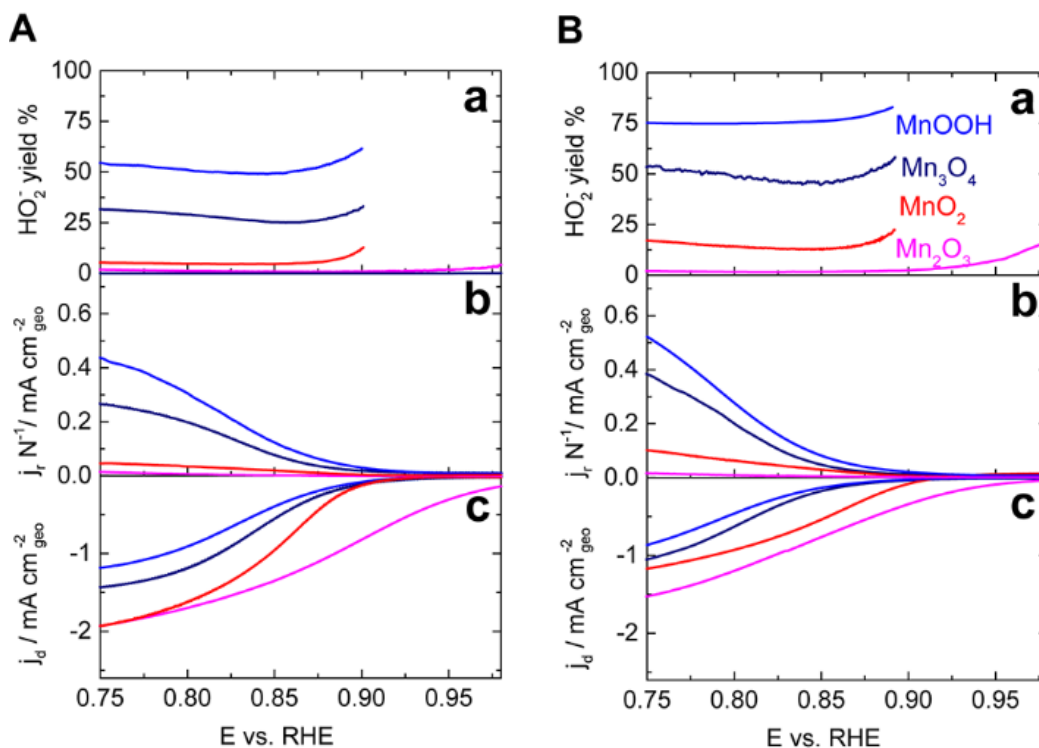


Figure 3.1 RRDE experimental data for manganese oxides. (a) Percentage of  $\text{HO}_2^-$  formed, (b) ring and (c) disk currents versus disk potential extracted from the positive scans of the RRDE voltammograms of GC-supported thin films of Mn oxides + Sibunit carbon in  $\text{O}_2$ -saturated 1 M NaOH at 900 rpm and  $10 \text{ mV} \cdot \text{s}^{-1}$ . Catalyst loadings:  $91 \mu\text{g} \cdot \text{cm}^{-2}_{\text{geo}}$  Oxide +

91  $\mu\text{g}\cdot\text{cm}^{-2}_{\text{geo}}$  Sibunit (A), 30  $\mu\text{g}\cdot\text{cm}^{-2}_{\text{geo}}$  Oxide + 30  $\mu\text{g}\cdot\text{cm}^{-2}_{\text{geo}}$  Sibunit (B). Disk currents are normalized to the geometric area of the electrode and corrected to the background currents measured in the  $\text{N}_2$  atmosphere. Ring currents are normalized to the geometric area of the disk electrode and to the collection factor.

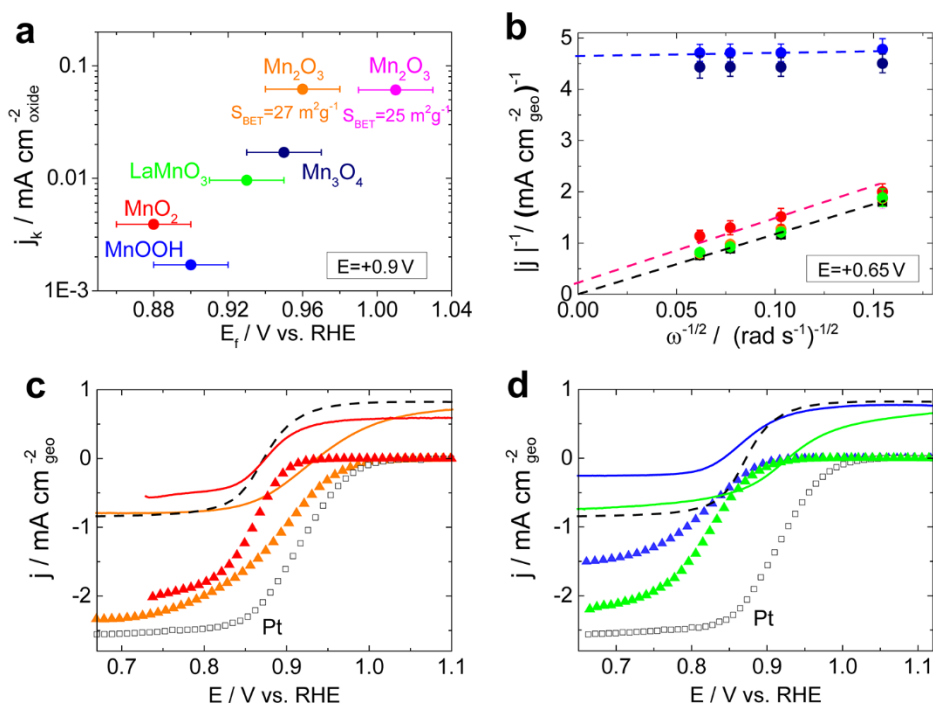


Figure 3.2 (a) Kinetic ORR currents at 0.9 V vs. RHE against the formal potential,  $E_f$ , of the surface Mn(IV)/Mn(III) redox couple. (b): Levich-Koutecky (LK) plots of the HPRR currents at 0.65 V vs. RHE. (c,d): RDE voltammograms in  $\text{N}_2$ -purged 1 M NaOH + 0.84 mM  $\text{H}_2\text{O}_2$  (solid lines) and  $\text{O}_2$ -saturated 1 M NaOH blue (MnOOH), orange ( $\text{Mn}_2\text{O}_3$ ,  $S_{\text{BET}} = 27\text{m}^2\text{g}^{-1}$ ), green (LaMnO<sub>3</sub>), red (MnO<sub>2</sub>). Currents are normalized to the BET surface area of corresponding oxides (triangles) at 900 rpm and  $10\text{mV s}^{-1}$ . Catalyst loadings on the GC electrode are  $91\ \mu\text{g cm}^{-2}$  manganese oxide +  $91\ \mu\text{g cm}^{-2}$  Sibunit carbon. Color codes: (a), and to the electrode geometric area (b-d). Error bars represent standard deviations from at least two independent repeated measurements. Data for Pt/C (black) is presented for comparison. Data is reproduced from [73], [79], [199]

All the materials except  $\text{Mn}_2\text{O}_3$  demonstrated the catalyst loading-dependent  $\text{HO}_2^-$  yield. The latter decreases at lower catalyst loadings, which correlates with the number of active sites available for hydroperoxide decomposition. The  $\text{Mn}_2\text{O}_3$  showed the loading independent negligible  $\text{HO}_2^-$  yield, even at the low-area samples (see supporting information in [198]). Therefore, the hypothesis of the “direct”  $4e^-$  ORR pathway (O-O bond breaking in the  $\text{O}_2$  reaction intermediate) on  $\text{Mn}_2\text{O}_3$  should be checked in addition to the fast hydroperoxide decomposition.

Periodic DFT calculations were used for estimating adsorption energies of the reaction intermediates:  $\text{O}_{2\text{ ads}}$ ,  $\text{HO}_{2\text{ ads}}$ ,  $\text{OH}_{\text{ads}}$ , and  $\text{O}_{\text{ads}}$  assumed within a “series” mechanism. These calculations allowed to assess surface restructuring of the two oxides, at least at a qualitative level. Given the large size of the  $\text{Mn}_2\text{O}_3$  (111) cell (190 atoms in the asymmetric cell) and the difficulties associated with accurate *ab initio* calculations for large systems, only one surface layer was optimized, which induces some degree of inaccuracy in the obtained geometries of the surfaces. The results should thus be treated as an initial guess of the surface reconstruction trends. Figure 3.2 shows the geometries of the optimized first layers of the Mn oxide surfaces. They are associated with the experimentally obtained formal potentials [79] of the  $\text{Mn(IV)=O}_{\text{ads}}/\text{Mn(III)-OH}_{\text{ads}}$  surface redox transition [200] on  $\text{MnOOH}$  and  $\text{Mn}_2\text{O}_3$ . It was observed both experimentally [75] and from the computed surface Pourbaix diagrams [201].

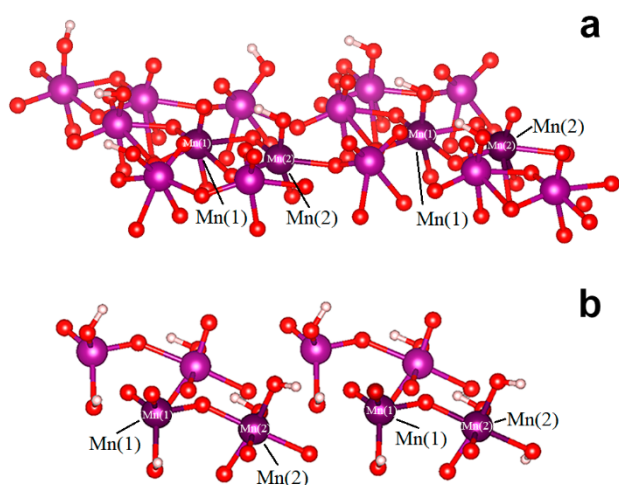
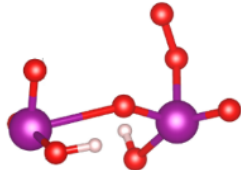
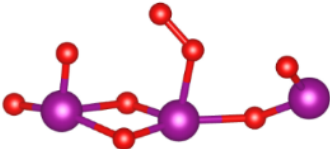
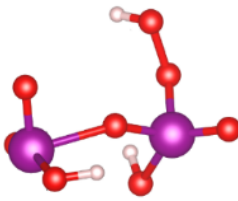
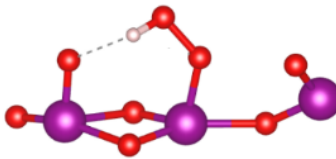
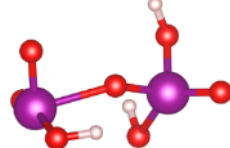
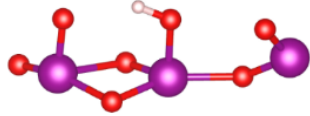


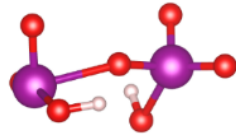
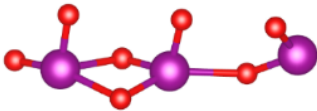
Figure 3.3 Surface layers of Mn<sub>2</sub>O<sub>3</sub> (a) and MnOOH (b) oxides (0.5 ML O<sub>ads</sub>, 0.5 ML OH<sub>ads</sub> coverage), as obtained from periodic DFT calculations.

The active centers, which are assigned to the closest Mn atoms, are marked in the Figure 3.2. Both surfaces show significant changes in the positions of Mn octahedra after the relaxation procedure. For MnOOH (110), the distance between Mn(1) and Mn(2) atoms (“active center”) is decreased from 3.76 to 3.49 Å, while other distances between the surface Mn atoms are increased by 0.2 – 0.4 Å. In the case of the Mn<sub>2</sub>O<sub>3</sub> (111) surface, the distance between the closest Mn(1) and Mn(2) atoms decreases from 3.16 Å to 2.98 Å, while other distances on the surface increase by 0.2-0.3 Å.

The intermediates of the ORR reaction (O<sub>2ads</sub>, HO<sub>2ads</sub>, OH<sub>ads</sub>, O<sub>ads</sub>) were placed on the Mn(2) atoms of the active centers. The subsequent geometry relaxation provided the structures of the O-containing adsorbates at the MnOOH and Mn<sub>2</sub>O<sub>3</sub> surfaces. Table 3.2 shows the geometries of the adsorbates and lists the corresponding bond lengths and angles in the structure.

Table 3.3 Adsorbate geometries on Mn<sub>2</sub>O<sub>3</sub> (111) and MnOOH (110) surfaces, as obtained from periodic DFT calculations. Atoms denoted by plain text and connected by dashes indicate the bond or angle, for which the value is shown.

System	Parameter	Value	Structure
MnOOH (110) –OO	Mn-O <sub>O</sub>	1.96 Å	
	Mn-O-O	1.27 Å	
	Mn-O-O angle	120.4°	
Mn <sub>2</sub> O <sub>3</sub> (111) –OO	Mn-O <sub>O</sub>	2.05 Å	
	Mn-O-O	1.27 Å	
	Mn-O-O angle	124.9°	
MnOOH (110) –OOH	Mn-O <sub>OH</sub>	1.80 Å	
	Mn-O-O <sub>H</sub>	1.43 Å	
	O-H <sub>OO</sub>	0.99 Å	
	MnOOH-O <sub>Mn</sub>	4.22 Å	
	Mn-O-O <sub>H</sub> angle	117.5°	
	Mn-O-O-H angle	100.1°	
Mn <sub>2</sub> O <sub>3</sub> (111) –OOH	Mn-O <sub>OH</sub>	1.83 Å	
	Mn-O-O <sub>H</sub>	1.40 Å	
	MnO-O-H	0.99 Å	
	MnOOH-O <sub>Mn</sub>	2.02 Å	
	Mn-O-O <sub>H</sub> angle	127.4°	
	Mn-O-O-H angle	105.0°	
MnOOH (110) –OH	Mn-O <sub>H</sub>	1.76 Å	
	Mn-O-H	0.98 Å	
	Mn-O-H angle	112.8°	
Mn <sub>2</sub> O <sub>3</sub> (111) –OH	Mn-O <sub>H</sub>	1.79 Å	
	Mn-O-H	0.98 Å	
	Mn-O-H angle	113.5°	

MnOOH (110) –O	Mn-O	1.60 Å	
Mn <sub>2</sub> O <sub>3</sub> (111) –O	Mn-O	1.60 Å	

The molecular oxygen is relatively weakly adsorbed on the model surfaces (see Table 3.2). The Mn-O<sub>ads</sub> distance for adsorbed oxygen is in the range of 1.96 – 2.05 Å. The HO<sub>2ads</sub> intermediate adopts different configurations upon adsorption at Mn<sub>2</sub>O<sub>3</sub> and MnOOH surfaces. In the case of Mn<sub>2</sub>O<sub>3</sub> a stabilizing interaction between the OH group of the peroxide moiety and the O<sub>ads</sub> adsorbate of the neighboring Mn atom can be noticed, which is absent for the MnOOH surface due to larger Mn-Mn distances. The bond lengths between Mn atoms and O<sub>ads</sub> (1.60 Å) and HO<sub>ads</sub> (1.76 – 1.79 Å) adsorbates are similar for the two surfaces.

In the framework of thermodynamic approaches, the free energy difference for the surfaces with various adsorbed intermediates is used to assess the kinetics of multistep processes without computing reaction activation energies [9], [10], [201], [202]. This simplification assumes a straightforward relationship between the activation energy and the reaction free energy, which is not obvious, especially for the inner-sphere steps. For the ORR, free energy diagrams are usually constructed for the reaction pathway involving successive interconversion of the adsorbed O<sub>2ads</sub>, HO<sub>2ads</sub>, OH<sub>ads</sub>, and O<sub>ads</sub> intermediates. Despite the thermodynamic approach remains a convenient and valid method for comparing adsorption energies of the intermediates and for the initial screening of potential catalysts, sometimes it fails to describe the experimental trends and to give correct predictions on the nature of the reaction limiting step [120], [203], [204].

The simplified procedure was adopted to evaluate the interaction energies of the ORR intermediates with the Mn oxide surfaces, which did not involve an extensive search for the minimum energy surface at a given potential with the account for the fractional

occupation of the surface by water molecules. Instead, the MnOOH (110) and Mn<sub>2</sub>O<sub>3</sub> (111) surfaces were used at 0.5 ML OH<sub>ads</sub> and 0.5 ML O<sub>ads</sub> coverages. The free energy diagrams were computed for the potentials, which correspond to these coverages based on the available experimental information (formal potentials of the two oxides). Under these conditions, the 0.5 O<sub>ads</sub> coverage corresponds to the potential of ca. 1.0 V for Mn<sub>2</sub>O<sub>3</sub> and 0.9 V for MnOOH [79]. The free energy diagrams for the two oxides, calculated for these potentials, are shown in Figure 3.3.

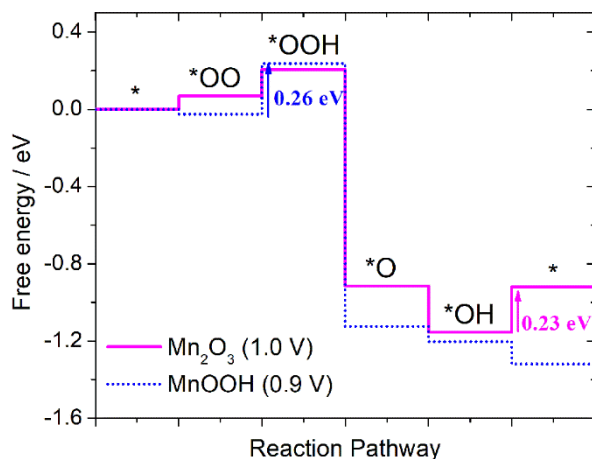


Figure 3.4 Free energy diagrams for MnOOH (110) and Mn<sub>2</sub>O<sub>3</sub> (111) at 0.9 and 1.0 V vs. RHE, respectively.

The free energy diagram suggests that for MnOOH the potential determining step (PDS) involves HO<sub>2ads</sub> formation from O<sub>2ads</sub>, while for Mn<sub>2</sub>O<sub>3</sub> the PDS could be attributed to the OH<sub>ads</sub> desorption step. While supporting the higher activity of Mn<sub>2</sub>O<sub>3</sub>, the thermodynamic approach fails to explain the most notable difference between the Mn<sub>2</sub>O<sub>3</sub> and the MnOOH oxide: kinetic limitation of the bond-breaking in HO<sub>2ads</sub> for MnOOH but not for Mn<sub>2</sub>O<sub>3</sub> evidenced in [79]. The contribution of long-range van der Waals interactions should not qualitatively alter the result due to the significant negative free energy change for the HO<sub>2ads</sub> bond-breaking step on both Mn<sub>2</sub>O<sub>3</sub> and MnOOH. This calls for a more detailed computational investigation of the hydrogen peroxide decomposition reaction, which

involves the bond breaking in the hydrogen peroxide intermediate and thus is likely to be associated with a high energy barrier at least at the MnOOH (110) surface.

The hypothesis of the outer-sphere ORR mechanism should be tested, as the low adsorption energies of O<sub>2</sub> on both MnOOH (-0.03 eV) and Mn<sub>2</sub>O<sub>3</sub> (0.07 eV) were obtained from the periodic DFT calculations. Additionally, in a number of publications the outer-sphere ORR mechanism was discussed on Au and Pt in alkaline media [205]–[207]. The first two steps of the outer-sphere ORR mechanism are (3.15), (3.16). The formed HO<sub>2</sub><sup>-</sup> can then be adsorbed on Mn active site (3.17) and decomposed (3.18).

As the author's main contribution to the work is the periodic DFT calculations, only the brief summary of results is shown for the quantum-chemical modeling of activation barriers for the elementary steps and microkinetic modeling. One can find a detailed description of the corresponding sections in the original paper [198].

The feasibility of “direct” ORR pathway on Mn<sub>2</sub>O<sub>3</sub> was accessed by the cluster calculations (in order to allow the treatment of the charged species) of the activation energies for O<sub>2</sub> and O<sub>2</sub><sup>-</sup> (as it has sufficient lifetime in alkaline media [208]) dissociative adsorption on two neighboring Mn atoms. The optimized geometries of Mn active sites were taken from periodic DFT calculations. All cluster calculations were performed by V. Nikitina. It was shown that the direct 4e<sup>-</sup> pathway is not feasible due to the prohibitive activation energies ca. 2.5eV for both O<sub>2</sub> and O<sub>2</sub><sup>-</sup> dissociative adsorption on Mn<sub>2</sub>O<sub>3</sub>.

Then the origin of the catalytic activity difference between the MnOOH and Mn<sub>2</sub>O<sub>3</sub> can be addressed by the faster bond breaking in the adsorbed HO<sub>2</sub><sup>-</sup> (3.18) on the Mn<sub>2</sub>O<sub>3</sub>. Figure 3.4 (a, b) shows the corresponding barriers for the bond breaking in HO<sub>2</sub><sup>-</sup> adsorbed at Mn<sub>2</sub>O<sub>3</sub> and MnOOH oxide surfaces, which were estimated as ca. 0.5 eV and 0.8 eV correspondingly. The geometries of transition states (lower panels of Figure 3.4) suggest that smaller distances between neighboring Mn atoms in Mn<sub>2</sub>O<sub>3</sub> allow for the existence of stabilizing interactions between O<sub>ads</sub> and OH<sub>ads</sub>, which facilitate the OH<sup>-</sup> detachment and decrease the activation barrier. For MnOOH such kind of interactions is unlikely, as the distance between the adjacent Mn centers is too large.

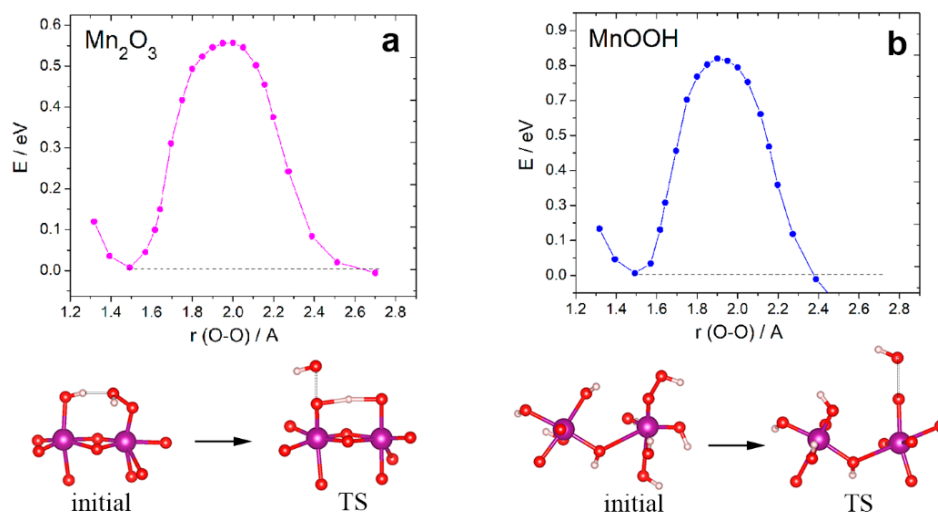


Figure 3.5 Energy curves for the bond breaking in  $\text{HO}_2^-$  at the  $\text{Mn}_2\text{O}_3$  (a) and  $\text{MnOOH}$  (b) clusters.

Therefore, one can conclude that adsorbate-adsorbate interactions may allow for a significant reduction of the bond breaking barrier height, which could determine the higher activity of  $\text{Mn}_2\text{O}_3$  with respect to the reduction of hydrogen peroxide species explaining the experimentally observed kinetically limited HPRR for  $\text{MnOOH}$  but not for  $\text{Mn}_2\text{O}_3$ . Note however, that the exact barrier heights should be taken with caution given the vast number of approximations and simplifications in performed cluster calculations.

The estimations of activation barriers of first two ET steps (3.15), (3.16) within the outer-sphere scenario were carried out by R. R. Nazmutdinov. The spinless Anderson-Newns model (narrow band formalism) [209], [210] was combined with DFT calculations to map the ET free energy along the solvent coordinate. The solvent reorganization energy was estimated to be  $\lambda=1.2$  eV [209]. Three geometries of the  $\text{O}_2$  approach to the active center (see Figure 3.5) of the model cluster were considered. The closest approach distance  $z_{\text{min}}$  provides the minimal energy values of the  $\text{O}_2$  approach (Figure 3.6).

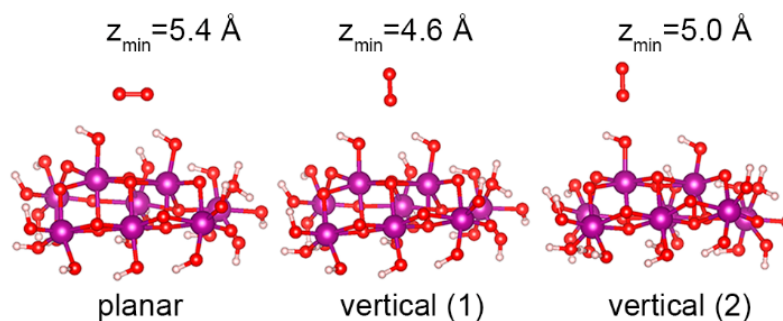


Figure 3.6 Selected orientations of O<sub>2</sub> molecule near the surface of model Mn<sub>2</sub>O<sub>3</sub> clusters.  $z_{\min}$  denotes the minimal energy values for the approach of O<sub>2</sub> to the cluster “surface”. “Planar” orientation corresponds to the O-O bond being parallel to the active center plane; “vertical (1)” – to the O-O bond normal to the cluster surface with the projection between the Mn(1) and Mn(2) atoms; “vertical (2)” – to the O-O bond normal to the cluster surface with the projection at the oxygen atom of OH<sub>ads</sub>.

The  $z_{\min}$  values for OH-terminated MnOOH and Mn<sub>2</sub>O<sub>3</sub> are 5.4, 4.6, 5.0 Å, and 5.4, 4.4, 5.5 Å for the planar, vertical(1), and vertical(2) geometries respectively. The influence of the surface OH vacancies and presence of O-terminated Mn active sites were also elucidated (see SI in [198] for more details). The “OH vacancies” were shown to decrease the  $z_{\min}$  thus lowering the ET activation barrier. The presence of O-terminated Mn active sites showed the repulsion effect (increased  $z_{\min}$ ) only in vertical(2) geometry. The  $z_{\min}$  is decreased in two other coordinations due to the shorter Mn-O distance being compared with Mn-OH distance.

The ET barriers were estimated for three O<sub>2</sub> orientations at the corresponding  $z_{\min}$  and hydroxylated Mn active sites. The “OH vacancies” are not considered as active sites are likely to be occupied by H<sub>2</sub>O or OH in alkaline media. The ET barriers on both oxides were estimated ca. 0.3 eV ( $\lambda/4$  in accordance with Marcus theory at zero overvoltage). The consideration of the first ET step as the outer-sphere is allowed by a modest activation barrier.

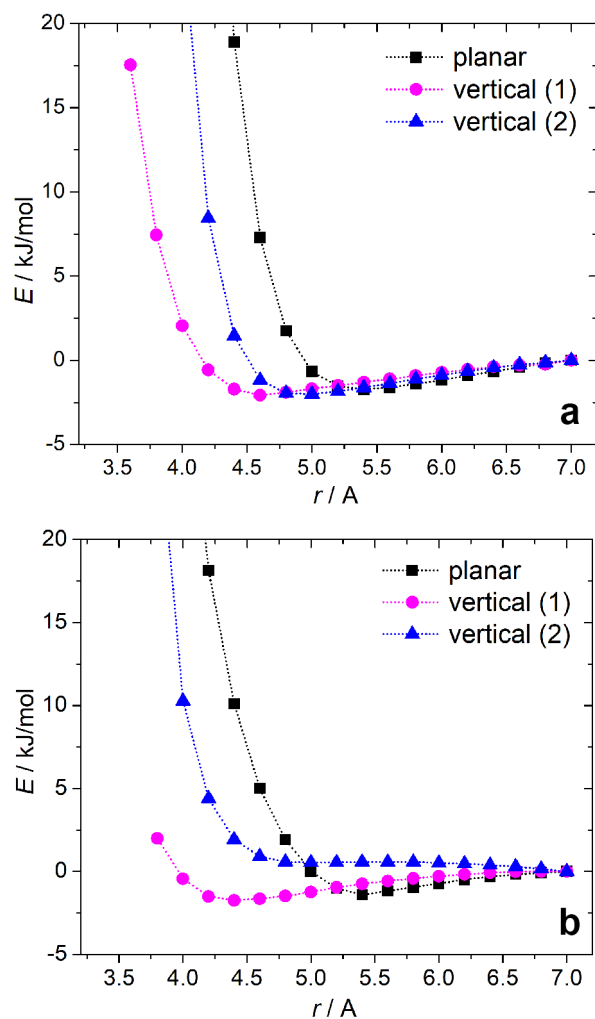


Figure 3.7  $O_2$  - cluster interaction energy curves for a set of three orientations of  $O_2$  molecule in the vicinity of hydroxylated  $Mn_2O_3$  (a) and  $MnOOH$  (b) surfaces.

The electronic transmission coefficients  $\kappa$  [210] were estimated for the three  $O_2$  orientations at corresponding  $z=z_{\min}$  on  $Mn_2O_3$  and  $MnOOH$  clusters. For the  $Mn_2O_3$   $\kappa$  were found to be in the range of  $10^{-1}$ - $10^{-2}$ , while for the  $MnOOH$  ( $\kappa \approx 10^{-2}$ ) for all  $O_2$  orientations. The adiabatic limit ( $\kappa \approx 1$ ) is not reached for the hydroxylated surfaces implying the non-adiabatic regime (i.e. weak orbital coupling) with the ET rate to be dependent on the oxide nature. As the  $\kappa$  is ca. 2-15 times lower for  $MnOOH$ , than  $Mn_2O_3$ , one can expect faster first ET step at  $Mn_2O_3$  due to the similar ET barriers on both oxides.

The low values of  $\kappa$  lead to the suggestion of competition between the non-adiabatic outer-sphere and inner-sphere ET involving the adsorbed  $O_2$ . Data on the  $O_2$  approach towards Mn oxide surfaces is currently unavailable in the literature. The barrier for  $O_2$  adsorption on Mn oxides can be qualitatively estimated to be the same as for Ag(100) surface, which is estimated to be ca. 0.5-0.8 eV [120], [205]. The additional barrier of 0.5-0.8 eV cannot be compensated by a ca.  $10^2$  increase in  $\kappa$ , which should take place when switching from an outer-sphere to an inner-sphere mechanism. A very weak  $O_2$  adsorption energy was computed without the account for the solvating media, but these results point to the absence of strong oxide/adsorbate interactions. So, there are no experimental or theoretical implications to consider oxygen species adsorption to be much stronger on Mn oxides than on gold or silver facets. Therefore, the outer-sphere first ET step can have a higher rate than the inner-sphere alternative.

The second ET step (3.16) can also follow either outer-sphere or inner-sphere scenario. Despite it is difficult to distinguish them, the second ET step is unlikely to be a candidate for RDS due to low barrier ca. 0.05eV [206] of proton-coupled ET to  $O_2^-$ . The latter is stronger adsorbed than the  $O_2$  [211], [212].

The results of MF-MKM, obtained by A. Bonnefont are depicted in Figure 3.7.

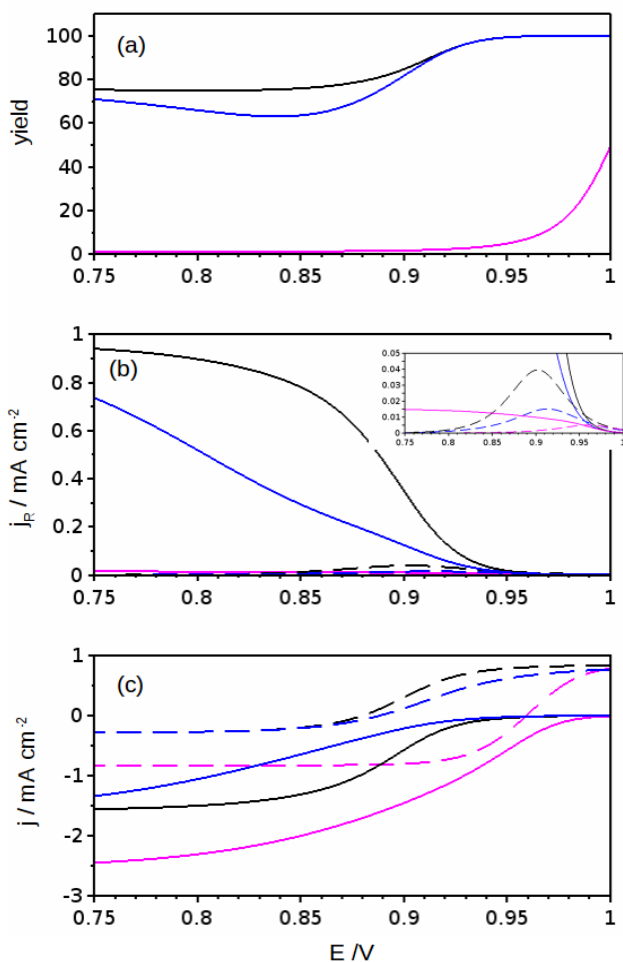


Figure 3.8 MF-MKM results of ORR and HPRR/HPOR on manganese oxides. Panel (a): Yield of soluble ORR intermediates calculated as a sum of  $\text{HO}_2^-$  and  $\text{O}_2^-$ . Panel (b), simulated  $\text{HO}_2^-$  (full lines) and  $\text{O}_2^-$  (dashed lines) escape currents. Panel (c): ORR RRDE (full lines) and HPRR (dashed lines) current-potential curves simulated for the mechanism comprising steps (3.15), (3.16):  $k_3$ , (3.17), (3.18), (3.19) Purple curves ( $k_2=10^6 \text{ cm}^3 \cdot \text{mol}^{-1} \cdot \text{s}^{-1}$ ,  $k_3=10^8 \text{ cm}^3 \cdot \text{mol}^{-1} \cdot \text{s}^{-1}$ ,  $k_5 = 40 \text{ s}^{-1}$ ,  $E^\circ_1=0.98 \text{ V}$ ), intend to reproduce the behavior of  $\text{Mn}_2\text{O}_3$ ; black curves ( $k_2=10^6 \text{ cm}^3 \cdot \text{mol}^{-1} \cdot \text{s}^{-1}$ ,  $k_3=10^8 \text{ cm}^3 \cdot \text{mol}^{-1} \cdot \text{s}^{-1}$ ,  $k_5 = 0.2 \text{ s}^{-1}$ ,  $E^\circ_1=0.90 \text{ V}$ ) and blue curves ( $k_2=10^5 \text{ cm}^3 \cdot \text{mol}^{-1} \cdot \text{s}^{-1}$ ,  $k_3=10^8 \text{ cm}^3 \cdot \text{mol}^{-1} \cdot \text{s}^{-1}$ ,  $k_5 = 0.2 \text{ s}^{-1}$ ,  $E^\circ_1=0.90 \text{ V}$ ) intend to reproduce the behavior of  $\text{MnOOH}$ . See Table S1 in [198] for other simulation parameters.

It was shown that the experimental ORR and HPRR/HPOR data cannot be reproduced by MF-MKM with materials-independent fast transfer of the first and the second electron and at least one of these steps has to be “slow” in order to simulate the behavior of MnOOH. It was possible to reproduce the experimentally observed differences in the ORR and HPRR/HPOR kinetics by assuming *ca.* 10 fold smaller  $k_2'$  for MnOOH compared to Mn<sub>2</sub>O<sub>3</sub>. The observed tenfold difference in the  $k_2'$  values (required to reproduce experimental current-potential curves) could be explained by the difference in the electronic transmission coefficients assuming the non-adiabatic reaction rate control.

### 3.4. Conclusions

A number of complementary quantum chemical approaches were applied in order to rationalize the experimentally observed differences between the most (Mn<sub>2</sub>O<sub>3</sub>) and the least active (MnOOH) oxides. The main focus was put on molecular-level factors, which determine the reaction mechanisms. It was shown that periodic DFT calculations within the conventional thermodynamic approach cannot account for the differences between Mn<sub>2</sub>O<sub>3</sub> and MnOOH, in particular with regard to the slow bond breaking in the hydrogen peroxide intermediate corroborated by the experimentally observed kinetically limited HPRR and high hydrogen peroxide yield during the ORR on MnOOH. Instead, it provided the optimized surface geometry, which was used for the calculations of activation barriers for the likely elementary steps using the cluster models (as the periodic DFT cannot be used to directly simulate charged surfaces). The faster bond-breaking was demonstrated for the hydrogen peroxide intermediate adsorbed on the surface of Mn<sub>2</sub>O<sub>3</sub> compared to that on MnOOH. It is explained by adsorbate-adsorbate interactions at the Mn<sub>2</sub>O<sub>3</sub> surface, which decrease the activation barrier for bond-breaking in the HO<sub>2</sub><sup>-</sup><sub>ads</sub> intermediate. The cluster calculations also suggest that a direct 4e<sup>-</sup> ORR is unlikely for Mn<sub>2</sub>O<sub>3</sub>. According to MF-MKM, the experimental differences between Mn<sub>2</sub>O<sub>3</sub> and MnOOH cannot be reproduced considering material-independent kinetics for the outer-sphere transfer of the first and the second electrons, which is corroborated by the 1 order of magnitude difference

in estimated electron transmission coefficients for  $\text{Mn}_2\text{O}_3$  and  $\text{MnOOH}$ . The estimated activation barriers for the first outer-sphere ET step supports its possibility on the Mn oxides in alkaline media.

The computational results reported in this study involve a large number of approximations, which should be taken into account critically when comparing the calculated and experimental trends. First, the solvent-solute and the solvent-electrode interactions are not taken into account either in periodic DFT or in cluster calculations, as these would increase the system size to a hardly treatable value. The focus of the computational study is thus placed exclusively at the electrode/reactant interactions. The second major approximation is related to the application of the cluster approach to describe the orbital overlap effect on the ET rate for the two oxides, as this approach does not allow to reproduce the difference in the oxides' electronic structures quantitatively. In this case, as well as in the case of the bond-breaking step, one can outline mainly geometrical factors, which affect the differences in the  $\text{MnOOH}$  and  $\text{Mn}_2\text{O}_3$  activities. Another approximation consists in the simplification of the bond-breaking mechanism, which could involve much more complex rearrangements in the reaction layer with the participation of  $\text{H}_2\text{O}$  and  $\text{OH}^-$  species. Finally, the reaction steps in the formal kinetic modeling do not directly correspond to the elementary steps, which are addressed in the computational study. This does not allow to directly compare the values of the rate constants resulting from formal kinetic modeling and from quantum chemical calculations, but rather rely on the outlined general trends in the differences of oxides' activity. Due to the vast number of approximations, the model form uncertainties arising from them should be quantified in order to determine, whether the current detailing enables the predictive analysis of reaction rates on oxides within the proposed reaction mechanism.

## **Chapter 4. Assessment of ORR Mechanism Complexity for Decoupling the Roles of Carbon and Metal Oxides on $\text{La}_{1-x}\text{Sr}_x\text{O}_{3-\delta}$ / C Composite Materials Within the MF-MKM Approach.**

The results presented in this chapter are based on the following publication. [T. J. Mefford, A. A. Kurilovich, J. Saunders, W. G. Hardin, A. M. Abakumov, R. P. Forslund, A. Bonnefont, S. Dai, K. P. Johnston, K. J. Stevenson. Decoupling the roles of carbon and metal oxides on the electrocatalytic reduction of oxygen on  $\text{La}_{1-x}\text{Sr}_x\text{CoO}_{3-\delta}$  perovskite composite electrodes. *Phys. Chem. Chem. Phys.*, 2019;21(6):3327-38.]. Given the unavoidable approximations at the microscopic level required to qualitatively explain the catalytic activity difference between the  $\text{Mn}_2\text{O}_3$  and  $\text{MnOOH}$ , the first step to understanding the role of carbon (particularly with respect to N-doping) should be carried out on the macroscopic level by MF-MKM. It can be started using the models which were successfully applied to the LCO/Sibunit carbon[68]. One can further extend them to explain the self-consistent experimental dataset with the series of TMO materials ( $\text{La}_{1-x}\text{Sr}_x\text{CoO}_{3-\delta}$ ) supported by N-doped and non-doped carbon components.

The aim of this chapter is to elucidate the individual contributions of the carbon support and the perovskite oxide series  $\text{La}_{1-x}\text{Sr}_x\text{CoO}_{3-\delta}$  (LSCO(1-x)x) in the ORR by MF-MKM in order to understand the required complexity of the overall ORR mechanistic pathway, which should be capable to explain the synergistic effects in the carbon-supported perovskite composite systems. The author's main contribution was the MF-MKM for the ORR and HPRR/HPOR on LSCO/Carbon composite materials.

### **4.1. Materials and methods**

#### *4.1.1. Chemicals*

All chemicals were used as received. Anhydrous ethanol and 5 wt% Nafion solution in lower alcohols were purchased from Sigma-Aldrich. Lanthanum (III) nitrate hexahydrate (99.999%), strontium (II) nitrate hexahydrate (99.9%), cobalt (II) nitrate hexahydrate (99.9%), tetrapropylammonium bromide (98%), tetramethylammonium hydroxide pentahydrate (99%), 2-propanol, and potassium hydroxide were obtained from Fisher

Scientific. Absolute ethanol (200 proof) was obtained from Aaper alcohol. Oxygen (99.999%) gas was obtained from Praxair. Vulcan carbon XC-72 (VC) was obtained from Cabot Corporation, and the nitrogen-doped carbon (NC) was prepared as reported elsewhere [213]. The LSCO series was synthesized by T. J. Mefford and W. G. Hardin according to the methods described previously [214]–[217].

#### *4.1.2. Electrochemical characterization*

The electrochemical characterization was performed by T. J. Mefford. All  $\text{La}_{1-x}\text{Sr}_x\text{CoO}_{3-\delta}$  (LSCO(1-x)x) nanopowders were loaded onto carbon through ball milling with a Wig-L-Bug ball mill. For rotating disk electrode (RDE) and for the rotating ring-disk electrode (RRDE) measurements the LSCO nanopowders were loaded at a mass loading of ~30 wt% onto either VC or NC. LSCO/carbon mixtures were dispersed in ethanol containing 0.05 wt% Na-substituted Nafion at a ratio of 1 mg mL<sup>-1</sup> and sonicated for 45 min. This solution was spincast onto a glassy carbon rotating disk electrode (0.196 cm<sup>2</sup>, Pine Instruments) and for the rotating ring-disk electrode (Glassy Carbon Disk: 0.2472 cm<sup>2</sup><sub>geom</sub>; Pt ring: 0.1859 cm<sup>2</sup>, Pine Instruments) at a total mass loading of 51.0 μg cm<sup>-2</sup><sub>geom</sub> (LSCO loading: 15.3 μg cm<sup>-2</sup><sub>geom</sub>). The electrodes were cleaned prior to spincasting by sonication in a 1:1 de-ionized water:ethanol solution. The electrodes were then polished using 50 nm alumina powder, sonicated in a fresh deionized water:ethanol solution, and dried under a scintillation vial in ambient air.

Electrochemical testing was performed on a CH Instruments CHI832a potentiostat or a Metrohm Autolab PGSTAT302N potentiostat, both equipped with high-speed rotators from Pine Instruments. Both RDE and RRDE ORR tests were performed at room temperature in O<sub>2</sub> saturated 0.1M KOH (measured pH ≈ 12.6). The current interrupt and positive feedback methods were used to determine electrolyte resistance (50 Ω) and all data was *iR* compensated after testing. Each measurement was performed in a standard three-electrode cell using a Hg/HgO (1M KOH) reference electrode, a Pt wire counter electrode, and a film of catalyst ink on the glassy carbon working electrode. All ORR testing was performed on a new electrode that had not undergone the previous testing. Cyclic

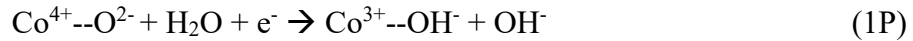
voltammetry was performed from +1.0 to +0.4 V at 5 mV s<sup>-1</sup> at rotation rates of  $\omega = 400, 522, 712, 1024, \text{ and } 1600$  rpm.

For the peroxide studies, the same methodology was used with an electrolyte consisting of 1.2 mM H<sub>2</sub>O<sub>2</sub> in Ar-saturated 0.1M KOH. Cyclic voltammetry was performed by scanning either +/- 500 mV from the measured open circuit potential at a scan rate of 5 mV s<sup>-1</sup> and an electrode rotation rate of 1600 rpm. The measurements were carried out in triplicate using a freshly prepared electrode for each measurement. Electrodes subjected to scans in the anodic potential direction from OCV were not tested in the cathodic and vice versa. The data presented is an average of the triplicate measurements. All potentials are reported versus the reversible hydrogen electrode (RHE), which was measured as  $E_{\text{RHE}} = E_{\text{Hg/HgO}} + 0.8456 \text{ V}$  through the reduction of hydrogen in 1 atm H<sub>2</sub> saturated 0.1M KOH.

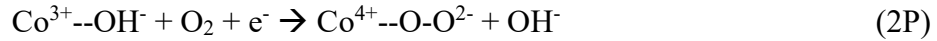
#### 4.2. Theoretical basis

The suggested ORR mechanisms for perovskites consist of 5 reaction steps:

- 1) Surface Co<sup>4+</sup>/Co<sup>3+</sup> redox transition.



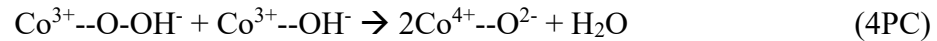
- 2) Oxygen adsorption/ desorption on/from the Co<sup>3+</sup> active sites, combined with the first electron transfer step.



- 3) The reduction of the adsorbed oxygen into the HO<sub>2</sub><sup>-</sup> / oxidation of HO<sub>2</sub><sup>-</sup> to the oxygen.



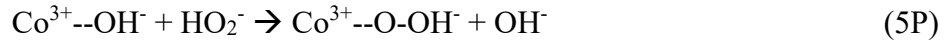
- 4) Chemical decomposition of the adsorbed HO<sub>2</sub><sup>-</sup>. (reaction mechanism with 4PC step)



Electrochemical reduction of HO<sub>2</sub><sup>-</sup> to OH<sup>-</sup> / oxidation of OH<sup>-</sup> to HO<sub>2</sub><sup>-</sup>. (reaction mechanism with 4PE step)



5) The adsorption/desorption of  $\text{HO}_2^-$  on/from the  $\text{Co}^{3+}$  surface site.

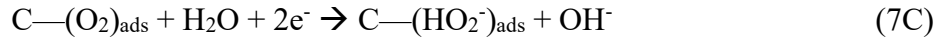


The ORR and HPRR/HPOR reactions on VC and NC carbons were simulated using the following effective mechanism:

6) Oxygen adsorption/ desorption on/from the carbon active sites



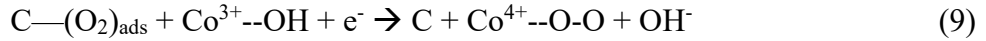
7) The reduction of the adsorbed oxygen into the  $\text{HO}_2^-$ /oxidation of  $\text{HO}_2^-$  to the oxygen.



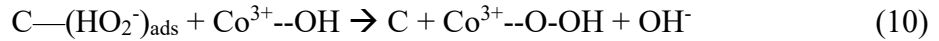
8)  $\text{HO}_2^-$  adsorption/desorption on/from the carbon active site.



9) Effective reaction step for the oxygen spillover between the N-doped active sites and  $\text{Co}^{3+}$  cations (also modeled on VC for consistency)



10) Effective reaction step for the  $\text{HO}_2^-$  spillover between the N-doped active sites and  $\text{Co}^{3+}$  cations



The electrode surface is considered to be flat with the perfectly intermixed carbon and perovskite active sites which are equally accessible by the  $\text{O}_2$  and  $\text{HO}_2^-$  species, so the  $\text{O}_2$  and  $\text{HO}_2^-$  concentration is considered the same in the vicinity of perovskite and carbon active sites. The diffusion profile was assumed to be linear for the  $\text{O}_2$  and  $\text{HO}_2^-$  species in the solution. The diffusion in the bulk of the electrode was neglected because of the low experimental catalyst loading. Diffusivities of  $\text{O}_2$  and  $\text{HO}_2^-$ , kinematic viscosity, and oxygen solubility were taken from the literature data. [39] LCO and VC surface active sites densities were obtained by renormalization of the estimates for LCO and Sibunit-152 carbon from works by BET surface areas and loadings ratios for the materials synthesized in this and abovementioned works. [68], [73]

The proposed reaction mechanisms are used to construct a system of ordinary differential equations, which describes the reaction kinetics together with the mass transport of O<sub>2</sub> and HO<sub>2</sub><sup>-</sup> to the vicinity of the electrode. It is solved numerically in the steady-state approximation which can be directly linked with the experiments due to the slow scan rates in the performed experiments. The microkinetic model follows the assumption of Langmuir isotherms for the adsorption/desorption steps and Butler-Volmer electrochemical kinetics for all electron transfer steps. The rate constants for the reaction mechanisms were adjusted until the model qualitatively reproduced experimental findings for ORR RDE and HPRR/HPOR

Forward and backward rate constants ratio of steps 1) (6C), (7C), (8C); 2) (2P), (3P), (5P); 3) (2P), (3P), (5P), (9); 4) (2P), (3P), (5P), (10) were simultaneously adjusted and fixed in order to reproduce pH-corrected equilibrium potential E<sub>HO<sub>2</sub><sup>-</sup>/O<sub>2</sub></sub> = 0.74 V vs. RHE at pH = 13. The same procedure was applied to adjust the rate constants ratio for the steps (4PE), (4PC) to reproduce the pH corrected equilibrium potential E<sub>HO<sub>2</sub><sup>-</sup>/OH<sup>-</sup></sub> = 1.74 vs. RHE at pH = 13. It was consistently obtained that the (4PE) and (4PC) steps are irreversible at the potential range at which the ORR and HPRR/HPOR experiments were carried out.

$$r_{1P} = k_1 \theta_{O_2 P} \exp\left(-\frac{\alpha_1 F(E - E_1^0)}{RT}\right) - k_{-1}(1 - \theta_{O_2 P} - \theta_{O_2 P} - \theta_{HO_2 P}) \exp\left(\frac{(1 - \alpha_1)F(E - E_1^0)}{RT}\right) \quad (4.1)$$

$$r_{2P} = k_2 c_{O_2} (1 - \theta_{O_2 P} - \theta_{O_2 P} - \theta_{HO_2 P}) \exp\left(-\frac{\alpha_2 FE}{RT}\right) - k_{-2} \theta_{O_2 P} \exp\left(\frac{(1 - \alpha_2)FE}{RT}\right) \quad (4.2)$$

$$r_{3P} = k_3 \theta_{O_2 P} \exp\left(-\frac{\alpha_3 FE}{RT}\right) - k_{-3} \theta_{HO_2 P} \exp\left(\frac{(1 - \alpha_3)FE}{RT}\right) \quad (4.3)$$

$$r_{4PC} = k_4 (1 - \theta_{O_2 P} - \theta_{O_2 P} - \theta_{HO_2 P}) \theta_{HO_2 P} - k_{-4} \theta_{O_2 P}^2 \quad (4.4)$$

$$r_{4PE} = k_4 \theta_{HO_2 P} \exp\left(-\frac{\alpha_4 FE}{RT}\right) - k_{-4} \theta_{O_2 P} \exp\left(\frac{(1 - \alpha_4)FE}{RT}\right) \quad (4.5)$$

$$r_{5P} = k_5 c_{HO_2^-} (1 - \theta_{O_2 P} - \theta_{O_2 P} - \theta_{HO_2 P}) - k_{-5} \theta_{HO_2 P} \quad (4.6)$$

$$r_{6C,N} = k_{6C,N}c_{O_2}(1 - \theta_{O_2 C,N} - \theta_{HO_2^- C,N}) - k_{-6C,N}\theta_{O_2 C,N} \quad (4.7)$$

$$r_{7C,N} = k_{7C,N}\theta_{O_2 C,N} \exp\left(-\frac{\alpha_7 FE}{RT}\right) - k_{-7C,N}\theta_{HO_2^- C,N} \exp\left(\frac{(1 - \alpha_7) FE}{RT}\right) \quad (4.8)$$

$$r_{8C,N} = k_{8C,N}\theta_{HO_2^- C,N} - k_{-8C,N}c_{HO_2^- C,N}(1 - \theta_{O_2 C,N} - \theta_{HO_2^- C,N}) \quad (4.9)$$

$$r_{9N} = k_9\theta_{O_2 N}(1 - \theta_{O P} - \theta_{O_2 P} - \theta_{HO_2 P}) \exp\left(-\frac{\alpha_9 FE}{RT}\right) - k_{-9}(1 - \theta_{O_2 N} - \theta_{HO_2^- N}) \exp\left(\frac{(1 - \alpha_9) FE}{RT}\right) \quad (4.10)$$

$$r_{10N} = k_{10}\theta_{HO_2^- N}(1 - \theta_{O P} - \theta_{O_2 P} - \theta_{HO_2 P}) - k_{-10}\theta_{HO_2 P}(1 - \theta_{O_2 N} - \theta_{HO_2^- N}) \quad (4.11)$$

The ORR current potential curves were simulated under the stationary conditions:

$$\frac{d\theta_{O_2 N}}{dt} = 0 = r_{6N} - r_{7N} - \frac{\Gamma_P}{\Gamma_N} r_{9N} \quad (4.12)$$

$$\frac{d\theta_{O_2 C}}{dt} = 0 = r_{6C} - r_{7C} \quad (4.13)$$

$$\frac{d\theta_{HO_2^- N}}{dt} = 0 = r_{7N} - r_{8N} - \frac{\Gamma_P}{\Gamma_N} r_{10N} \quad (4.14)$$

$$\frac{d\theta_{HO_2^- C}}{dt} = 0 = r_{7C} - r_{8C} \quad (4.15)$$

When the pathway follows (4PC)

$$\frac{d\theta_{O P}}{dt} = 0 = 2r_{4PC} - r_{1P} \quad (4.16)$$

When the pathway follows (4PE)

$$\frac{d\theta_{O P}}{dt} = 0 = r_{4PE} - r_{1P} \quad (4.17)$$

$$\frac{d\theta_{O_2 P}}{dt} = 0 = r_{2P} - r_{3P} + r_{9N} \quad (4.18)$$

$$\frac{d\theta_{HO_2 P}}{dt} = 0 = r_{3P} - r_{4P} + r_{5P} + r_{10N} \quad (4.19)$$

Given the linear concentration profile in the solution, one can write down the mass-balance equations for  $O_2$  and  $HO_2^-$ :

$$D_{O_2} \frac{dc_{O_2}}{dt} \approx D_{O_2} \frac{c_{O_2}^{bulk} - c_{O_2}}{\delta_{O_2}} = \Gamma_C r_{6C} + \Gamma_N r_{6N} + \Gamma_P r_{2P} \quad (4.20)$$

$$D_{HO_2^-} \frac{dc_{HO_2^-}}{dt} \approx D_{HO_2^-} \frac{c_{HO_2^-}^{bulk} - c_{HO_2^-}}{\delta_{HO_2^-}} = -\Gamma_C r_{8C} - \Gamma_N r_{8N} + \Gamma_P r_{5P} \quad (4.21)$$

Here,  $D_{O_2}$ ,  $D_{HO_2^-}$  are the  $O_2$  and  $HO_2^-$  diffusion coefficients,  $c_{O_2}^{bulk}$ ,  $c_{HO_2^-}^{bulk}$  are the  $O_2$  and  $HO_2^-$  concentrations in the solution bulk,  $c_{O_2}$ ,  $c_{HO_2^-}$  are  $O_2$  and  $HO_2^-$  concentrations in the vicinity of the electrode surface,  $\delta_{O_2}$ ,  $\delta_{HO_2^-}$  are the  $O_2$  and  $HO_2^-$  diffusion layer thickness,  $\theta_{O_2 C}$ ,  $\theta_{HO_2^- C}$  are the  $O_2$  and  $HO_2^-$  surface coverages on carbon active sites,  $\theta_{O_2 N}$ ,  $\theta_{HO_2^- N}$  are the  $O_2$  and  $HO_2^-$  surface coverages on nitrogen-doped carbon active sites, and  $\theta_{O_2 P}$ ,  $\theta_{HO_2 P}$ ,  $\theta_{O P}$  are the  $O_2$ ,  $HO_2$ , and  $O$  surface coverages on perovskite. The diffusion layer thicknesses are estimated from the analytical solution for the RDE experiment using the electrode rotation rate  $\omega$  and kinematic viscosity  $\nu$  [58], [83]:

$$\delta_{O_2} = 1.61 D_{O_2}^{1/3} \omega^{-1/2} \nu^{1/6} \quad (4.22)$$

$$\delta_{HO_2^-} = 1.61 D_{HO_2^-}^{1/3} \omega^{-1/2} \nu^{1/6} \quad (4.23)$$

$\Gamma_C$ ,  $\Gamma_N$ ,  $\Gamma_P$  are C, N-doped, and perovskite surface active sites densities for ORR and HPRR/HPOR, which were calculated from the estimations provided in the work using the renormalization by the catalyst loading and BET surface areas [68].

ORR and HPRR/HPOR currents were calculated as:

$$I_{ORR, HPRR/HPOR}^{4PC} = -2F\Gamma_C r_{7C} - 2F\Gamma_N r_{7N} - F\Gamma_P (r_{1P} + r_{2P} + r_{3P} + r_9) \quad (4.24)$$

$$I_{ORR, HPRR/HPOR}^{4PE} = -2F\Gamma_C r_{7C} - 2F\Gamma_N r_{7N} - F\Gamma_P (r_{1P} + r_{2P} + r_{3P} + r_{4PE} + r_9) \quad (4.25)$$

Table 4.1 Adjusted model parameters

Parameter	VC (4PC/4PE)	NC (4PC/4PE)	LCO/VC (4PC/4PE)	LCO/NC (4PC/4PE)	LSCO64/VC (4PC)	LSCO64/NC (4PC)
$k_1, s^{-1}$	-/-	-/-	$9.6 \times 10^{-1}/5.6$ $\times 10^{-1}$	$9.6 \times 10^{-1}/5.6$ $\times 10^{-1}$	$9.6 \times 10^{-1}$	$9.6 \times 10^{-1}$
$k_{-1}, s^{-1}$	-/-	-/-	$9.6 \times 10^{-1}/5.6$ $\times 10^{-1}$	$9.6 \times 10^{-1}/5.6$ $\times 10^{-1}$	$9.6 \times 10^{-1}$	$9.6 \times 10^{-1}$
$k_2, cm^3 mol^{-1}$ $s^{-1}$	-/-	-/-	$1.3 \times 10^{10}/1.6$ $\times 10^{11}$	$1.3 \times 10^{10}/1.6$ $\times 10^{11}$	$1.0 \times 10^{16}$	$1 \times 10^{16}$
$k_2, s^{-1}$	-/-	-/-	$2.8 \times 10^{-9}/3.5$ $\times 10^{-8}$	$2.8 \times 10^{-9}/3.5$ $\times 10^{-8}$	$2.2 \times 10^{-3}$	$2.3 \times 10^{-3}$
$k_3, s^{-1}$	-/-	-/-	$1.3 \times 10^{10}/2.9$ $\times 10^{11}$	$1.3 \times 10^{10}/2.9$ $\times 10^{11}$	$1.2 \times 10^8$	$1.2 \times 10^8$
$k_{3C}, s^{-1}$	-/-	-/-	$1.4 \times 10^{-6}/3.5$ $\times 10^{-4}$	$1.4 \times 10^{-6}/3.5$ $\times 10^{-4}$	$1.4 \times 10^{-7}$	$1.4 \times 10^{-7}$
$k_4, s^{-1}$	-/-	-/-	$2.5 \times 10^1/1.4$ $\times 10^{10}$	$2.5 \times 10^1/1.4$ $\times 10^{10}$	$3.0 \times 10^1$	$3.0 \times 10^1$
$k_{4C}, s^{-1}$	-/-	-/-	0/0	0/0	0	0
$k_5, cm^3 mol^{-1}$ $s^{-1}$	-/-	-/-	$4 \times 10^8/4 \times 10^6$	$4 \times 10^8/4 \times 10^6$	$4 \times 10^8$	$4 \times 10^8$
$k_{5C}, s^{-1}$	-/-	-/-	$1 \times 10^3/1 \times 10^1$	$1 \times 10^3/1 \times 10^1$	$1 \times 10^3$	$1 \times 10^3$
$k_{6C}, cm^3 mol^{-1}$ $s^{-1}$	$1.5 \times 10^8/1.5$ $\times 10^8$	$1.5 \times 10^8$	$1.5 \times 10^8$			
$k_{6C}, cm s^{-1}$	$1.6 \times 10^3/1.6$ $\times 10^3$	$1.6 \times 10^3$	$1.6 \times 10^3$			
$k_{7C}, s^{-1}$	$5.5 \times 10^9/5.5$ $\times 10^9$	$5.5 \times 10^9$	$5.5 \times 10^9$			
$k_{7C}, s^{-1}$	$1.6 \times 10^{-1}/1.6$ $\times 10^{-1}$	$1.6 \times 10^{-1}$	$1.6 \times 10^{-1}$			
$k_{8C}, s^{-1}$	$1.8 \times 10^3/1.8$ $\times 10^3$	$1.8 \times 10^3$	$1.8 \times 10^3$			

$k_{8C}, \text{cm}^3 \text{mol}^{-1} \text{s}^{-1}$	$2.0 \times 10^3/2.0 \times 10^3$	$2.0 \times 10^3/2.0 \times 10^3$	$2.0 \times 10^3/2.0 \times 10^3$	$2.0 \times 10^3/2.0 \times 10^3$	$2.0 \times 10^3$	$2.0 \times 10^3$
$k_{6NC}, \text{cm}^3 \text{mol}^{-1} \text{s}^{-1}$	-/-	$1.5 \times 10^8/1.5 \times 10^8$	-/-	$1.5 \times 10^8/1.5 \times 10^8$	-	$1.5 \times 10^8$
$k_{6N}, \text{cm}^3 \text{s}^{-1}$	-/-	$1.6 \times 10^3/1.6 \times 10^3$	-/-	$1.6 \times 10^3/1.6 \times 10^3$	-	$1.6 \times 10^3$
$k_{7N}, \text{s}^{-1}$	-/-	$3.7 \times 10^8/3.7 \times 10^8$	-/-	$3.7 \times 10^8/3.7 \times 10^8$	-	$3.7 \times 10^8$
$k_{7N}, \text{s}^{-1}$	-/-	$6.9 \times 10^{-3}/6.9 \times 10^{-3}$	-/-	$6.9 \times 10^{-3}/6.9 \times 10^{-3}$	-	$6.9 \times 10^{-3}$
$k_{8N}, \text{s}^{-1}$	-/-	$4.2 \times 10^3/4.2 \times 10^3$	-/-	$4.2 \times 10^3/4.2 \times 10^3$	-	$4.2 \times 10^3$
$k_{8N}, \text{cm}^3 \text{mol}^{-1} \text{s}^{-1}$	-/-	$4.6 \times 10^3/4.6 \times 10^3$	-/-	$4.6 \times 10^3/4.6 \times 10^3$	-	$4.6 \times 10^3$
$k_9, \text{s}^{-1}$	-/-	-/-	$8.8 \times 10^{11}/-$	$1.7 \times 10^{12}/8.8 \times 10^{11}$	-	$3.5 \times 10^{12}$
$k_9, \text{s}^{-1}$	-/-	-/-	$1.8 \times 10^{-2}/-$	$3.6 \times 10^{-2}/2.3 \times 10^{-1}$	-	$7.2 \times 10^{-2}$
$k_{10}, \text{s}^{-1}$	-/-	-/-	-/-	$1 \times 10^5/1 \times 10^4$	-	-
$k_{10}, \text{s}^{-1}$	-/-	-/-	-/-	$2.8 \times 10^{-1}/2.8 \times 10^{-2}$	-	-
$E_1^0 \text{ V vs. RHE}$	-/-	-/-	0.933	0.933	1.053	1.053
$\alpha_1$	-/-	-/-	0.5/0.5	0.5/0.5	0.5	0.5
$\alpha_2$	-/-	-/-	0.5/0.5	0.5/0.5	0.8	0.8
$\alpha_3$	-/-	-/-	0.5/0.5	0.5/0.5	0.5	0.5
$\alpha_4$	-/-	-/-	-/0.5	-/0.5	-	-
$\alpha_{7C}$	0.8/0.8	0.8/0.8	0.8/0.8	0.8/0.8	0.8	0.8
$\alpha_{7NC}$	-/-	0.5	-/-	0.5	-	0.5
$\alpha_9$	-/-	-/-	-/-	0.8/0.8	-	0.8

$\Gamma_C$	$1.9 \times 10^{-8}/1.9 \times 10^{-8}$	$1.9 \times 10^{-8}/1.9 \times 10^{-8}$	$1.9 \times 10^{-8}/1.9 \times 10^{-8}$	$1.9 \times 10^{-8}/1.9 \times 10^{-8}$	$1.9 \times 10^{-8}$	$1.9 \times 10^{-8}$
$\Gamma_{NC}$	-/-	$3.9 \times 10^{-10}/3.9 \times 10^{-10}$	-/-	$3.9 \times 10^{-10}/3.9 \times 10^{-10}$	-	$3.9 \times 10^{-10}$
$\Gamma_{LSCO}$	-/-	-/-	$6.1 \times 10^{-10}/6.1 \times 10^{-10}$	$6.1 \times 10^{-10}/6.1 \times 10^{-10}$	$6.1 \times 10^{-10}$	$6.1 \times 10^{-10}$
$v, \text{cm}^2 \text{s}^{-1}$	$1.0 \times 10^{-2}$	$1.0 \times 10^{-2}$	$1.0 \times 10^{-2}$	$1.0 \times 10^{-2}$	$1.0 \times 10^{-2}$	$1.0 \times 10^{-2}$
$c_{O_2}^*$	$1.2 \times 10^{-6}$	$1.2 \times 10^{-6}$	$1.2 \times 10^{-6}$	$1.2 \times 10^{-6}$	$1.2 \times 10^{-6}$	$1.2 \times 10^{-6}$
$c_{HO_2}^*$	$1.2 \times 10^{-6}$	$1.2 \times 10^{-6}$	$1.2 \times 10^{-6}$	$1.2 \times 10^{-6}$	$1.2 \times 10^{-6}$	$1.2 \times 10^{-6}$
$D_{O_2}$	$1.9 \times 10^{-5}$	$1.9 \times 10^{-5}$	$1.9 \times 10^{-5}$	$1.9 \times 10^{-5}$	$1.9 \times 10^{-5}$	$1.9 \times 10^{-5}$
$D_{HO_2}$	$0.8 \times 10^{-5}$	$0.8 \times 10^{-5}$	$0.8 \times 10^{-5}$	$0.8 \times 10^{-5}$	$0.8 \times 10^{-5}$	$0.8 \times 10^{-5}$

### 4.3. Results and discussion

The physical properties of a series of Sr substituted lanthanum cobalt oxides,  $\text{La}_{1-x}\text{Sr}_x\text{CoO}_{3-\delta}$ , where, for instance, LSCO28 refers to  $\text{La}_{0.2}\text{Sr}_{0.8}\text{CoO}_{3-\delta}$ , have been described by J. T. Mefford et. al. [214] The surface properties of the series were elucidated by collaborators using the O1s X-ray photoelectron spectroscopy (XPS) and HAADF and ABF-STEM imaging with atomic resolution EDX [218].

In order to decouple the activities of the LSCO members from the contributions of the carbon to the ORR, the perovskite catalysts were supported at 30 wt% on two different carbons, Vulcan carbon XC-72 (VC) and a 2 at. % nitrogen-doped mesoporous carbon (NC). Following results are crucial for ORR mechanism suggestion and modeling:

BET surface areas were relatively consistent across the entire series, ranging from 3.1 to  $4.5 \text{ m}^2 \text{ g}^{-1}$ . [214] Chemical titration measurements of the oxygen stoichiometry across the series show a trend of increasing oxygen deficiency and increasing the cobalt oxidation state with increasing  $\text{Sr}^{2+}$  substitution for  $\text{La}^{3+}$ . In addition, it was shown through XPS that surface hydroxylation increases substantially with Sr substitution, partially as a function of cobalt oxidation state, and from the presence of surface oxygen vacancies which act as



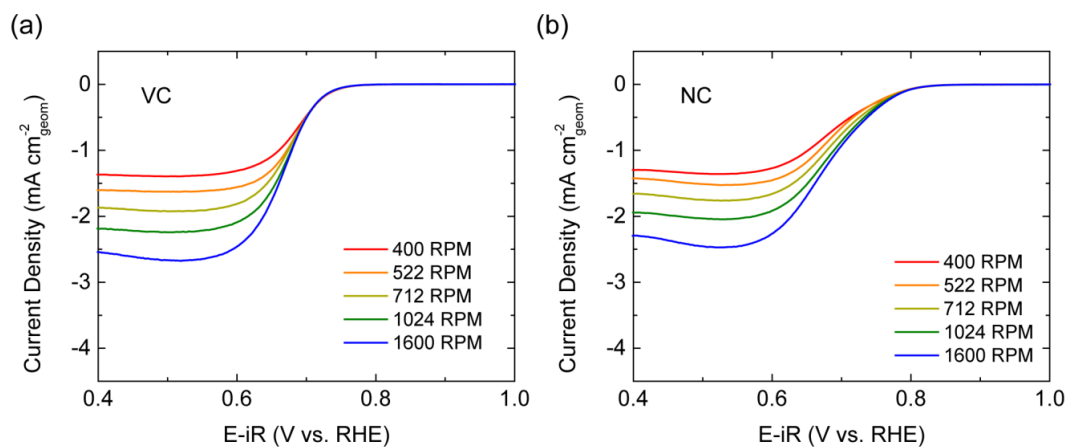


Figure 4.2 RDE analysis of (a) Vulcan carbon and (b) nitrogen-doped mesoporous carbon at a scan rate of  $5 \text{ mV s}^{-1}$  in the negative potential direction in  $\text{O}_2$  saturated  $0.1 \text{ M KOH}$ . Electrode mass loadings were  $35.7 \mu\text{g cm}^{-2}_{\text{geom}}$ . All polarization curves have been  $iR$  corrected.

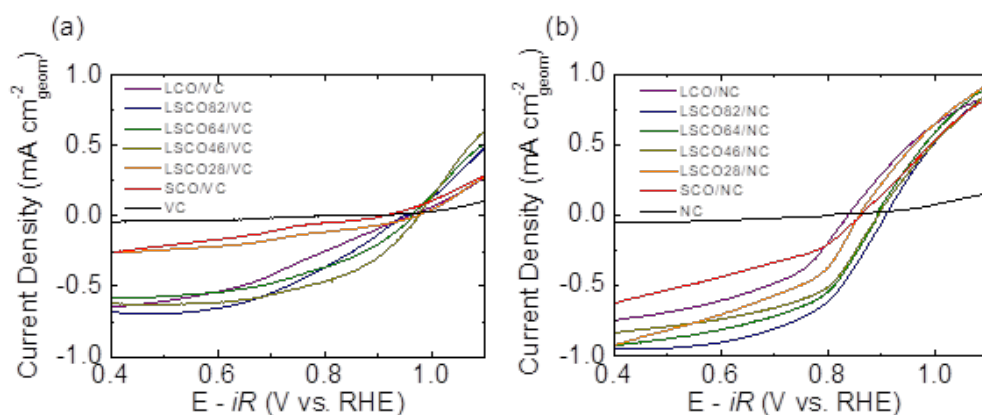


Figure 4.3 RDE analysis of HPOR/HPRR on LSCO perovskite composite electrocatalysts supported on (a) Vulcan carbon and on (b) Nitrogen-doped mesoporous carbon at a scan rate of  $5 \text{ mV s}^{-1}$  and rotation rate of  $1600 \text{ rpm}$  in  $0.1 \text{ M KOH}$  with an addition of  $1.2 \text{ mM H}_2\text{O}_2$ . Electrode mass loadings were  $35.7 \mu\text{g cm}^{-2}_{\text{geom}}$  for carbon and  $15.7 \mu\text{g cm}^{-2}_{\text{geom}}$  for oxide. All polarization curves have been  $iR$ -corrected.

To gain further insight into the ORR reaction mechanism the reactivity of the hydrogen peroxide reduction (HPRR) and oxidation (HPOR) reactions is investigated on the LSCO/carbon composites through rotating-disk electrochemistry, as shown in Figure 4.3. The represented results are the average of triplicate measurements of capacitance averaged forward and backward scans. The obtained voltammograms generally consist of three electrochemical reactions: (1)  $\text{HO}_2^-$  reduction to  $\text{OH}^-$  (HPRR,  $E_1^0 = 1.74$  V vs. RHE @ pH = 13); (2)  $\text{O}_2$  reduction to  $\text{HO}_2^-$  /  $\text{HO}_2^-$  oxidation to  $\text{O}_2$  (HPOR,  $E_2^0 = 0.74$  V vs. RHE @ pH = 13); (3) Full  $4e^-$   $\text{O}_2$  reduction to  $\text{OH}^-$  (ORR,  $E_3^0 = 1.23$  V vs. RHE @ pH = 13). The ORR (reaction (3)) may occur at potentials higher than 0.77 V vs. RHE due to  $\text{O}_2$  production by the reverse of reaction (2). Both the VC and NC show negligible activity towards the HPRR, supporting the  $2e^-$  reduction of  $\text{O}_2$  to  $\text{HO}_2^-$  on carbons. At the more positive potentials where HPOR may occur, the currents on pure carbons are still much lower than those of the LSCO/carbon composite electrodes. This behavior may be observed only if the reaction (2) is sluggish and has a slow rate even at the overpotentials higher than 0.8 V. The mixed current potential (open circuit potential) is shifted towards lower overpotential by  $\sim 50$  mV for LSCO/NC versus LSCO/VC. The currents on the LSCO/NC composites also tend to increase compared to those of LSCO/VC. This effect can be explained by the nonequivalent enhancement of the HPOR and HPRR by the NC support leading to the simultaneous increase in currents and shift of the onset potential. While both VC and NC are inactive for HPRR/HPOR, this demonstrates the effect of reaction coupling between the perovskites and the carbon support. In order to better understand this behavior, one needs to deconvolute the contributions of reactions (1) and (2) through the aid of a microkinetic model described below. The simulation of the ORR mechanism requires the experimental data for the materials which are stable within the experimental setup. Otherwise, the degradation processes should be directly taken into consideration by the model. For these reasons, the data for the LCO and LSCO64 perovskite materials are used in simulations. LCO is shown to be stable at the potentials above 0.4 V vs RHE, where ORR and HPRR/HPOR are studied [60], [81]. Despite LSCO64 has lower bulk stability than LCO [219], which is correlated with the more negative free energy change for the

lattice oxygen vacancy formation [214], rather low O vacancy concentration in LSCO64 [214], [220] and the use of fresh electrodes at each ORR and HPRR/HPOR RDE experiments suggest that the catalytic degradation process (if present) is slow during the experiments and does not notably change the results.

The synergistic mechanistic pathways are considered involving the spillover of oxygen-containing intermediates (either  $O_2^-$  or  $HO_2^-$ ) from the carbon to the oxide in agreement with a number of recent studies on cobalt-based perovskites. [68], [71], [73], [82], [216], [221]–[225]. The reactions are simulated using a MF-MKM and compared to the experimentally observed catalytic activity trends towards the ORR and HPRR/HPOR for LSCO perovskites and carbons in order to ascertain the dominant pathway [68], [73].

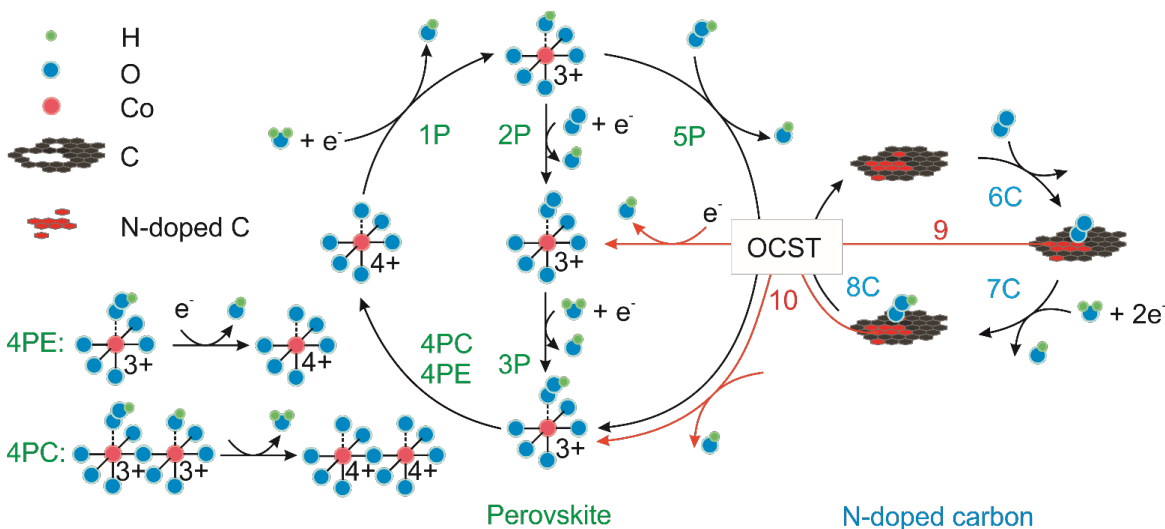


Figure 4.4 Proposed mechanism of oxygen reduction on LSCO/Carbon composite electrodes. On the LSCO perovskite catalysts (where P refers to a reaction on the perovskite surface) the steps are: (1P)  $Co^{3+/4+}$  surface redox step associated with  $-O$  and  $-OH$  adsorbates; (2P) oxygen adsorption on the  $Co^{3+}$  active sites combined with the first electron transfer step; (3P) reduction of the adsorbed oxygen to the  $HO_2^-$ ; (4PE) electrochemical reduction of the adsorbed  $HO_2^-$  to  $OH^-$  or (4PC)  $HO_2^-$  chemical decomposition; (5P) alternative pathway considering adsorption of  $HO_2^-$  on the perovskite surface rather than  $O_2$ . On the carbon (where C refers to a reaction on the carbon surface) the hypothesized steps are: (6C)  $O_2$  adsorption; (7C) effective step of  $O_2$  reduction to  $HO_2^-$ , note that 6C and

7C yield the overall  $2 e^-$  reduction of  $O_2$  to  $HO_2^-$ ; (8C)  $HO_2^-$  desorption step. Oxygen-containing species transfer steps (OCST) consist of (9)  $O_2$  spillover between the nitrogen-doped carbon active sites and perovskite active sites; (10)  $HO_2^-$  spillover between the nitrogen-doped carbon active sites and perovskite active sites. OCST also includes the pathway for the  $HO_2^-$  reduction/oxidation on the carbon with (5C) and (8C) steps for both C and N-doped C active sites. Steps (9) and (10); (4PC) and (4PE) were not simulated in parallel, only one of them was introduced to the model simultaneously to check its applicability using the experimental data.

Two reaction mechanisms for ORR and HPRR/HPOR on the oxides provided the best explanation for the observed experimental findings. The first one, shown in Figure 4.4 adapts the reaction steps proposed by Cushing, Goodenough with (1P), (2P), (3P), (4PE), (5P) steps, where P refers to the reaction occurring on the perovskite surface and PE refers to the electrochemical version of step (4) [72], [226], [227]. The second reaction mechanism, proposed by Strasbourg's group consists of the same reaction steps but includes an alternative irreversible step of  $HO_2^-$  *chemical* decomposition (4PC) instead of (4PE) step [68], [73]. It was previously successfully applied to simulate the catalytic activity trends for various oxides in the alkaline media towards the ORR and HPRR/HPOR as well as the kinetic control of HPRR reaction at high overpotentials for the several studied manganese oxides [79]. All the proposed reaction mechanisms were modeled in order to ascertain which mechanism best described the observed trends in the LSCO/VC and NC catalytic activity. The ORR reaction on carbons was simulated by the mechanistic  $2e^-$  reduction of  $O_2$  to  $HO_2^-$ , which comprises of steps (6C), (7C), and (8C) in Figure 4.4, where C refers to a step on the carbon surface. It was successfully used previously to describe ORR RDE on carbon without overcomplicating the model [68], [73], [79].

According to the XPS data on nitrogen content in the NC, ORR and HPRR/HPOR on NC were modeled through the addition of 2% more active sites, which follow the same reaction mechanism but with faster ORR kinetics [216]. For the NC, the same total active sites surface density was used as for VC because of the following considerations: (i)

Catalytic activity of carbons does not linearly scale with the BET or BJH surface areas and (ii) Correct relative rate constants values should be obtained for both NC and VC in order to reproduce the experiment [61]. Hence, the reaction pathway is conserved for both carbons with the renormalization of the reaction rate by the active sites surface density and their contribution to the ORR for the composite materials may be correctly accounted without accurate estimation of their absolute rate constant values.

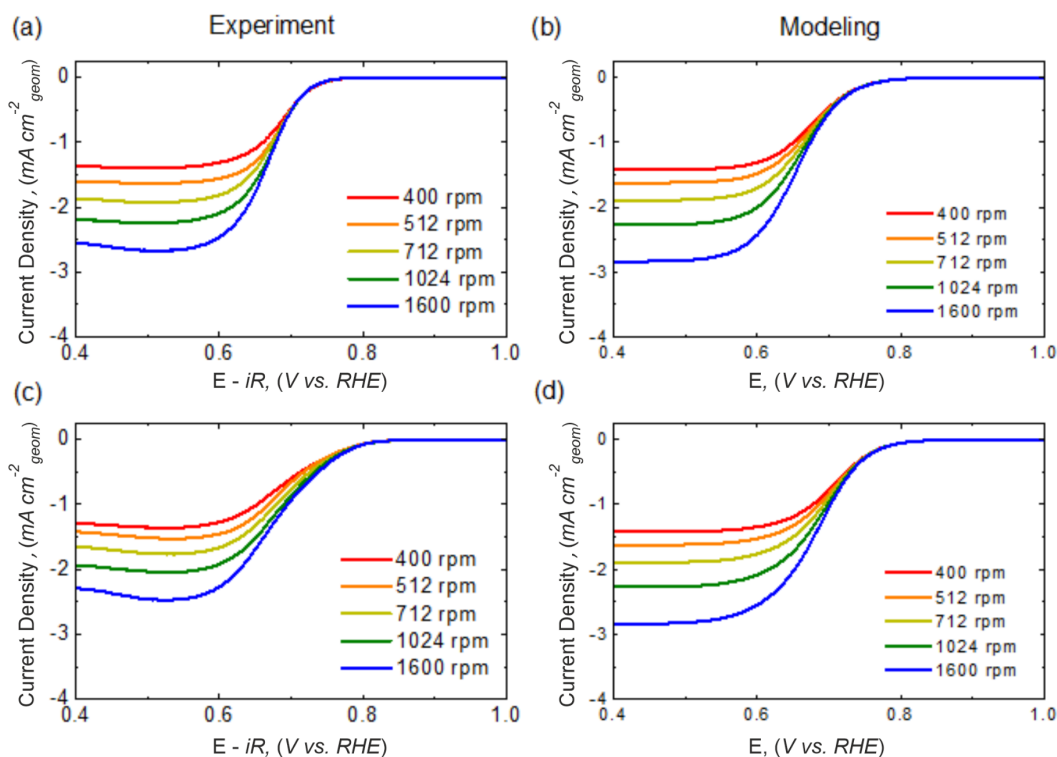


Figure 4.5 Experimental (a, c) and simulated (b, d) ORR RDE voltammograms for Vulcan carbon (a, b) and nitrogen doped mesoporous carbon (c, d) in  $O_2$  saturated 0.1 M KOH solution and total electrode mass loadings  $35.7 \text{ ug cm}^{-2}_{\text{geom}}$ .

As the influence of the carbon type on the overall ORR activity is stronger than that of Sr doping ratio on LSCO, the attempt to simulate it is provided first by modeling LCO/VC and LCO/NC using the two abovementioned reaction mechanisms for oxides. Three options of carbon type influence on the overall catalytic activity towards the ORR were

considered: 1) Faster ORR kinetics on NC leads to the higher rate of  $\text{HO}_2^-$  generation, which is further adsorbed and reduced on perovskite, increasing the overall catalytic activity. 2)  $\text{O}_2$  spillover between the nitrogen-doped carbon active sites and perovskite active sites in step (9). 3)  $\text{HO}_2^-$  spillover between the nitrogen-doped carbon active sites and perovskite active sites in step (10). The assumptions 2) and 3) were considered as the spillover of oxygen-containing species was observed experimentally between the carbon and Pt at Pt/C porous electrodes [228]. Hence, an attempt to use the spillover effects could be applied to explain the synergy between the metal oxides and carbon.

Effective steps (9) and (10) in Figure 4.4 serve as an initial attempt to introduce  $\text{O}_2$  and  $\text{HO}_2^-$  spillover effects to the model. The further refinement of the modeling approach to simulate the spillover effects requires additional experimental data to better understand the oxide/carbon interface.

The consecutive way in which the model parameters are adjusted are as follows: 1) The VC and NC rate constants were adjusted to reproduce the experimental ORR and HPRR/HPOR results on the respective bare carbons; 2) Using the adjusted VC rate constants, the LCO rate constants were adjusted to reproduce experimental data for ORR and HPRR/HPOR at LCO/VC within the reaction mechanisms with (4PC) and (4PE) steps; 3) Using the previously adjusted parameters for LCO and NC, the abovementioned hypotheses for carbon type influence were tested; and 4) The most successful reaction mechanism and hypothesis for the carbon type influence were applied to describe the catalytic activity trends with the Sr doping ratio in LSCO. For these reasons, the modeling parameters are provided for the most active composition, LSCO64.

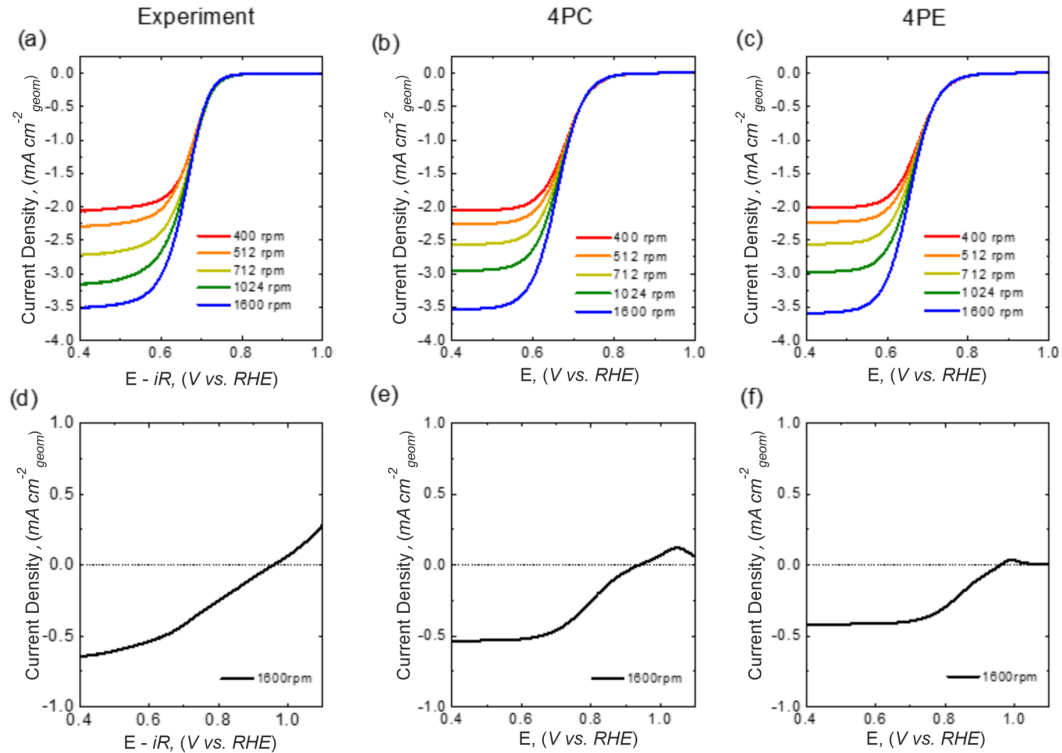


Figure 4.6 ORR RDE voltammograms (a-c) in  $O_2$  saturated 0.1M KOH. HPOR/HPOR RDE voltammograms (d-f) in Ar-purged 0.1 M KOH solution with 1.2 mM  $HO_2^-$ . 30 wt% LCO/VC composite catalyst was used with total electrode mass loading equal to  $51 \mu g cm^{-2}_{geom}$ . (a, d) – experimental results. (b, e) – modeling results with the (4PC) reaction mechanism. (c, f) – modeling results with the 4PC reaction mechanism.

The simulated ORR RDE voltammograms for the carbons, shown in Figure 4.5, qualitatively reproduce experimental results. For the NC, the positive shift of ORR onset potential comparing to that of VC was reproduced. The more detailed simulation of the well-observed minimum of ORR currents at 0.55 V vs. RHE for NC, as well as the voltammograms shape at average potentials, require the improvement of the model, with possible addition of a direct  $4e^-$  oxygen reduction pathway occurring on the carbon (rather than the  $2e^- O_2$  to  $HO_2^-$ ) with competition of different active sites at NC at low overpotentials and carbon surface poisoning at high overpotentials [39]. In order to do that,

additional experimental studies are required to make the model improvement physically relevant. The negligible simulated HPOR/HPRR currents on the VC and NC are consistent with the low values observed in experiments.

The results of the LCO/VC simulation are shown in Figure 4.6. Both models, using either the (4PE) or the (4PC) step for  $\text{HO}_2^-$  decomposition, semi-quantitatively reproduce ORR RDE voltammograms. Within the model considering the (4PC) step the ORR proceeds on the LCO/VC composite material through steps (6C), (7C), (8C), (5P), (4PC),  $2 \times$  (1P). The LCO by itself has a slow (2P) step which prohibits the series  $2e^- + 2e^-$  pathway on the oxide. The model qualitatively reproduces the zero current potential as well as the incipient current regions for HPRR/HPOR RDE voltammograms. The reaction mechanism following the (4PC) step shows better results for the reproduction of HPRR kinetically limiting currents at high overpotentials due to the higher degree of freedom for the simultaneous adjustment of ORR and HPRR kinetically-limiting currents with the two chemical steps (4PC) and (5P). Both models have limitations on the maximum positive potential that can be applied because the surface active sites are passivated at the positive potentials by the reverse reaction (-1P). One can potentially overcome this limitation via the introduction of interactions between the adsorbed reaction intermediates via Frumkin isotherms, consideration of the outersphere reaction regime at positive potentials, or inclusion of multiple LCO active sites with different distributions of their formal surface redox potential. All of these require additional experimental data beyond the scope of this study.

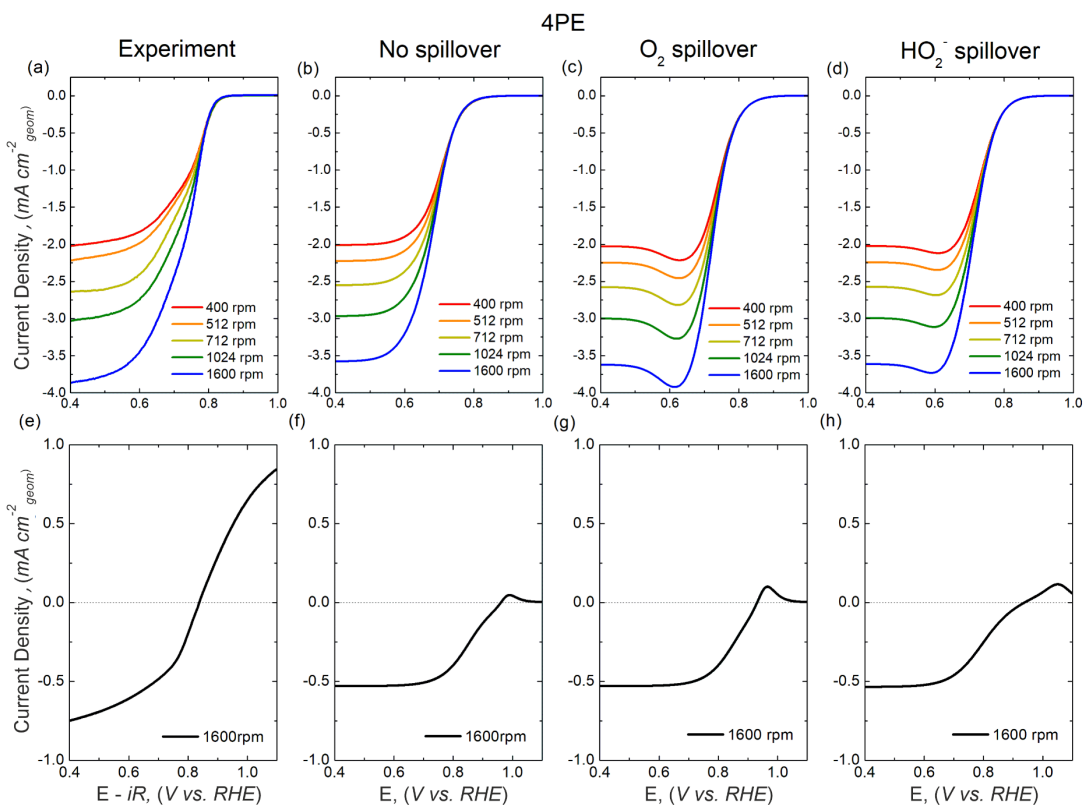


Figure 4.7 ORR RDE voltammograms (a-d) in  $O_2$  saturated 0.1M KOH. HPOR/HPOR RDE voltammograms (e-h) in Ar-purged 0.1 KOH solution with 1.2mM  $HO_2^-$ . 30 wt% LCO/NC composite catalyst was used with total electrode mass loading equal to  $51 \text{ ug cm}^{-2}_{\text{geom}}$ . (a, e) experimental results. (b, f), (c, g), (d, h) modeling results for (4PE) reaction mechanism without/with  $O_2$ /with  $HO_2^-$  spillover respectively.

Similar results on LCO/NC (Figure 4.7) shows that neither increased ORR activity of NC towards the  $2e^-$  oxygen reduction, nor  $HO_2^-$  and  $O_2$  spillover steps can explain simultaneous increase in HPOR currents, ORR currents, and change of the ORR currents slope at the LCO/NC within the model assumptions and (4PE) step for  $HO_2^-$  reduction. The rate constants for spillover steps were adjusted to reproduce the shift in the ORR onset potential. Additionally, an artificial minimum of ORR currents was observed with the  $O_2$  and  $HO_2^-$  spillover due to the competitive  $O_2$  reduction at the VC and NC active sites. Thus

the 4PE pathway can be excluded in the mechanism of the ORR on the LSCO/carbon composites.

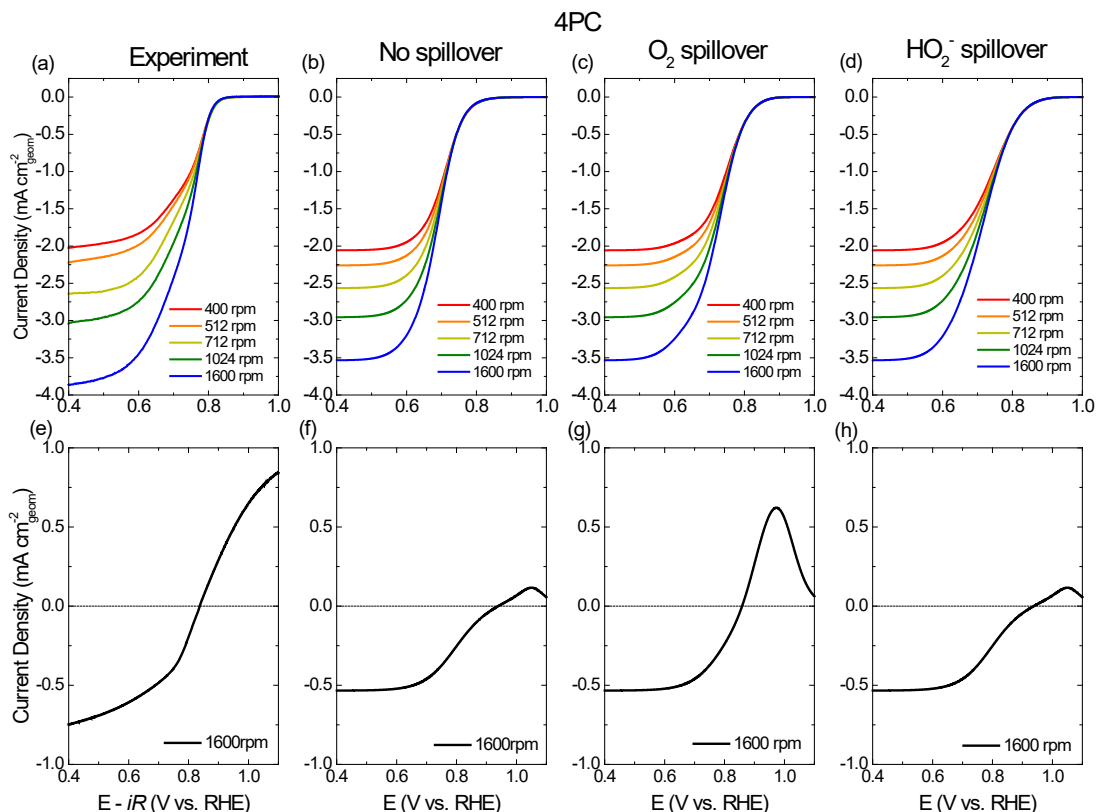


Figure 4.8 ORR RDE voltammograms (a-d) in  $O_2$  saturated 0.1 M KOH. HPRR/HPOR RDE voltammograms (e-h) in  $N_2$ -purged 0.1 M KOH solution with 1.2 mM  $HO_2^-$ . 30 wt% LCO/NC composite catalyst was used with total electrode mass loading equal to  $51 \mu g \text{ cm}^{-2}_{\text{geom}}$ . (a, e) – experimental results. (b, f), (c, g), (d, h) – modeling results for (4PC) reaction mechanism without/with  $O_2$ /with  $HO_2^-$  spillover respectively.

For the nitrogen-doped carbon (NC) the best result of simultaneous qualitative reproduction of experimental results was obtained for the reaction mechanism with the (4PC) step for  $HO_2^-$  decomposition and (9)  $O_2$  spillover step, as shown in Figure 4.8. This option was able to reproduce: (i) The negative shift of the HPRR/HPOR mixed current potential, (ii) The initial HPOR region, (iii) The positive onset potential shift for the ORR,



options such as higher NC activity (Figure 4.8 (2b), (2f)) and  $\text{HO}_2^-$  spillover (Figure 4.8, (2d), (2h)) are not able to simultaneously reproduce ORR and HPRR/HPOR RDE voltammograms. This suggests a differing mechanism in the oxygen-containing species transfer step (9) or (10) when nitrogen is introduced into the carbon structure and may indicate the buildup of a superoxide like  $\text{O}_2^-$  on nitrogen-doped carbon.

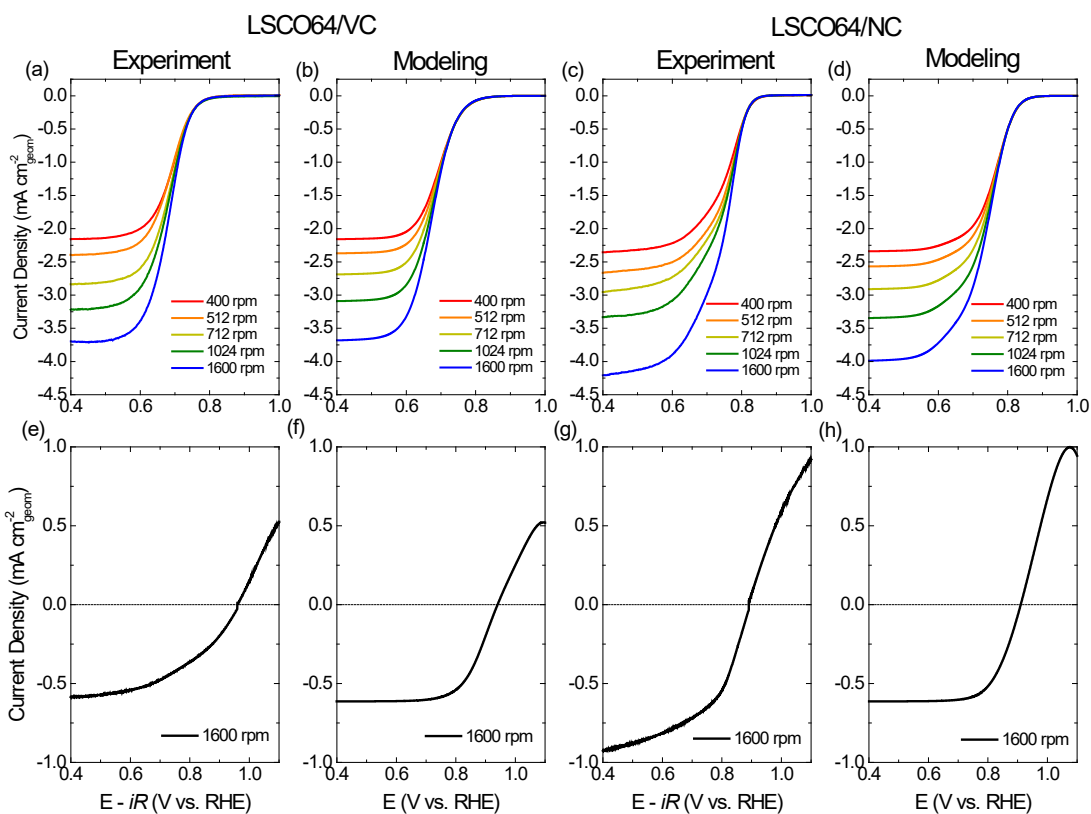


Figure 4.10 ORR RDE voltammograms (a-d) in  $\text{O}_2$  saturated 0.1 M KOH. HPRR/HPOR RDE voltammograms (e-h) in  $\text{N}_2$ -purged 0.1 M KOH solution with 1.2 mM  $\text{HO}_2^-$ . 30 wt% LCO/NC composite catalyst was used with total electrode mass loading equal to  $51 \text{ ug cm}^{-2}_{\text{geom}}$ . (a, e), (c, g) – experimental results for LSCO/VC and LSCO64/NC respectively. (b, f), (d, h) – modeling results using the reaction mechanism with (4PC) step for LSCO/VC and LSCO64/NC respectively.

Finally, an attempt to model the higher catalytic activity of LSCO64 was made as shown in Figure 4.10. The higher surface hydroxylation at higher Sr content was qualitatively modeled by positively shifting the surface  $\text{Co}^{3+}/\text{Co}^{4+}$  formal redox potential by 120 mV relative to LCO. If one wants to fix this parameter as it was done for LCO, the same experimental procedure should be applied [82]. The transfer coefficient for the (2P) step was changed from the 0.5 to 0.8 to reproduce the ORR RDE voltammograms slopes. The forward and backward rate constants should be unavoidably simultaneously adjusted for (2P) (increased 2 times), (3P) (decreased 10 times), and (9) (increased 2 times) reaction steps. For the LSCO64 the ORR kinetically limiting currents at high overpotentials are different for VC and NC support, which is opposite to what was observed at LCO. From the modeling point of view, it could be explained by (i) the faster (4PC) step, or different influence of the carbon type on the oxide utilization via the improvement of the electrical contact. In order to check it, an oxide utilization enhancement should be experimentally estimated [82]. Moreover, because the LSCO64 has lower bulk stability than LCO, one cannot exclude an option that the surface structure, as well as the surface active sites and their density, are different from the ones for LCO [214]. Regardless, the modeling suggests that the origin in the higher catalytic activity originates from a fast peroxide decomposition (4PC) step.

On LCO/VC, NC and LSCO64/VC, NC the rate-limiting step was identified as the decomposition of the hydroperoxide adsorbate (4PC). This step requires both  $\text{OH}^-$  and  $\text{HO}_2^-$  adsorbates and results in a  $\text{Co}^{4+}$  species. Considering the XPS hydroxylation information and the oxidation state data derived through iodometric titrations, the high reactivity of LSCO46 and LSCO64 can be explained as an optimal balance in both intermediate oxidation state (which reflects the energy of the electronic states of the catalyst) and relative hydroxylation. In contrast, SCO, which has a similar oxidation state but higher surface hydroxylation results in low HPOR/HPRR/ORR activity. Similarly, LCO has a lower oxidation state and lower surface hydroxylation resulting in low activity. The change in Tafel slope at high potentials for NC (in comparison to VC) can be explained by a higher mass transfer

of reactants through the O<sub>2</sub> spillover step (9) leading to high coverage of intermediates at lower overpotential.

#### 4.4. Conclusions

The role of carbon as a co-catalyst was investigated through supporting the LSCO catalysts on either Vulcan carbon with no nitrogen or on a 2 at. % N-doped carbon. It was found that the interactions between LSCO and carbon in composite systems played a crucial role in describing the activity of the series. The proposed microkinetic model qualitatively reproduced experimental data for ORR RDE on VC and NC, ORR and HPRR/HPOR data for LCO/VC, NC, and LSCO64/VC, NC. Within the assumptions of the developed model, two reaction mechanisms with chemical and electrochemical hydroperoxide decomposition steps were considered. Three hypotheses for the catalytic activity enhancement due to nitrogen incorporation in the carbon were elucidated. It was shown that the reaction mechanism with a chemical step for HO<sub>2</sub><sup>-</sup> decomposition on the perovskite surface, HO<sub>2</sub><sup>-</sup> mass transfer between VC and the perovskite, and O<sub>2</sub> spillover between the NC and perovskite active sites provided the best qualitative reproduction for the ORR and HPRR/HPOR RDE experiments. Despite the simplified model for ORR and HPOR/HPRR on carbon and neglect of adsorbates interactions, the results of this work show that use of a nitrogen-doped carbon support leads to a 5-fold catalytic activity enhancement for ORR on LSCO/carbon composites through enhancement of the O<sub>2</sub> spillover pathway. This work serves as the first step to the elucidation of carbon support influence in composite oxide/carbon electrodes and a better description of catalytic activity trends with Sr doping ratio in LSCO. From this study, it is clear that the rational design of perovskite electrocatalysts requires a complete understanding of the composite systems used in the studies and that the role of carbon in the reduction of oxygen on metal oxides cannot be overlooked. The undoubtedly high complexity of the suggested ORR mechanism, requires the quantification of inverse uncertainty propagation in order to access its capability for quantitative but not qualitative insights on the estimated model parameters. It should also target the further molecular level study to the model parameters,

which are weakly constrained from the available experimental data. Given the complexity of the suggested mechanism, the simpler model system is required to approbate the inverse uncertainty characterization techniques and to develop the approach to determine the accessible detailing level of ORR mechanism detailing based on the completeness of the available experimental data and its accuracy.

## Chapter 5. Uncertainty Quantification for Quantitative ORR Mechanism Selection.

The results reported in this chapter are based on the following publication [A. A. Kurilovich, C. T. Alexander, E. M. Pazhetnov, and K. J. Stevenson, “Active learning-based framework for optimal reaction mechanism selection from microkinetic modeling: a case study of electrocatalytic oxygen reduction reaction on carbon nanotubes,” *Phys. Chem. Chem. Phys.*, vol. 22, no. 8, pp. 4581–4591, 2020]. As it is shown in the previous chapter, the catalytic activity trends within the LSCO/VC, NC series require high minimal complexity of the microkinetic models in order to be reproduced. Together with the limited amount of the RRDE experimental data, it raises the question about the predictive capability of the suggested model and the corresponding reaction mechanism. Namely, if the available experimental data and suggested reaction mechanism provide the unique and correct explanation of observed catalytic activity trends by the unique set of model parameters. Hence, their uncertainties arising from experimental errors should be quantified and used as a criterion to elucidate the detailing level of the ORR mechanism (i.e. choose the reaction mechanism with the optimal complexity), which can be verified from the experiments.

Therefore, the aim of this chapter is to develop the framework for the macroscale model selection using not only the precision of the experimental data fitting but also the uncertainty of the reaction mechanism parameters (rate constants, charge transfer coefficients, etc.) It should narrow the gap between the experiments and macroscale simulations in the multiscale modeling approach. In order to aim this specific part, the *ab initio* calculations are intentionally avoided to bound the model parameters. Therefore, it should be possible to elucidate the connection between the available experimental data and the details on the reaction mechanism it can reliably provide. This should make further validation of the proposed reaction mechanism by the molecular level insights more conclusive.

The ORR on multiwalled carbon nanotubes (CNTs) is used as model system. CNTs are good model catalysts since they catalyze ORR through the  $2e^-$  mechanism with  $O_2$  being reduced to  $HO_2^-$  in alkaline media [41], [51], [53], which decreases the number of possible

elementary steps compared to the Pt or TMO/C systems. As such, a rather simple model can be proposed and examined on the influence of experimental dataset completeness on achievable detailing of the reaction mechanism. In this work, the framework of the optimal model selection is demonstrated based on the RDE experimental data fitting using the mean-field MF-MKM.

## 5.1. Materials and Methods

### 5.1.1. Chemicals

All chemicals were used as received. 5 wt% Nafion solution in lower alcohols and m-xylene (>99%) were purchased from Sigma-Aldrich while ferrocene (99%) was obtained from Alfa Aesar. Oxygen (research-grade, 99.999% purity), argon (research-grade 99.999% purity) and hydrogen (research-grade, 99.999% purity) were obtained from Praxair. Millipore deionized water (18 M $\Omega$  cm) was used.

### 5.1.2. Carbon Nanotube Synthesis

CNTs were prepared by C. T. Alexander using a floating catalyst chemical vapor deposition (CVD) method as described previously [53]. Briefly, a 2 mL flask and 1 mL glass syringe were rinsed four times with m-xylene to remove trace ferrocene from previous runs. After the flask was dried using a Kim wipe, 156.4 mg of ferrocene was added to the flask which was then capped with a rubber septum and flushed with argon for five minutes using a pair of syringe needles to flush out oxygen and moisture from the flask with one needle and relieve pressure with the other needle. Then, m-xylene was injected into the flask to make the solution 104.28 mg ferrocene/mL of m-xylene (or 9.6 wt% ferrocene). The solution was then sonicated to speed the ferrocene dissolution rate until there were no visible solids left in the deep orange solution. Then, 1 mL of the solution (with an extra 0.1 mL added to account for the plastic tubing volume for a total of 1.1 mL) was injected into the first stage of a two-stage furnace at a rate of 1.2 mL hr<sup>-1</sup> in a quartz tube with argon flowing at 750 cm<sup>3</sup> min<sup>-1</sup>. The first stage was held at 200°C while the second stage was held at 760°C for ten minutes prior to and during injection to eliminate

thermal gradients. The synthesis was run for 60 minutes after which the argon flow rate was reduced to  $200 \text{ cm}^3 \text{ min}^{-1}$ , the furnace was turned off and allowed to cool for three hours until the quartz tube was cool enough ( $\sim 150^\circ\text{C}$ ) to handle and collect the CNTs.

### *5.1.3. Surface Area Characterization*

The CNT's surface area was measured by C. T. Alexander using a Quantachrome Instruments NOVA 2000 high-speed surface area BET analyzer at 77 K. The samples were degassed at  $200^\circ\text{C}$  under vacuum for eight hours prior to measurement and the  $P/P_0$  range for data analysis was from 0.05 to 0.30.

### *5.1.4. Material Characterization*

Chemical analysis of sample surfaces was carried out by E. M. Pazhetnov with X-ray photoelectron spectroscopy (XPS) technique. measurements were performed using the PHI 500 VersaProbe II spectrometer with a spherical mirror analyzer. Al  $K\alpha$  monochromatic x-ray source with 1486.6eV X-ray energy was utilized. Emitted photoelectrons were collected at the normal incidence. Survey spectra were recorded with 1.0 eV step size while high-resolution spectra were recorded with 0.1 eV step size. Electron neutralizer was not applied due to the good electronic conductivity of material under study. Following the commonly used procedure for X-ray spectroscopy data analysis, high-resolution XPS spectra were processed in two steps. Firstly, photoelectron backgrounds were subtracted from the high-resolution spectra using Shirley function approximation. The resulting spectra were used for element content quantification. Secondly, the peak fitting procedures with mixed Gauss-Lorentz (Voigt) profile components were applied to O1s high-resolution spectra in order to quantify the oxygen functional groups. All the high-resolution spectra were calibrated to the C1s binding energy 284.6eV. Obtained results were then compared with the ones for previously studied CNTs [53].

### *5.1.5. Electrochemical Characterization*

Electrochemical testing was performed by C. T. Alexander on a Metrohm Autolab PGSTAT 302N with high-speed rotators and rotating disk electrodes (RDEs) from Pine

Instruments. The RDEs consisted of a 5 mm diameter glassy carbon electrode (GCE) surrounded by a PEEK sheath. The GCE was prepared by first sonicating it in a 50:50 (by volume) water: ethanol solution for thirty seconds, followed by polishing in an alternating figure-eight pattern on a wet polishing pad with 50 nm alumina and DI water. The electrode was then rinsed with DI water from a squirt bottle and sonicated in a fresh 50:50 water: ethanol (by volume) solution for thirty seconds. The electrode was then allowed to dry for one hour prior to depositing the CNTs via an ink under a covering open to ambient to prevent dust from falling on the electrode but allow the solvent to evaporate. The CNT ink was prepared by first ball milling the CNTs for three minutes using a Wig-L-Bug ball mill and then adding it to a 0.05 wt% Na-substituted Nafion in ethanol solution to make the solution 1 mg mL<sup>-1</sup>. The solution was made by mixing 0.180 mL of 5 wt.% Nafion in ethanol, 0.360 mL of 0.1 M NaOH and 19.258 mL of ethanol. The CNT ink was then sonicated for two hours and then 10 µL was pipetted onto the polished GCEs in 3.5, 3.5 and 3 µL increments which were covered and spun at ~185 r.p.m. to dry before adding the next increment. At first, the CNTs appeared to not wet the ink well and would splatter on the inside walls during sonication, but after one to two hours the CNTs appeared to better wet the ink solution. Just before placing the electrodes in the electrolyte, a drop of electrolyte was added to cover the electrode surface, 7 µL of isopropanol was pipetted into the droplet and pulsed several times to remove air bubbles trapped in the film. The electrode surface was then rinsed with 1 mL of electrolyte to remove residual isopropanol.

Electrochemical tests were performed in fresh 0.1 M KOH (pH = 13.24) from 400 to 1600 r.p.m. using a 1 M KOH Hg/HgO reference electrode and Au wire counter electrode enclosed behind a glass frit. The electrolyte resistance was measured to be 46 Ω using the positive feedback method and all curves were iR-corrected accordingly. O<sub>2</sub> or Ar was bubbled into the electrolyte for at least 35 minutes prior to ORR or HPOR/HPRR testing respectively. During HPOR/HPRR measurements, Ar bubbling was stopped and was instead flowed over the electrolyte surface to prevent bubbles from disturbing the measurement. ORR cyclic voltammograms (CVs) were scanned at 5 mV s<sup>-1</sup> from 0.9455 V to 0.3955 V vs RHE. RHE was measured following the same procedure as described

previously [53]. Linear potential sweep measurements were made for HPOR and HPRR starting from the open circuit potential after adding the appropriate amount of hydrogen peroxide and were swept at 5 mV s<sup>-1</sup> to 0.3 V and -0.4 V vs Hg/HgO, respectively. All measurements were made in triplicate and a new solution was used for each HPRR/HPOR measurement at a different rotation rate.

## 5.2. Theoretical Basis

### 5.2.1. Experimental error calculation

Given an experiment type (ORR or HPRR/HPOR) and RDE rotation rate, the data points from triplicate RDE CVs were allocated to the 200 equal potential intervals (“bins”). For each bin the mean geometric current density  $\hat{I}_{geom}(s, \omega, b)$  was calculated according to (5.1).

$$\hat{I}_{geom}(s, \omega, b) = \frac{1}{N(b)} \sum_{i=1}^{N(b)} I_{geom}(s, \omega, b, i) \quad (5.1)$$

Here,  $s$  is the experiment type (ORR or HPRR/HPOR),  $\omega$  is the RDE rotation rate,  $b$  is the bin,  $i$  is the data point number in a particular bin,  $N(b)$  is the total number of data points in the bin, and  $I_{geom}(s, \omega, b, i)$  is the geometric current density. The experimental dataset for further modeling was formed as a set of potentials equal to half sum of left and right bin boundaries and corresponding mean geometric current densities for each  $\omega$  and  $s$ . For each bin, the unbiased variance  $S(s, \omega, b)$  was calculated using equation (5.2):

$$S(s, \omega, b) = \frac{1}{N(b) - 1} \sum_{i=1}^{N(b)} (\hat{I}_{geom}(s, \omega, b) - I_{geom}(s, \omega, b, i))^2 \quad (5.2)$$

Then the mean squared error (MSE) for a given  $\omega$  and  $s$  was calculated by averaging out the unbiased variances in all bins (5.3).

$$MSE(s, \omega) = \frac{1}{N_{bins}} \sum_{b=1}^{N_{bins}} S(s, \omega, b) \quad (5.3)$$

It was further averaged out by  $\omega$  to calculate MSE for one experiment type, e.g. ORR RDE (5.4).

$$MSE(s) = \frac{1}{N_{\omega}} \sum_{\omega} MSE(s, \omega) \quad (5.4)$$

The overall MSE experimental error is obtained by summing up the MSEs for each type of experiment (5.5).

$$MSE_{experimental} = \sum_s MSE(s) \quad (5.5)$$

### 5.2.2. Modeling details

Three considered ORR reaction mechanisms on CNTs were formalized using the MF-MKM [68], [73], [79]. All adsorption/desorption steps were assumed to follow the Langmuir isotherm. Mass transfer of the  $O_2$  and  $HO_2^-$  in the electrolyte is considered using the approximate analytical solution for RDE obtained by Levich [100]. The constructed system of ordinary differential equations was solved numerically in a steady-state approximation mimicking the low scan rates in performed RDE experiments. Flat electrode surface with uniformly distributed carbon active sites, which are equally accessible for  $O_2$  and  $HO_2^-$  species was considered in simulations. The concentration profile on the vicinity of the electrode surface was assumed to be linear for  $O_2$  and  $HO_2^-$  species. The diffusion in the bulk of the electrode was neglected because of the low catalyst loadings. All rate constant values are reported for the 0.1 M KOH solution. The rate constants for effective  $2e^-$  charge transfer steps are given at  $E_0 = 0.7404$  V vs. RHE. Prior to each numerical solution, the backward rate constant value for the charge transfer step was numerically calculated to reproduce the standard potential of  $O_2/HO_2^-$  redox pair in alkaline media. The applied potential was stepped down by decrements of 0.5 mV starting from 1.0 V vs RHE

for ORR and 1.2 V. vs RHE for HPRR/HPOR. For each potential value, the corresponding system of nonlinear algebraic equations is solved numerically by the `fsolve` function from Python `scipy.optimize` library, which is the wrapper around MINPACK `hybrd` and `hybrj` algorithms [229]. The variables were standardized. The relative tolerance parameter `xtol` was set to  $10^{-6}$ .

In this work, ‘model parameters’ refer to independent pre-exponential rate constants and charge transfer coefficients which define the CV shape but remain constant during the solution of the corresponding system of non-linear equations. The adopted data collaboration approach for the uncertainty quantification of the model parameters space was performed using the off-the-shelf implementation of the Tree-Structured Parzen estimator algorithm (TPE) [176] in the Python `hyperopt` library [230].

TPE requires warming up, which is done by parameters random sampling from specified prior distributions, which mimics our knowledge on possible model parameters values. The TPE global optimization outcome is highly dependent on this step. Multiple starts are performed with the results merged together in order to archive a more accurate sampling of the parameter space. In each start (i) 200 points were sampled from loguniform and uniform prior distributions for rate constants and charge transfer coefficients respectively, (ii) 800 points were evaluated by TPE global optimization procedure. The uniformness of the sampling is provided by randomness and independence of the warm-up step in each start, while low errors are achieved by the global optimization stage. 100 starts were performed with the wide intervals of model parameters prior distributions and 100 starts were made for the reduced intervals of the parameters, where low values of the objective function were observed. The objective function for the single experiment type is calculated as MSE between the averaged experimental CVs and linearly interpolated simulated CVs (5.6).

$$MSE(s) = \frac{1}{N_\omega} \sum_{\omega} \frac{1}{N_{bins}} \sum_{b=1}^{N_{bins}} \left( \hat{I}_{geom}(s, \omega, b) - I_{simulated}(s, \omega, V(b)) \right)^2 \quad (5.6)$$

Here,  $V(b)$  is the corresponding experimental potential. For the simultaneous fitting of the complete experimental dataset, the MSEs of single experiment types were summed up.

In the case the numerical model does not converge, the MSE was explicitly set to be very high, so the regions with high stiffness in the parameters space are avoided on the global optimization stage in TPE.

### 5.2.3. Model equations

The effective diffusion layer thickness  $\delta_{O_2,HO_2^-}$  {cm} for  $O_2$  and  $HO_2^-$  is evaluated from the approximate analytical solution for RDE reported by Levich [100].

$$\delta_{O_2,HO_2^-} = 1.61D_{O_2,HO_2^-}^{1/3} \nu^{1/6} \omega^{-1/2} \quad (5.7)$$

Here,  $D_{O_2,HO_2^-}$  {cm<sup>2</sup> s<sup>-1</sup>} are diffusivities of  $O_2$  and  $HO_2^-$  respectively,  $\nu$  {cm<sup>2</sup> s<sup>-1</sup>} – kinematic viscosity,  $\omega$  {rad s<sup>-1</sup>} – RDE rotation rate. The values for  $D_{O_2,HO_2^-}$  and  $\nu$  were taken from literature data [58].

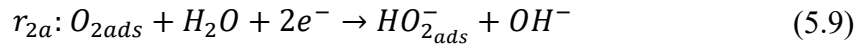
- Model (a)

Three steps are considered within this model.

1) Oxygen adsorption/desorption step on/from the surface:



2) Effective 2e<sup>-</sup> reduction/oxidation step of/to  $O_2$  to/from  $HO_2^-$ . Reaction product remains adsorbed on the surface:



3)  $HO_2^-$  desorption/adsorption step from/on the surface:



The rates of steps can be formally expressed as follows:

$$r_{1a} = k_{1a}c_{O_2}(1 - \theta_{O_2} - \theta_{HO_2^-}) - k_{-1a}\theta_{O_2} \quad (5.11)$$

$$r_{2a} = k_{2a}\theta_{O_2} \exp\left(-\frac{\alpha_{2a}F(E - E_o)}{RT}\right) \quad (5.12)$$

$$- k_{-2a}\theta_{HO_2^-} \exp\left(\frac{(1 - \alpha_{2a})F(E - E_o)}{RT}\right)$$

$$r_{3a} = k_{3a}\theta_{HO_2^-} - k_{-3a}c_{HO_2^-}(1 - \theta_{O_2} - \theta_{HO_2^-}) \quad (5.13)$$

Here  $k_{1a}/k_{-1a}$   $\{\text{cm}^3 \text{ mol}^{-1} \text{ s}^{-1} / \text{s}^{-1}\}$  are forward/backward rate constants for reaction step (5.8),  $k_{2a}/k_{-2a}$   $\{\text{s}^{-1} / \text{s}^{-1}\}$  are forward/backward rate constants for reaction step (5.9),  $\alpha_{2a}$   $\{1\}$ -charge transfer coefficient in (5.9),  $k_{3a}/k_{-3a}$   $\{\text{s}^{-1} / \text{cm}^3 \text{ mol}^{-1} \text{ s}^{-1}\}$  are forward/backward rate constants for reaction step (5.10),  $\theta_{O_2}/\theta_{HO_2^-}$   $\{1/1\}$  are surface coverages by  $O_2$  and  $HO_2^-$  species respectively,  $E_0$  – potential at which rate constants for electrochemical step were specified (0.7404 V vs. RHE in this work),  $R$  – universal gas constant  $\{\text{J K}^{-1} \text{ mol}^{-1}\}$ ,  $F$  – Faraday constant  $\{\text{C mol}^{-1}\}$ , and  $T$  – temperature  $\{\text{K}\}$  (298 K in this work).

The model, which was solved numerically:

$$\left\{ \begin{array}{l} \frac{d\theta_{O_2}}{dt} = 0 = r_{1a} - r_{2a} \\ \frac{d\theta_{HO_2^-}}{dt} = 0 = r_{2a} - r_{3a} \\ D_{O_2} \left( \frac{dc_{O_2}}{dx} \right)_{x=0} \approx D_{O_2} \frac{c_{O_2}^* - c_{O_2}}{\delta_{O_2}} = \Gamma_C r_{1a} \\ D_{HO_2^-} \left( \frac{dc_{HO_2^-}}{dx} \right)_{x=0} \approx D_{HO_2^-} \frac{c_{HO_2^-}^* - c_{HO_2^-}}{\delta_{HO_2^-}} = -\Gamma_C r_{3a} \end{array} \right. \quad (5.14)$$

Here  $c_{O_2}/HO_2^-$   $\{\text{mol cm}^{-3}\}$  are concentrations of  $O_2$  and  $HO_2^-$  species in the vicinity of the electrode surface,  $c_{O_2}^*/HO_2^-$   $\{\text{mol cm}^{-3}\}$  are concentrations of  $O_2$  and  $HO_2^-$  in the bulk of electrolyte, given by oxygen solubility in 0.1 M KOH [231] and experimental conditions for HPRR/HPOR.  $\Gamma_C$  is CNT active site surface density  $\{\text{mol cm}^{-2}\}$ . It was recalculated from the value used in our previous simulations [218] for Vulcan Carbon XC-72 (VC) using the ratios of BET surface areas and mass loadings for VC and CNTs.

Finally, the geometric current density  $I_{geom}(E)$  is evaluated from:

$$I_{geom}(E) = -2F\Gamma_C r_{2a}(E) \quad (5.15)$$

- Model (b)

This model is obtained by simplification of the Model (a) by merging steps (5.9) and (5.10). No adsorbed  $HO_2^-$  considered (fast  $HO_2^-$  adsorption/desorption step).



Then, the rates will be:

$$r_{1b} = k_{1b}c_{O_2}(1 - \theta_{O_2}) - k_{-1b}\theta_{O_2} \quad (5.18)$$

$$r_{2b} = k_{2b}\theta_{O_2} \exp\left(-\frac{\alpha_{2b}F(E - E_o)}{RT}\right) - k_{-2b}c_{HO_2^-}(1 - \theta_{O_2}) \exp\left(\frac{(1 - \alpha_{2b})F(E - E_o)}{RT}\right) \quad (5.19)$$

Here  $k_{1b}/k_{-1b}$   $\{\text{cm}^3 \text{ mol}^{-1} \text{ s}^{-1} / \text{s}^{-1}\}$  are forward/backward rate constants for reaction step (5.16),  $k_{2b}/k_{-2b}$   $\{\text{s}^{-1} / \text{cm}^3 \text{ mol}^{-1} \text{ s}^{-1}\}$  are forward/backward rate constants for reaction step (5.17), and  $\alpha_{2b}$   $\{1\}$ - charge transfer coefficient in (5.17).

Numerical model:

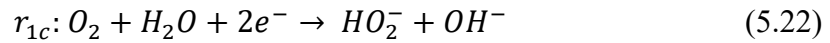
$$\left\{ \begin{array}{l} \frac{d\theta_{O_2}}{dt} = 0 = r_{1b} - r_{2b} \\ D_{O_2} \left( \frac{dc_{O_2}}{dx} \right)_{x=0} \approx D_{O_2} \frac{c_{O_2}^* - c_{O_2}}{\delta_{O_2}} = \Gamma_C r_{1b} \\ D_{HO_2^-} \left( \frac{dc_{HO_2^-}}{dx} \right)_{x=0} \approx D_{HO_2^-} \frac{c_{HO_2^-}^* - c_{HO_2^-}}{\delta_{HO_2^-}} = -\Gamma_C r_{2b} \end{array} \right. \quad (5.20)$$

Geometric current density:

$$I_{geom}(E) = -2F\Gamma_C r_{2b}(E) \quad (5.21)$$

- Model (c)

No surface coverages are considered within the simplest single step model:



Reaction rate:

$$r_{1c} = k_{1c}c_{O_2} \exp\left(-\frac{\alpha_{1c}F(E - E_o)}{RT}\right) - k_{-1c}c_{HO_2^-} \exp\left(\frac{(1 - \alpha_{1c})F(E - E_o)}{RT}\right) \quad (5.23)$$

Here  $k_{1c}/k_{-1c}$   $\{\text{cm}^3 \text{ mol}^{-1} \text{ s}^{-1} / \text{cm}^3 \text{ mol}^{-1} \text{ s}^{-1}\}$  are forward/backward rate constants for reaction step (5.22), and  $\alpha_{1c}$   $\{1\}$ - charge transfer coefficient in (5.22).

Numerical model:

$$\begin{cases} D_{O_2} \left( \frac{dc_{O_2}}{dx} \right)_{x=0} \approx D_{O_2} \frac{c_{O_2}^* - c_{O_2}}{\delta_{O_2}} = \Gamma_C r_{1c} \\ D_{HO_2^-} \left( \frac{dc_{HO_2^-}}{dx} \right)_{x=0} \approx D_{HO_2^-} \frac{c_{HO_2^-}^* - c_{HO_2^-}}{\delta_{HO_2^-}} = -\Gamma_C r_{1c} \end{cases} \quad (5.24)$$

Geometric current density:

$$I_{geom}(E) = -2F\Gamma_C r_{1c}(E) \quad (5.25)$$

Table 5.1 Estimated uncertainties of independent model parameters.

Model parameter	Overall parameter sampling interval	ORR fitting. Minimal interval, which contains all parameters giving the accuracy of fitting lower than experimental error.	ORR and HPRR/HPOR fitting. Minimal interval, which contains all parameters giving the accuracy of fitting lower than experimental error.
Model (a)			
$k_{1a}, s^{-1} cm^3 mol^{-1}$	$3.4 \times 10^{-4} \dots 3.4 \times 10^{10}$	$2.8 \times 10^6 \dots 1.3 \times 10^7$	$2.8 \times 10^6 \dots 7.2 \times 10^7$
$k_{-1a}, s^{-1}$	$3.4 \times 10^{-4} \dots 3.4 \times 10^{10}$	$3.4 \times 10^0 \dots 1.9 \times 10^8$	$2.2 \times 10^0 \dots 5.6 \times 10^7$
$k_{2a}, s^{-1}$	$3.4 \times 10^{-4} \dots 3.4 \times 10^{10}$	$4.8 \times 10^{-2} \dots 2.1 \times 10^6$	$2.3 \times 10^{-2} \dots 7.2 \times 10^6$
$k_{3a}, s^{-1}$	$3.4 \times 10^{-4} \dots 3.4 \times 10^{10}$	$4.4 \times 10^0 \dots 5.3 \times 10^8$	$5.5 \times 10^0 \dots 1.7 \times 10^9$
$k_{-3a}, s^{-1}$	$3.4 \times 10^{-4} \dots 3.4 \times 10^{10}$	$9.6 \times 10^0 \dots 3.4 \times 10^{10}$	$1.2 \times 10^1 \dots 7.7 \times 10^9$
$\alpha_{2a}, l$	0.40...0.95	0.40...0.92	0.43...0.90
Model (b)			
$k_{1b}, s^{-1} cm^3 mol^{-1}$	$3.4 \times 10^{-4} \dots 3.4 \times 10^{10}$	$2.8 \times 10^6 \dots 3.9 \times 10^6$	$2.8 \times 10^6 \dots 3.5 \times 10^6$
$k_{-1b}, s^{-1}$	$3.4 \times 10^{-4} \dots 3.4 \times 10^{10}$	$8.8 \times 10^0 \dots 5.5 \times 10^2$	$9.7 \times 10^0 \dots 1.7 \times 10^2$
$k_{2b}, s^{-1}$	$3.4 \times 10^{-4} \dots 3.4 \times 10^{10}$	$3.1 \times 10^{-2} \dots 5.9 \times 10^6$	$3.6 \times 10^{-2} \dots 1.5 \times 10^1$
$\alpha_{2b}, l$	0.40...0.95	0.42...0.91	0.64...0.90

### 5.3. Results and Discussion

The surface area of the CNTs was measured to be  $50.58 \text{ m}^2 \text{ g}^{-1}$  using BET  $\text{N}_2$  adsorption. XPS analysis performed by E. M. Pazhetnov shows no signal from Fe on the surface of CNTs (Figure 5.1).

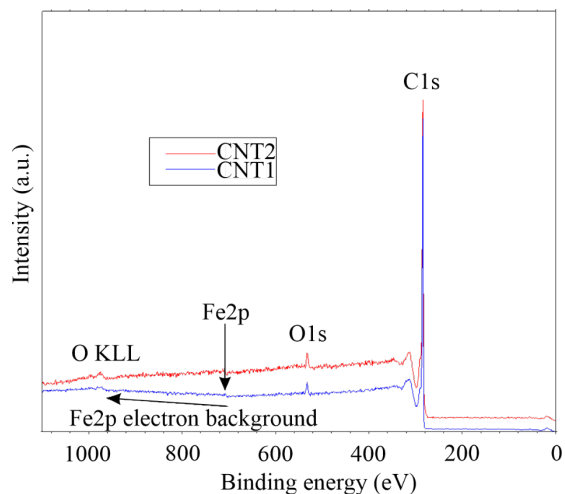


Figure 5.1 XPS survey spectra measured for two multiwalled carbon nanotube materials: CNT 1 sample – studied in [53] and CNT 2 sample – studied in this work. Spectra were shifted in Y-axis for the sake of comparison.

The C and O content is equal to 98.0 and 2.0 at% respectively. The high-resolution spectrum of O1s peak (Figure 5.2) was fitted by two Voigt components located at 531.2eV and 532.7eV respectively[232]. They can be attributed to carbonyl (C=O) and alcohol/ether (C-OH/C-O-C) groups with quantified content equal to 1.2 and 0.8 at%. The difference between CNTs under study and the ones discussed in the previous work [53] can be elucidated as follows: Despite the negligible but observable Fe content ( $<0.05$  at%), (Figure 5.2) and similar O content (1.7 at%), the O1s peak in the previously studied CNTs can be fitted only by one Voigt component attributed to alcohol/ether functional groups (Figure 5.2). As the content of highly hydrophilic alcohol groups is ca. 0.9 at. % lower for the currently studied CNTs then they should have higher hydrophobicity and hence the

lower electrochemical performance for ORR, which agrees with our ORR RDE experimental results.

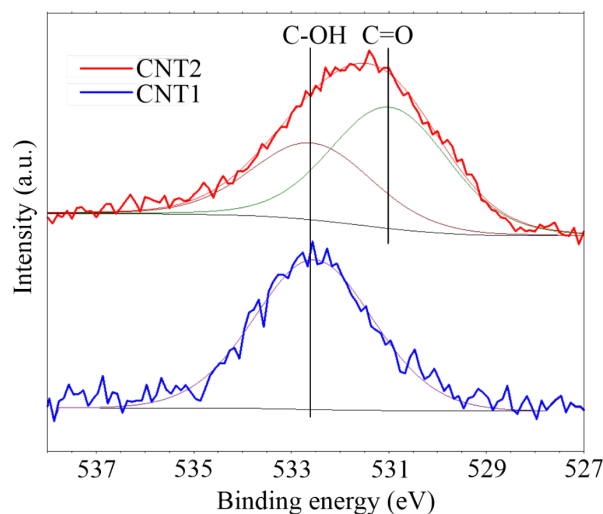


Figure 5.2 O1s high-resolution spectra measured for two multiwalled carbon nanotube materials: CNT 1 sample – studied in[53] and CNT 2 sample – studied in this work. Best peak fitting results. Spectra were shifted in Y-axis for the sake of comparison.

The experimental ORR RDE CVs (Figure 5.3 (a)) measured by C. T. Alexander reproducibly show that the geometric current densities at low potentials are more than 30% lower than the mass-transfer limited ones for  $2e^-$  ORR from Levich equation [100]. HPOR/HPRR current densities are negligible for both  $\text{HO}_2^-$  concentrations (Figure 5.3 (b, c)). It leads us to the following considerations: (i)  $\text{HO}_2^-$  does not undergo further  $2e^-$  reduction with ORR proceeding by  $2e^-$  pathway; (ii) the HPOR current is limited by backward step in ORR mechanism on CNTs. (i) is in agreement with our previous rotating ring-disk electrode (RRDE) study of CNTs, which showed  $\sim 100\%$   $\text{HO}_2^-$  yield during the ORR [53]. (ii) coincides with negligible HPRR currents and low HPOR currents on both Vulcan Carbon XC-72 and mesoporous nitrogen-doped carbon with 4.8 and 21.3 times higher BET surface areas than for CNTs [218]. The loadings were similar comprising  $35.7 \text{ ug cm}^{-2}$  instead of  $51 \text{ ug cm}^{-2}$  in this work.

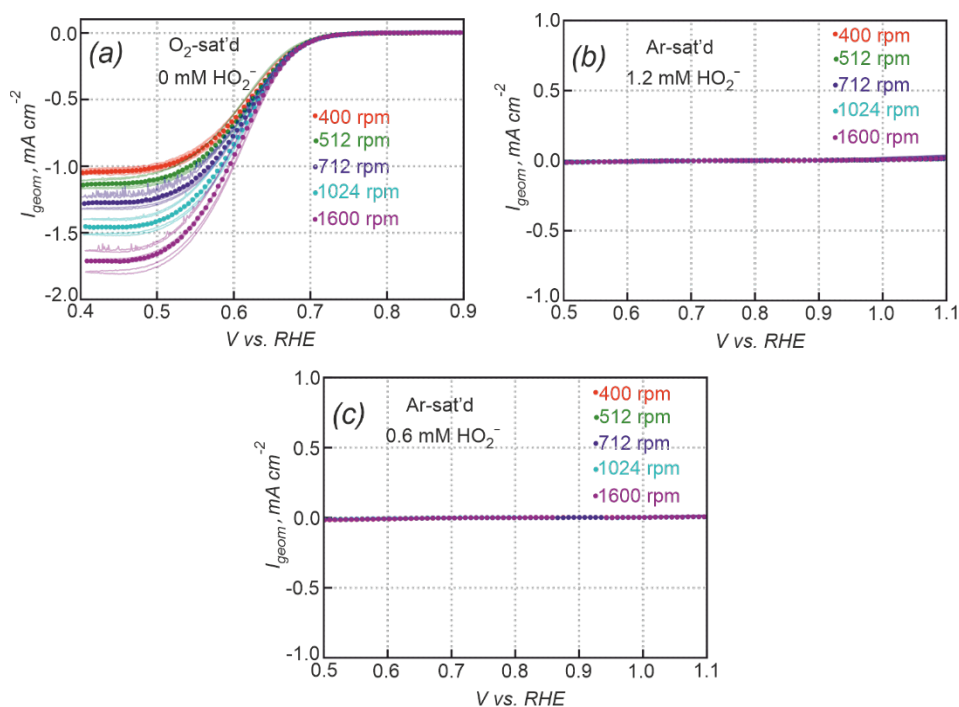


Figure 5.3 Experimental RDE CVs for CNTs with a mass loading of  $51 \mu\text{g cm}^{-2}$  in  $0.1 \text{ M KOH}$ . (a) ORR in  $\text{O}_2$ -saturated solution; HPRR/HPOR in Ar-purged solution with  $c_{\text{HO}_2^-}$  equal to (b)  $1.2 \text{ mM}$  and (c)  $0.6 \text{ mM}$ . Semi-transparent lines: independent experimental measurements, dots: averaged CVs.

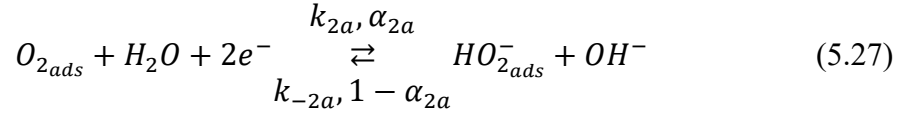
Before the numerical simulations, the prior distributions for the model parameters search by TPE should be defined. In the bottom-up multiscale approach, they are usually estimated from the DFT insights on the molecular level and TST [233]. The calculated adsorption and activation energies typically have uncertainties in the order of  $0.2 \text{ eV}$  [90]. Considering the exponential dependence of rate constants on activation energy in TST, it will lead to more than 3 orders of magnitude uncertainties in the determination of the reaction rate constants at room temperature. The error propagation is enabled by the choice of the prior intervals for model parameters.

In the top-down approach, model parameters' intervals are selected to be wide enough to explore possible reaction regimes and they represent the absence of our prior knowledge of the reaction mechanism. Based on the obtained results, the

systems for simulation on a molecular level may be suggested and studied. The error propagation is provided by experimental errors' influence on the selection of reaction mechanism which will be further studied on a molecular level.

The estimation of the active sites surface density relies on the knowledge about the nature of active sites on carbon for ORR and HPRR/HPOR, which is a matter of active research. As the one effective type of active site is considered in the models, the absolute values of rate constants are not so important as their ratios. So the uncertainty of the model parameters is quantified as a ratio of their minimum and maximum values giving the accurate fits. It is equivalent to the double uncertainty factor metrics discussed in [156].

Following the top-down approach, one should start the elucidation of ORR on CNTs considering the model (a), which consists of steps:



Here  $k_{1a/-1a}$   $\{\text{cm}^3 \text{ mol}^{-1} \text{ s}^{-1} / \text{s}^{-1}\}$  are forward/backward rate constants for  $O_2$  adsorption step (5.26) on the electrode surface,  $k_{2a/-2a}$   $\{\text{s}^{-1} / \text{s}^{-1}\}$  are forward/backward rate constants for  $O_2$  reduction to  $HO_2^-$  (5.27),  $\alpha_{2a}$   $\{1\}$  is cathodic charge transfer coefficient in (5.27), and  $k_{3a/-3a}$   $\{\text{s}^{-1} / \text{cm}^3 \text{ mol}^{-1} \text{ s}^{-1}\}$  are forward/backward rate constants for  $HO_2^-$  desorption step (5.28) from the electrode surface.

Note that (5.27) is not elementary, but an effective reaction step being composed of several elementary ones. Model (a) was chosen as it was successfully used to demonstrate synergistic effects between carbons and TMO catalysts [68], [79], [218]. The further

elucidation of the nature of the rate-determining step within the effective step (5.27) may be carried out using the formalism derived within the quasi-equilibrium approximation, which is described in [103]. However, additional model parameters should be introduced which makes the model more complicated.

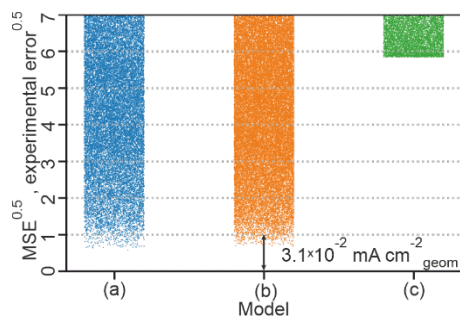


Figure 5.4 Square root of modeling errors in the optimization process for both ORR and HPRR/HPOR data. The detailed description of the models (a), (b), and (c) can be found in Scheme 1 and section 5.2.3. MSE is calculated according to (5.6). Experimental error is evaluated from (5.5). Each point in the histogram corresponds to the fitting error given by one particular set of model parameters. One unit of the y-axis corresponds to  $3.1 \times 10^{-2} \text{ mA cm}^{-2}_{\text{geom}}$  (per electrode geometric surface area).

The simulation shows (Figure 5.4) that the model (a) has sufficient accuracy to describe the full experimental data. The accuracy is provided by fitting errors lower than experimental ones on the available experimental dataset.

Model (a)

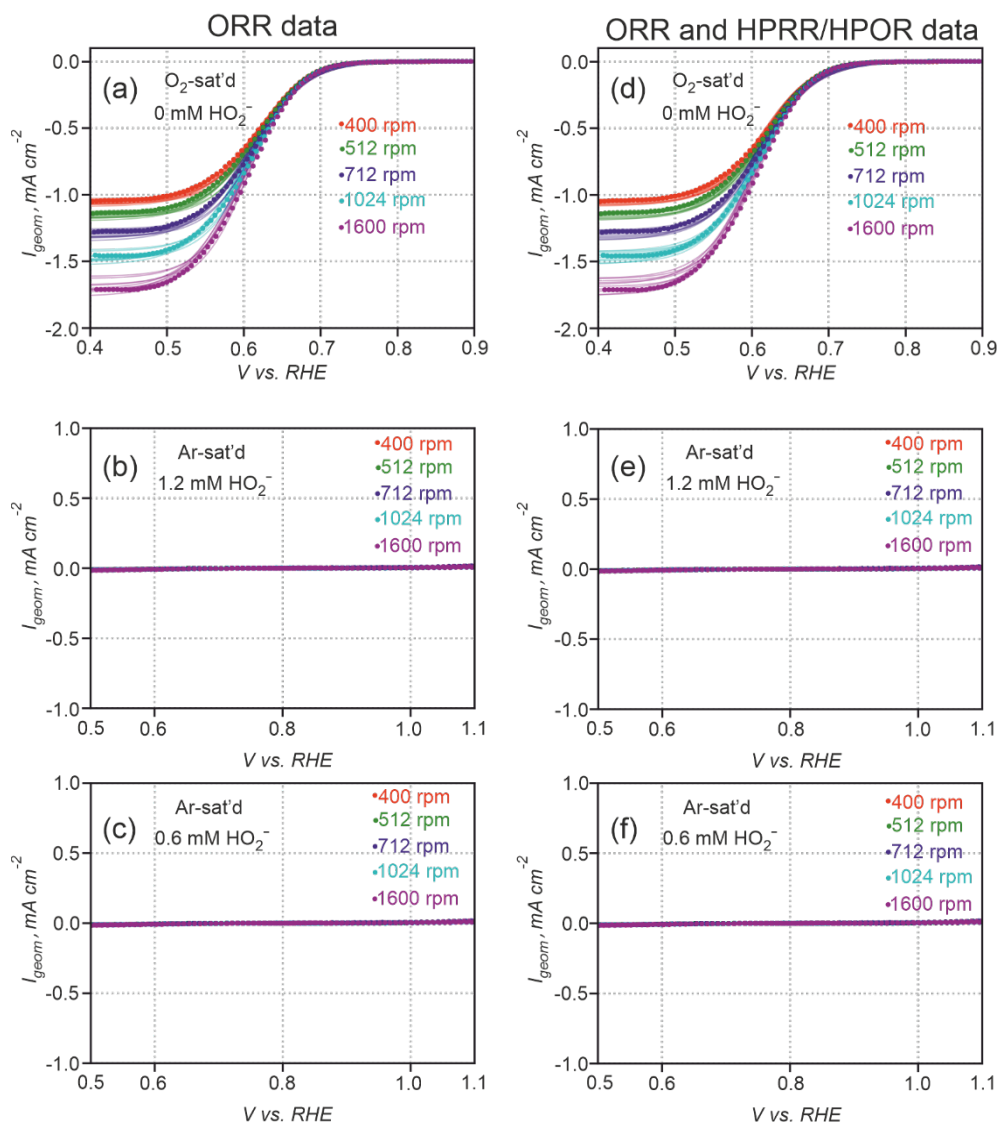


Figure 5.5 Example of modeling results for the model (a) with 3 reaction steps. All figures include the simulated RDE CVs for 10 random sets of model parameters with objective function lower than the experimental error (semi-transparent lines) and averaged experimental data (dots). Model parameters were adjusted by fitting of ORR RDE (a-c) and both ORR and HPRR/HPOR RDE (d-f) data. Simulated RDE CVs for O<sub>2</sub>-saturated solution (a, d), Ar-saturated solution with added 1.2 mM (b, e) and 0.6 mM (c, f) of hydroperoxide are shown.

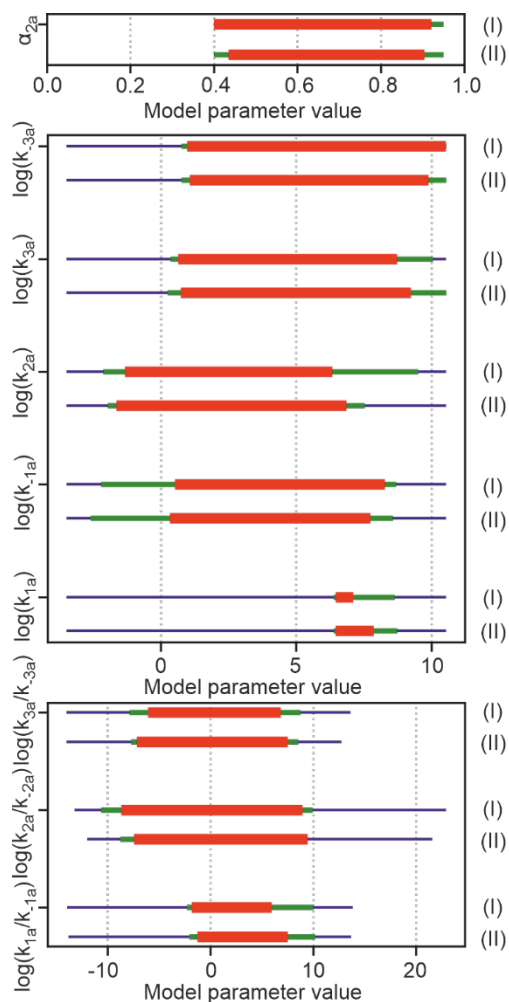


Figure 5.6 The intervals of the model (a) parameters. Blue line – overall optimization interval, green and red lines – minimal intervals within which all the values of parameters giving the fitting errors lower than four and one experimental errors calculated from (5.5) are contained. The experimental data of ORR RDE (I), ORR and HPRR/HPOR RDE (II) were fitted.

However, the range of the model (a) parameters, which gives accurate fit (Figure 5.5), is large for both fitting the ORR (Figure 5.6 (I)) and full HPRR/HPOR plus ORR (Figure 5.6 3(II)) data. It has more than seven orders of magnitude width for all rate constants except forward rate constant of O<sub>2</sub> adsorption, which varies less than 2 orders of magnitude. Such a high uncertainty in model parameters means that the model (a) is overcomplicated

being applied to available experimental data. One can solve this issue either by collecting more accurate and diverse experimental measurements (variation of pH, O<sub>2</sub> partial pressure, temperature, etc.) or by reducing the number of independent model parameters.

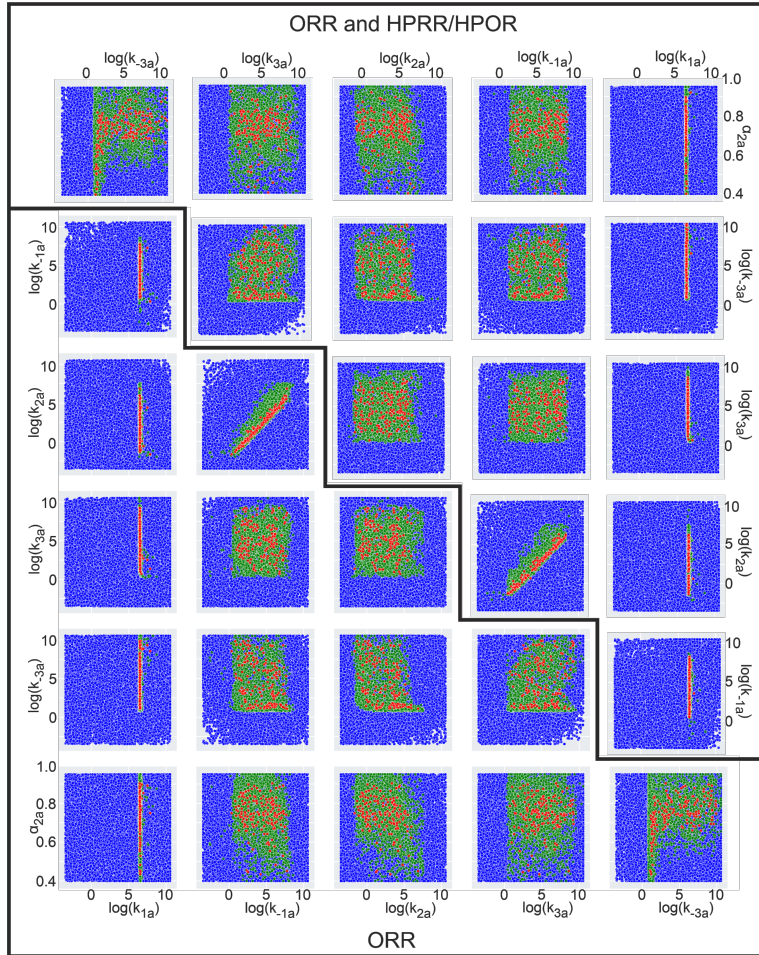


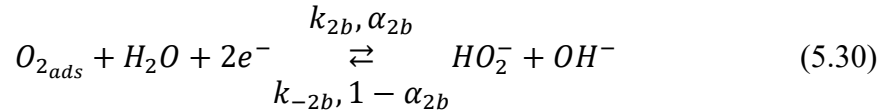
Figure 5.7 Pair distributions of independent model (a) parameters. The figures on the left lower and right upper parts correspond to the fitting of ORR only and all ORR plus HPRR/HPOR RDE CVs respectively. Dots represent sets of the model parameters, for which objective function was evaluated to be: lower than experimental error (red); between one and four experimental errors (green); higher than four experimental errors (blue).

The latter option can be implemented by identification of the lower number of descriptors (i.e. independent combinations of model parameters) within the same model.

The simple descriptors as the ratio of forward/backward rate constants for model (a) steps does not uniquely describe modeling results (Figure 5.6).

The exploration of the model parameters space with pairwise plots (Figure 5.7) reveals linear dependence for  $k_{-1a}$  and  $k_{2a}$  with the slope of 1.01 in log-log space and independency of  $k_{1a}$  from other model parameters. The estimated  $\log(k_{-1a}/k_{2a})$  varies in the range of [0.89, 2.83] for the accurate fitting of the complete dataset. Further elucidating other possible model descriptors cannot be provided by pairwise plots (Figure 5.7) and requires complicated dimensionality reduction techniques to be carried out. Hence one can claim that: (i) one cannot uniquely determine all rate constants from model (a) applied for our experimental dataset; (ii) simultaneous fitting of ORR and HPRR/HPOR does not reduce the uncertainty in estimated model parameters; (iii) only two descriptors in 6-dimensional model parameter space were found, namely  $k_{1a}$  and  $k_{-1a}/k_{2a}$ . So, model (a) is overcomplicated for the description of available experimental data and should be simplified. The step (5.26) should be upheld in the new model due to (iii).

The model (a) is simplified applying quasi-equilibrium and  $HO_2^-$  ads almost empty surface approximations to step (5.28) and merging steps (5.27), (5.28) into an effective one. It was done on the assumption that  $HO_2^-$  adsorption/desorption is fast under the experimental conditions and cannot be accessed on the complete ORR and HPOR/HPRR dataset. New model (b) proceeds through steps (5.29), (5.30):



Here  $k_{1b/-1b}$   $\{cm^3 mol^{-1} s^{-1} / s^{-1}\}$  are forward/backward rate constants for  $O_2$  adsorption step (5.29) on the electrode surface identical to (5.26),  $k_{2b/-2b}$   $\{s^{-1} / cm^3 mol^{-1} s^{-1}\}$  are forward/backward rate constants for  $O_2$  reduction to  $HO_2^-$  combined with its desorption from the surface (5.30),  $\alpha_{2b}$   $\{1\}$  is a cathodic charge transfer coefficient in (5.30). The rate

constants for the effective step (5.30) can still be potentially linked with molecular-level insights adopting the formalism from [103].

Model (b) provides sufficient accuracy to describe available experimental data (Figure 5.4). The examples of accurate fits are shown on (Figure 5.9).

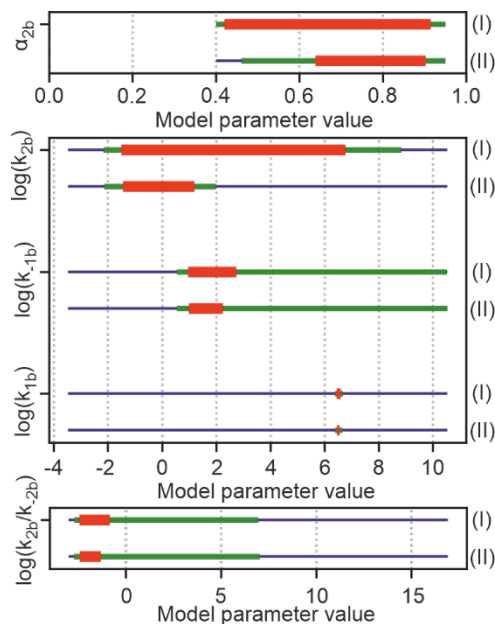


Figure 5.8 The intervals of model (b) parameters. Blue line – overall optimization interval, green and red lines – minimal intervals within which all the values of parameters giving the fitting errors lower than four and one experimental errors calculated from (5.5) are contained. The experimental data of ORR RDE (I), ORR and HPRR/HPOR RDE (II) were fitted.

Model (b)

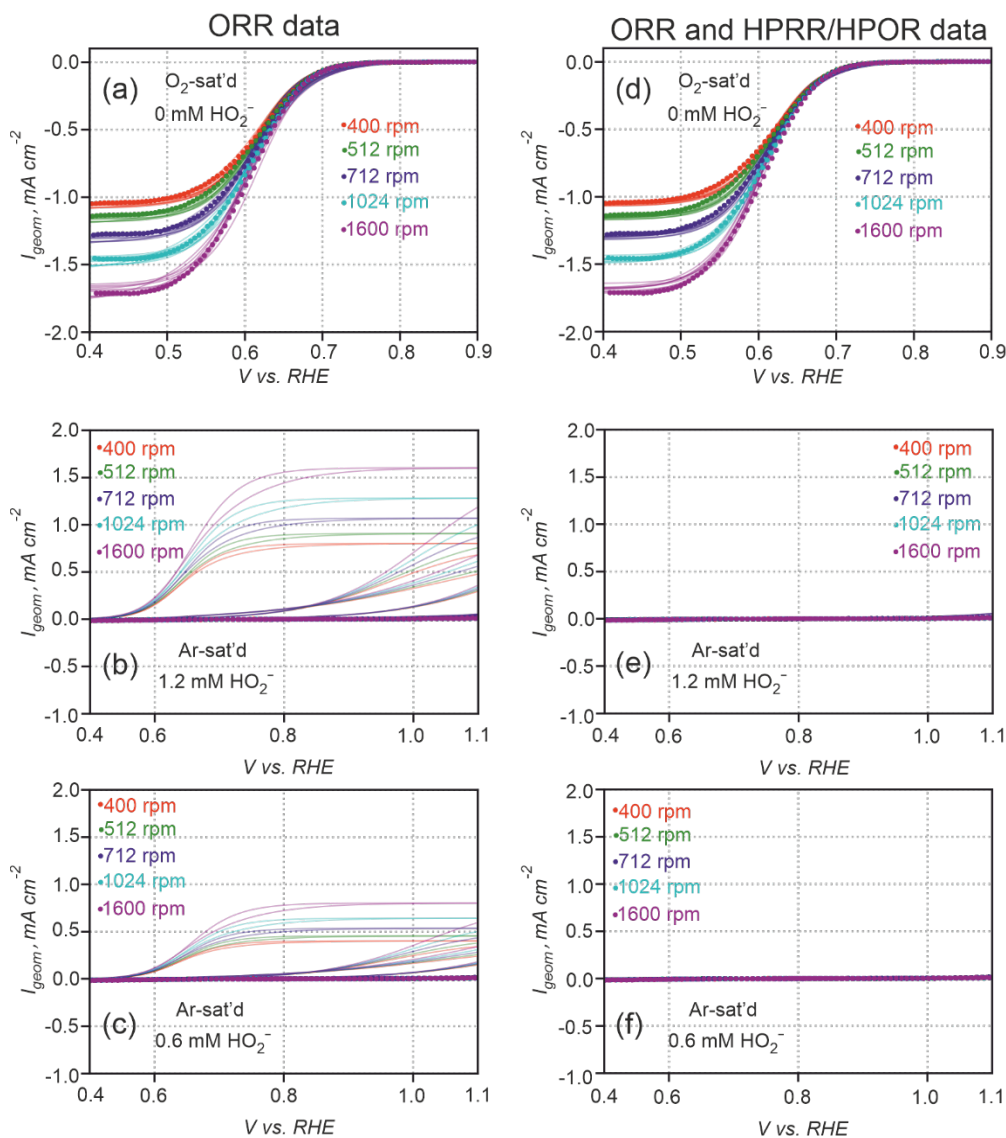


Figure 5.9 Example of modeling results for the model (b) with 2 steps. All figures include the simulated RDE CVs for 10 random sets of model parameters with objective function lower than the experimental error (semi-transparent lines) and averaged experimental data (dots). Model parameters were adjusted by fitting of ORR RDE (a-c) and both ORR and HPRR/HPOR RDE (d-f) data. Simulated RDE CVs for  $O_2$ -saturated solution (a, d), Ar-saturated solution with added  $1.2 \text{ mM}$  (b, e) and  $0.6 \text{ mM}$  (c, f) of hydroperoxide are shown.

For the model (b), the uncertainty of model parameters giving the accurate fit shows a strong dependence on the amount of experimental data (Figure 5.8). This result is the opposite of what was observed for the model (a). The uncertainty of the model parameters is quantified as the ratio of their maximum and minimum values giving the fits within the experimental error. The  $k_{1b}$  is accurately determined for both ORR and full ORR plus HPRR/HPOR data with uncertainties of 4.6 and 1.3 respectively. The  $k_{-1b}$  uncertainty is reduced from 62.5 to 17 by introducing the HPRR/HPOR data. It is still low corresponding to the 0.1 and 0.07 eV errors in activation barriers from TST at room temperature, which is well below 0.2 eV errors achievable in first-principles calculations [90].  $k_{2b}$  cannot be estimated even with the full experimental dataset, despite its uncertainty decreased from  $\sim 4.4 \times 10^5$  to  $4.3 \times 10^2$  switching from ORR to ORR plus HPRR/HPOR data. The simultaneous decrease in model parameters uncertainties can be explained as follows. One can see from the examples of accurate fits, that the model parameters obtained from only ORR fitting give non-negligible HPOR currents (Figure 5.9 (b), (c)) which is controversial to the experimental results. Obviously, the simultaneous fitting of ORR plus HPRR/HPOR experiments provides accurate fits for the complete dataset (Figure 5.9 (e), (f)). The  $k_{-2b}$ , which is governing the electrooxidation of hydroperoxide is calculated from model parameters to reproduce standard potential (2.7). So the values of model parameters are restricted to give  $k_{-2b}$  values, which provide negligible HPOR currents. The symmetry coefficient  $\alpha_{2b}$  can be estimated only for the full experimental dataset varying from 0.64 to 0.9.

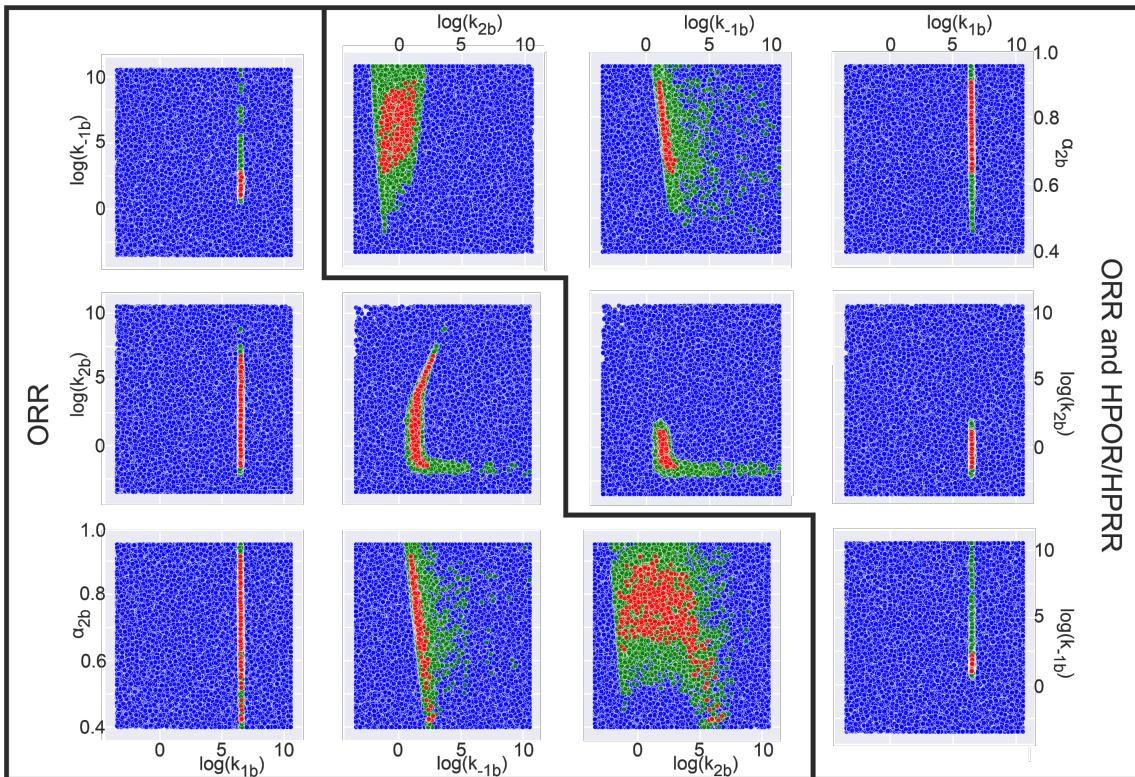


Figure 5.10 Pair distributions of independent model (b) parameters. The figures on the left lower and right upper parts correspond to the fitting of ORR only and all ORR plus HPOR/HPRR RDE CVs respectively. Dots represent sets of the model parameters, for which objective function was evaluated to be: lower than experimental error (red); between one and four experimental errors (green); higher than four experimental errors (blue). Experimental error is calculated using (5.5).

The elucidation of model parameters dependencies and model descriptors by pairwise plots (Figure 5.10) gives the following insights. Firstly,  $k_{1b}$  is independent of all other model parameters. Secondly, the  $\log(k_{-1b})$  reveals the linear dependence on  $\alpha_{2b}$  for both fitted datasets. As for the complete experimental dataset, the uncertainties of model parameters  $k_{-1b}$  and  $\alpha_{2b}$  are low, there is no need to introduce their combination as the model descriptor. Thirdly, one cannot elucidate the dependence of  $k_{2b}$  from other model parameters on the complete experimental dataset.

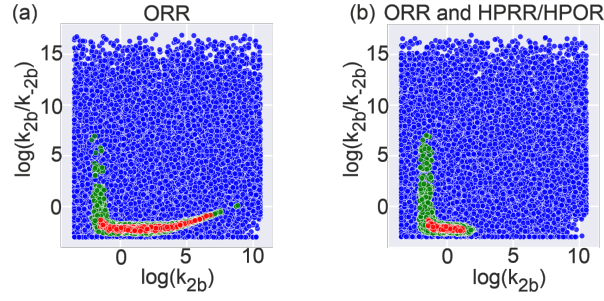
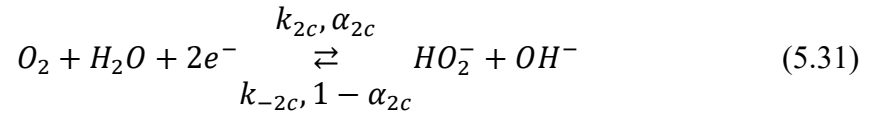


Figure 5.11 Pair distributions of model (b) parameters combination. Fitting was performed for ORR RDE (a) and both ORR plus HPR RDE (b) data. Dots represent sets of the model parameters, for which objective function was evaluated to be: lower than experimental error (red); between 1 and 4 experimental errors (green); higher than 4 experimental errors (blue).

However, one can also explore the dependence of  $k_{2b}$  and  $k_{-2b}$ . The latter one is not the independent model parameter as it was calculated from fitted model parameters to adjust standard potential (2.7). However, its combination with  $k_{2b}$  may be studied as a model descriptor. One can see from the pairwise plots (Figure 5.11) that  $k_{2b}/k_{-2b}$  has much lower uncertainties than  $k_{2b}$  equal to 40.3 and 12.8 for ORR and ORR plus HPRR/HPOR dataset, respectively. The uncertainties of  $k_{-2b}$  by itself are  $6.4 \times 10^7$  and  $5.2 \times 10^3$  respectively. Therefore, model (b) being applied for available experimental data provides uncertainties lower than achievable by *ab initio* methods [90] for the fitted model parameters with  $k_{2b}/k_{-2b}$  being used as model descriptor instead of fitted  $k_{2b}$ .

The further simplification of model (b) considering the quasi-equilibrium and  $O_{2ads}$  almost-empty surface approximations for (5.29) is leading to model (c):



Here  $k_{1c}/k_{-1c}$   $\{s^{-1}/cm^3 mol^{-1} s^{-1}\}$  are forward/backward rate constants for  $O_2$  reduction to  $HO_2^-$ ,  $\alpha_{1c}$   $\{1\}$  is cathodic charge transfer coefficient in (5.31).

Model (c)

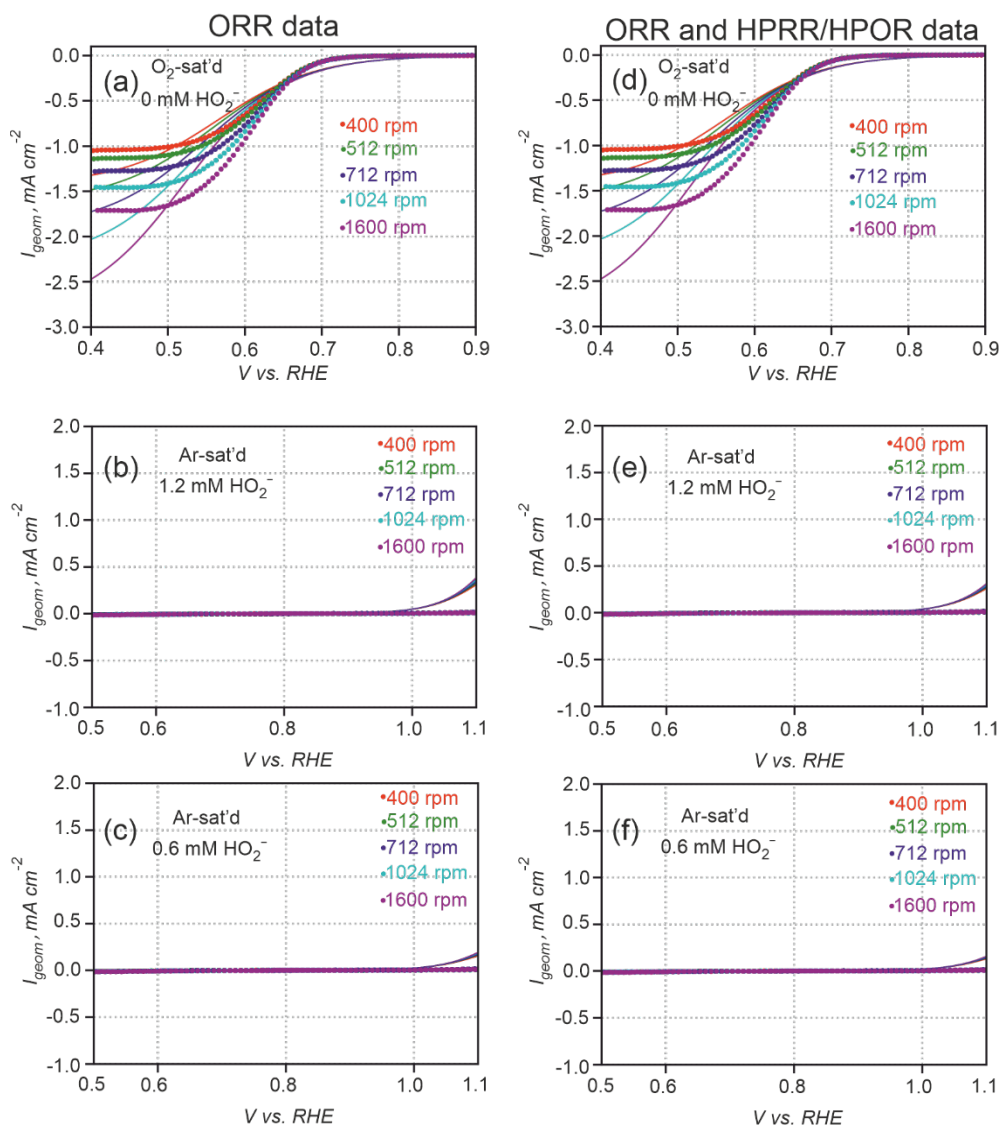


Figure 5.12 Example of modeling results for the model (c) with a single step. All figures include the simulated RDE CVs for 10 random sets of model parameters with objective function lower than the experimental error (semi-transparent lines) and averaged experimental data (dots). Model parameters were adjusted by fitting of ORR RDE (a-c) and both ORR and HPRR/HPOR RDE (d-f) data. Simulated RDE CVs for  $\text{O}_2$ -saturated solution (a, d), Ar-saturated solution with added 1.2 mM (b, e) and 0.6 mM (c, f) of hydroperoxide are shown.

O<sub>2</sub> adsorption/desorption step is fast with ORR and HPRR/HPOR undergoing at low surface coverages. This model does not provide an accurate fit for the available experimental data with MSEs for fitting being at least 25 times higher than the experimental MSEs (Figure 5.4). It is illustrated by the visualization of the most accurate fits within model (c). (Figure 5.12). Therefore, model (c) is too simple to describe the available experimental data for CNTs. The model (b) is the optimal one as it provides both accurate fits and low uncertainties of the model parameters. The elementary step detailing of ORR on CNTs cannot be achieved on the experimental data consisting of ORR and HPRR/HPOR RDEs in 0.1 M KOH. More detailed experiments such as ORR dependence on pH, T, and other data are needed which is the subject of a future study.

Based on the ORR on CNTs, the optimal model search methodology can be summarized as follows (Figure 5.13):

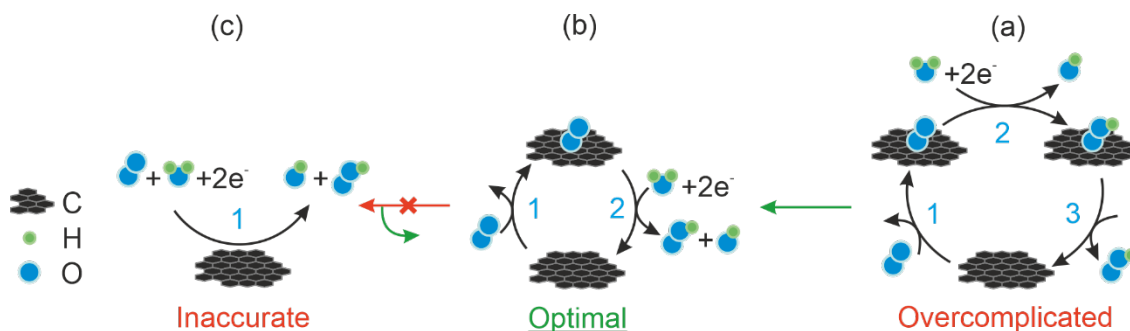


Figure 5.13 The framework of the optimal model selection for the ORR on CNTs.

- 1) Consider the initial model from literature (model (a) in this work).
- 2) Specify prior distributions for model parameters. In the bottom-up approach, they can be estimated from ab initio molecular-level insights. In the top-down approach, prior distributions should be set broad enough to explore possible reaction pathways within the same model.
- 3) If the model does not provide an accurate fit of all available experimental data, introduce a more advanced model (as for model (c) in this work).

- 4) If the model provides accurate fits for all experimental data, but the uncertainty of the model parameters and possible model descriptors is higher than the selected threshold value (for example, 20 in this work), consider model to be overcomplicated for available data and introduce simplified one (as for the model (a) in this work).
- 5) Iterate between steps 1 and 4, until the optimal model is found, for which uncertainty of model parameters or model descriptors is lower than threshold value, model provides accurate fit, more advanced model is overcomplicated, and simplified model is inaccurate.

#### 5.4. Conclusions

In this work, the quantitative framework of optimal model selection was demonstrated. It accounts for both accuracy of experimental results fitting by the suggested mean-field microkinetic model and the uncertainty in estimated model parameters with the latter one originating from the experimental errors. The utilized TPE algorithm for adaptive sampling of model parameters within the data collaboration approach enables error propagation through the estimated uncertainties and initial prior distributions for model parameters. The author believes that the quantitative treatment of experimental errors is of high importance for the successful application of a multiscale modeling approach to the study of complex heterogeneous reactions mechanisms. Despite that Pt-based and transition metal oxide catalyst systems require more complicated models with higher dimensionality of model parameters space, there is a big room for improvement by using adaptive sampling as part of the introduced framework, which should provide a more efficient way of uncertainties estimation even within the more advanced models.

When applied to the experimental dataset with ORR and HPRR/HPOR (varied  $\text{C}_{\text{HO}_2}$ ) RDE CVs on CNTs at different rotation rates, this approach demonstrates that the elementary step ORR mechanisms cannot be accessed based on the available experimental data. Even commonly used effective three-step mechanism provides large uncertainties in model parameters and should be simplified. The separate estimation of model parameters

with low uncertainties is possible only within the effective 2-step model with  $O_2$  adsorption/desorption and effective  $2e^- O_2/HO_2^-$  reduction/oxidation steps combined with  $HO_2^-$  adsorption/desorption on the full available experimental data. The developed framework guides our research towards the collection of a more diverse experimental base. As the approximate treatment was used for the effective  $2e^-$  step in order to reduce the number of model parameters, one can potentially access the higher detailing of the ORR mechanism by linking the simulated model with the elementary step mechanism within the reasonable approximations (e.g. RDS approximation). It should reduce the model form uncertainty by the cost of an acceptable number of additional model parameters. Moreover, it should improve the connection between the MF-MKM and *ab initio* simulations. I feel optimistic about accessing the elementary step mechanisms for CNTs based on the extended dataset with varied pH and  $P_{O_2}$  and higher precision of experimental measurements, which is a matter for further research. Together with the quantitative model selection approach, it should enable the quantitative selection of the ORR mechanism on more advanced transition metal oxide carbon composites currently being studied around the world.

## Chapter 6. Model Form Uncertainty Reduction Based on RDS Approximation for the Effective Multi-Electron Steps.

The work presented in this chapter aims to reduce the model form uncertainty for the ORR mechanism on CNTs addressed in previous chapter, by linking the microkinetic models including the effective multi-electron transfer steps with the one-electron step mechanism within the RDS approximation. The quantitative framework reported in the previous chapter was used for the reaction mechanism selection based on the accuracy of fitting with mean-field microkinetic models and parameter uncertainty quantification to determine how likely certain reaction steps occur if some aspects of the system are not exactly known.

### 6.1. Materials and methods

#### 6.1.1. Experimental data.

The data reported in Chapter 5 is used for the simulations. The CNTs sample is synthesized by C. T. Alexander. Briefly, the experimental dataset consists of RDE voltammograms at  $5 \text{ mV s}^{-1}$  scan rate for ORR and hydroperoxide oxidation/reduction reaction (HPRR/HPOR) in  $\text{O}_2$ -saturated and Ar-purged + 0.6; 1.2 mM  $\text{HO}_2^-$  0.1 M KOH respectively. CNTs mass loading was equal to  $51 \mu\text{g cm}^{-2}$  in all experiments,  $S_{\text{BET}} = 50.58 \text{ m}^2 \text{ g}^{-1}$ . Working electrode potential was recalculated vs. reversible hydrogen electrode (RHE) and iR-corrected with  $R=46 \Omega$ . The rotation rate was varied from 400 to 1600 rpm. Triplicate measurements were used to estimate the experimental uncertainty. The averaged voltammograms normalized by the geometric surface area of the electrode ( $0.196 \text{ cm}^2$ ) were fitted in simulations

### 6.1.2. Modeling details.

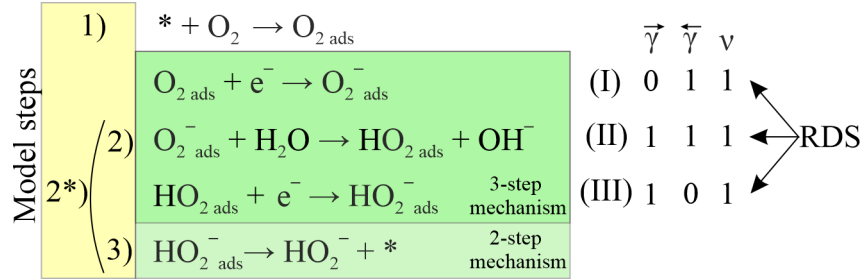


Figure 6.1 Effective model steps, ORR one-electron mechanism, RDS positions within the  $2e^- O_2/HO_2^-$  reduction step, and the values of the parameters, used to simulate the specified RDS within the model according to (6.1), (6.2).

The full experimental dataset was fitted simultaneously. The one-electron step ORR mechanism was adopted (see Figure 6.1). It was successfully used to simulate the ORR on carbon nanofibers [51]. Additionally, it explained Tafel slopes  $\sim -60\text{mV/dec}$  for ORR on CNTs at low overpotentials within the simplistic RDS approximation for the whole mechanism [121]. Two microkinetic models were simulated: 2-step model consisting of effective steps 1) and 2\*); 3-step model with the steps 1), 2), 3). (see Figure 6.1) Kinetic currents were extracted using the Koutecky-Levich equation.

The cathodic and anodic Tafel slopes are dependent on the position of RDS within the effective  $2e^-$  step. So the cathodic and anodic transfer coefficients were calculated in the model from RDS approximation of step 2) or 2\*) as follows [103]:

$$\tilde{\alpha} = \begin{cases} \frac{\vec{\gamma}}{v} + \alpha, & \text{RDS - electron transfer step} \\ \frac{\vec{\gamma}}{v}, & \text{RDS - chemical step} \end{cases} \quad (6.1)$$

$$1 - \tilde{\alpha} = \begin{cases} 1 + \frac{\vec{\gamma}}{v} - \alpha, & \text{RDS - electron transfer step} \\ \frac{\vec{\gamma}}{v}, & \text{RDS - chemical step} \end{cases} \quad (6.2)$$

Here,  $\vec{\gamma}/\hat{\gamma}$  is the number of one-electron steps before/after the RDS,  $v$  – number of RDS repetitions, and  $\alpha$  - cathodic symmetry factor of electron-transfer RDS. All other

parameters and procedures are the same as in previous work [234]. The experimental data uncertainty  $MSE_{exp}$  was calculated as the MSE for triplicate measurements. The fitting error  $MSE_{fit}$  was evaluated as MSE between the simulated and averaged experimental voltammograms. The inverse uncertainty propagation was quantified using the data collaboration approach [174], [235]. The Tree-Structured Parzen estimator [176] algorithm was used to estimate the lower bounds of model parameters uncertainties, which give the fitting errors within the threshold expressed in  $MSE_{exp}$  units. 50 runs were performed for the initial model parameters space and 10 for the reduced space, where the model uncertainty was  $< 8 MSE_{exp}$ .

## 6.2. Results and Discussion

One can see the estimated uncertainty of model parameters in Figure 6.2. The  $k_X$ ,  $k_{-X}$ , and  $\alpha_X$  are respectively forward, backward reaction rate constants, and symmetry coefficient in step  $X$  from the model ( $X = 1, 2, 2^*, 3$ ). Even the relatively low increase of threshold value  $MSE_{exp}$  raises the uncertainty in model parameters by several orders of magnitude. It confirms the ill-posed nature of this problem even for the simplified models. Therefore, uncertainty propagation treatment is crucial to make use of MF-MKM as the source of constraints for model parameters. Based on the full available experimental dataset only the 3-step reaction with (I) RDS was able to fit the experimental data with  $MSE_{fit} < MSE_{exp}$ . The high uncertainty in  $k_{-1}$  may require the search of the model descriptors (i.e. combination of the model parameters which govern the voltammogram shape and has low uncertainty).

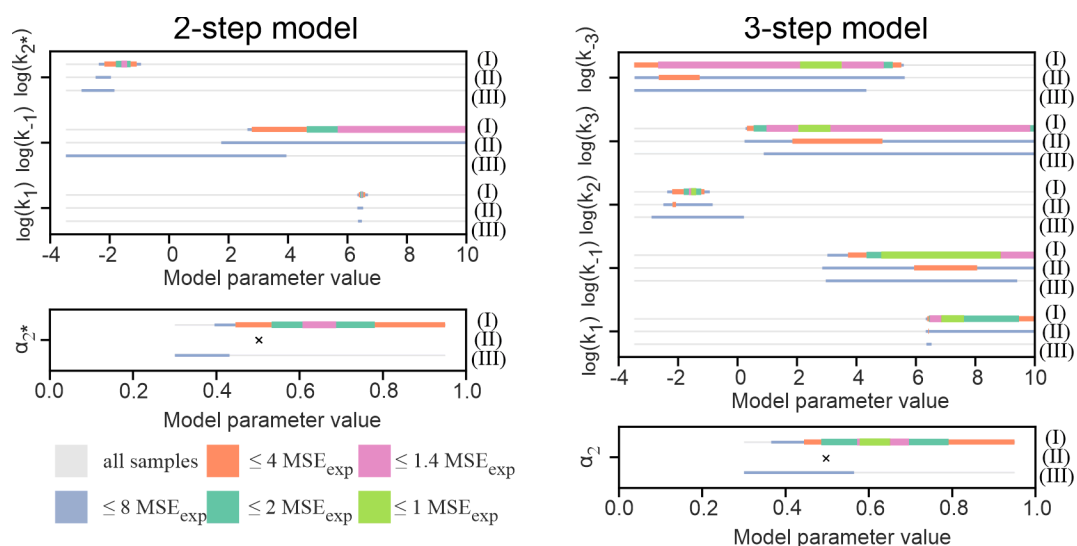


Figure 6.2. The lower bounds of the model parameters intervals in the 2-step and 3-step microkinetic models. Intervals with the specified colors contain all sets of the model parameters, which give  $MSE_{fit}$  lower than the corresponding threshold value.

The 2-step model with (I) RDS only reached the  $1.4 MSE_{exp}$  threshold, so it can be formally rejected using the criteria  $MSE_{fit} < MSE_{exp}$ . Models with (III) RDS should be rejected due to the high  $MSE_{fit}$  ( $> 4 MSE_{exp}$ ). Models with (II) RDS also inaccurately describe available data, although this approximation showed the observed Tafel slope of  $-60$  mV/dec and  $\infty$  at low and high overpotentials, respectively[121]. In order to understand this effect, one needs to analyze the fitting results of ORR voltammograms and extracted kinetic currents in the log scale.

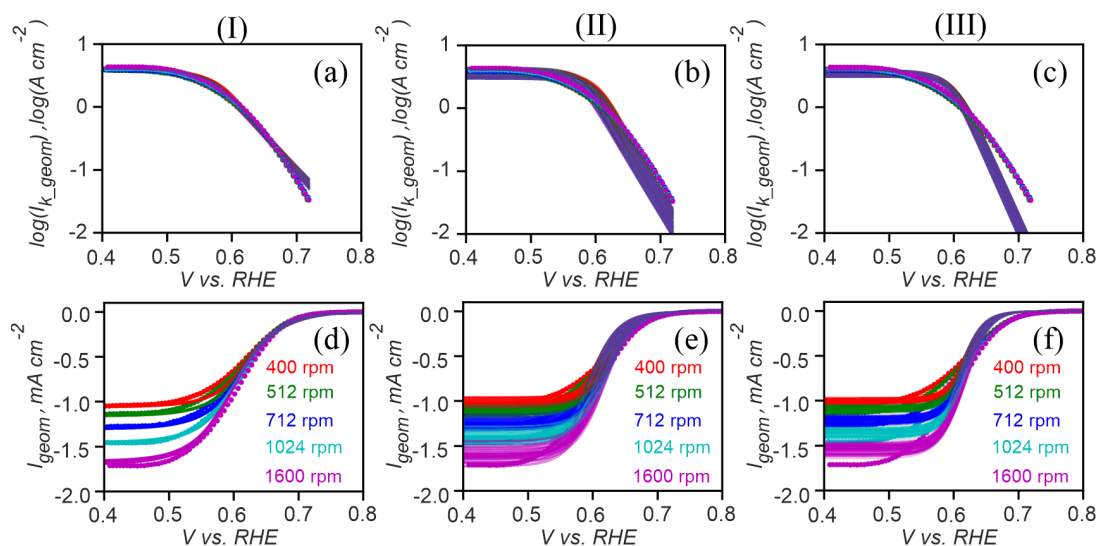


Figure 6.3. Modeling results for the 2-step microkinetic model for 3 possible RDS (I-III) positions within step 2\*). RDE CVs and extracted kinetic currents in log-scale are presented on figures (d-f) and (a-c) respectively. Numerical simulations and averaged experimental data are depicted as semi-transparent lines and dots. Modeling results are shown for 100 sets of model parameters giving the  $MSE_{fit}$  lower than the smallest available threshold value (see Figure 6.2).

Indeed, the  $MSE_{fit}$  is mostly sensitive to the potentials with moderate-high cathodic currents at potentials  $< 0.65$  V vs. RHE. They are attributed to the transition region  $-\infty$  -  $\infty$  mV/dec and region with  $\infty$  slope for log-kinetic currents (see Figure 6.3, Figure 6.4). The  $MSE_{fit}$  is not so sensitive to the slopes at low overpotentials. This leads to their deviations within the most accurate model fits with (II) RDS (Figure 6.3, Figure 6.4 (a)). The fitting procedure may be further improved by the use of better objective function than  $MSE_{fit}$  and corresponding thresholds  $MSE_{exp}$ . It should account for the importance of log-kinetic current slopes at low overpotentials for the deduction of the ORR mechanism. One could suggest the fitting in log-scale using the MSE as the objective function. This causes the undesirable omitting of the HPOR/HPRR data as their negligible currents at CNTs do not enable this kind of treatment. Alternatively, it could be used as the additional

constraints for ORR mechanism parameters by the use of appropriate objective function with experimental uncertainty treatment, which is the matter of further research.

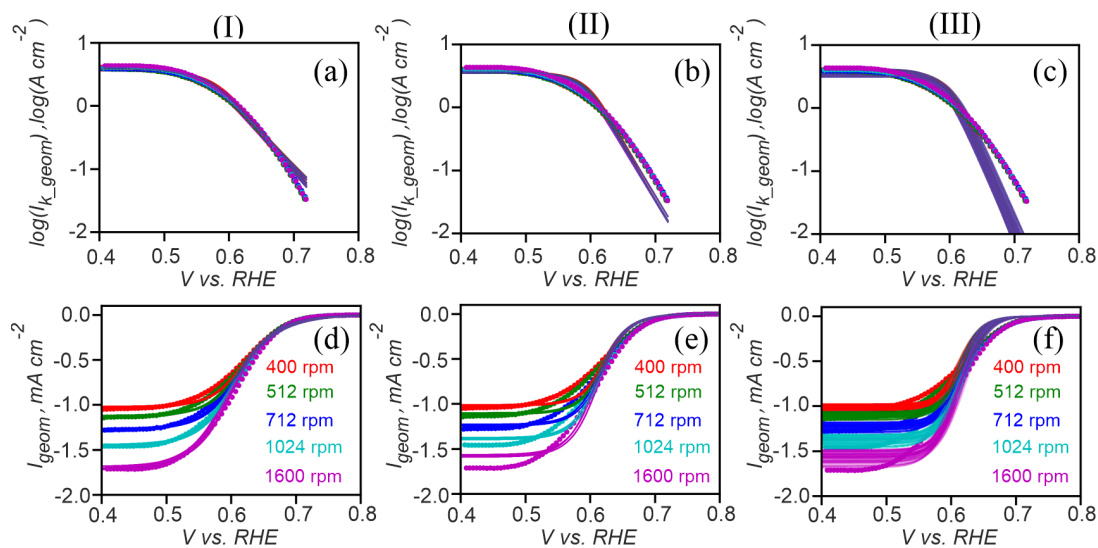


Figure 6.4. Modeling results for the 3-step microkinetic model for 3 possible RDS (I-III) positions within step 2). RDE CVs and extracted kinetic currents in log-scale are presented on figures (d-f) and (a-c) respectively. Numerical simulations and averaged experimental data are depicted as semi-transparent lines and dots. Modeling results are shown for 100 sets of model parameters giving the  $MSE_{fit}$  lower than the smallest available threshold value (see Figure 6.2).

Both models with (II) RDS correctly reproduce the  $-60$  mV/dec slope at low overpotentials (Figure 6.3, Figure 6.4 (b)). However, the transition region is poorly reproduced. Most probably, the direct modeling of the full one-electron mechanism will solve this issue by the cost of 6 additional model parameters, which is accessible by the current methods of inverse uncertainty propagation quantification within the kinetic models [156]. Higher dimensionality of model parameters space should bring significant uncertainty in the estimated model parameters due to the ill-posed nature of this problem. Therefore, only the existence possibility of this ORR mechanism on CNTs can be shown. The model with estimated model parameters will not be able to demonstrate predictive capability.

### 6.3. Conclusions

The model form uncertainty was decreased within the quantitative framework for reaction mechanism study as the models were linked with the one-electron ORR mechanism by RDS approximation. The importance of objective function was demonstrated for the experimental data fitting by the models. Despite the MSE of extracted kinetic currents in log scale may provide a better description of mechanistic features, it reduces the dataset size due to the low observed HPOR/HPRR currents. The predictive capability of the ORR mechanism with estimated model parameters can be enabled in two ways: i) Collection of the more detailed experimental dataset (e.g., accounting for T, pH, pO<sub>2</sub> variations). It is a matter of research to determine whether it is enough to precisely calculate the model parameters. However, their uncertainties should be gradually decreased making the results more reliable. The procedure of the optimal model selection is the same as described in a previous chapter. ii) Use of the estimated model parameters and their uncertainties within the multiscale modeling approach. They are additionally estimated from *ab initio* simulations. The latter ones should target the steps with the largest estimated uncertainty in model parameters. Therefore, the MF-MKM fitting provides additional constraints for the further mechanism study. The simultaneous treatment of model parameters uncertainties from two independent sources should help to elucidate the reaction mechanism thus decreasing the model form uncertainty.

## Chapter 7. Conclusions and Future Directions

The aim of the present thesis was to elucidate the ORR mechanism on the TMO/C catalysts in alkaline media for narrowing the process of their cost-effective search. This problem was accessed within the multiscale modeling approach.

The first attempt was dedicated to gaining mechanistic insights on ORR from the rationalization of the experimentally observed differences on the most ( $\text{Mn}_2\text{O}_3$ ) and the least ( $\text{MnOOH}$ ) active manganese oxides. It was shown that the *ab initio* thermodynamics approach based on periodic DFT calculations is not sufficient to explain the pronounced difference in observed HPRR currents and hydroperoxide yields. Instead, it provided the optimized surface active sites geometries, which were used to obtain the insights on the activation barriers of likely elementary steps within the cluster DFT calculations. The computed activation barriers ca. 2.5eV for  $\text{O}_2$  and  $\text{O}_2^-$  dissociative adsorption show that ORR is unlikely to proceed by the “direct”  $4e^-$  pathway on  $\text{Mn}_2\text{O}_3$ . The higher HPRR currents and the negligible  $\text{HO}_2^-$  yield on  $\text{Mn}_2\text{O}_3$  are explained by the ca. 0.3eV lower activation barrier for bond breaking in  $\text{HO}_2^-_{\text{ads}}$  intermediate due to adsorbate-adsorbate interactions at the  $\text{Mn}_2\text{O}_3$  surface. The estimated activation barriers for the first two ET steps in the outer-sphere regime, together with their modeling within the MF-MKM, do not contradict the available experimental data. The employed complementary computational methods with the experimental data cannot be used for quantitative discrimination of the possible ORR pathways, but rather suggest or question the existence of the alternative ones. Therefore, further improvement can be achieved only if the uncertainties arising from the accuracy of methods, corresponding approximations, and experimental data errors are quantified. It is necessary for the development of quantitative criteria for the rejection/acceptance of the ORR mechanisms and understanding, whether it is possible to distinguish them based on the state-of-the-art experimental/computational methods.

The experimental and MF-MKM components of the multiscale modeling approach for ORR were further addressed within the dual aim to elucidate the role of carbon as a co-catalyst supporting the LSCO materials, as well as to determine what minimal complexity of the microkinetic model (arising from the suggested ORR mechanism) is required to

describe all synergistic effects for ORR and HPRR/HPOR on TMO/C. The RDE experimental data of ORR and HPRR/HPOR on LSCO catalysts supported on either Vulcan carbon or 2 at. % N-doped carbon was used. The microkinetic model which is capable to qualitatively reproduce all the experimental data is unavoidably complicated. It was shown that only the reaction mechanism with 4-step ORR adopting a chemical step for  $\text{HO}_2^-$  decomposition on the perovskite surface, 3-step ORR on VC/NC,  $\text{HO}_2^-$  mass transfer between VC/NC and the perovskite, and  $\text{O}_2$  spillover between the NC and perovskite active sites, provided the qualitative reproduction for the ORR and HPRR/HPOR RDE experiments. Despite the simplified model for ORR and HPOR/HPRR on carbon and neglect of the adsorbate-adsorbate interactions, the modeling results show that the use of nitrogen-doped carbon support is leading to a 5-fold catalytic activity enhancement for ORR on LSCO/carbon composites through enhancement of the  $\text{O}_2$  spillover pathway. Indeed, these results rather provide the *ad hoc* mechanism, which should be further verified by the *ab initio* simulations. However, it is also valuable for understanding the unavoidable level of complexity, which is to be detailed in order to make predictive conclusions for the further catalyst search. Additionally, given the limited amount of the experimental data, further work is devoted to the elucidation of the constraints it can impose on the reaction mechanism and the corresponding model parameters. This goal can be achieved only when the experimental uncertainties and their propagation to the model parameters within MF-MKM are quantified. The experimentally accessible insights on the ORR mechanism can be then understood.

The simpler experimental system of ORR, HPOR/HPRR on CNTs was used to address this issue by developing the quantitative framework of optimal model selection from the available experimental data. It accounts for both accuracy of the experimental results fitting by the suggested mean-field microkinetic model and the uncertainty in estimated model parameters, with the latter one originating from the experimental errors. This approach demonstrates that the elementary step ORR mechanisms cannot be accessed based on the available experimental data (ORR and HPRR/HPOR (varied  $c_{\text{HO}_2^-}$ ) RDE CVs on CNTs at different rotation rates) on the simple experimental system. Even the commonly used

effective three-step mechanism provides large uncertainties in model parameters and should be simplified. The separate estimation of the model parameters with low uncertainties is possible only within the effective 2-step model with  $\text{O}_2$  adsorption/desorption and effective  $2e^- \text{O}_2/\text{HO}_2^-$  reduction/oxidation steps combined with  $\text{HO}_2^-$  adsorption/desorption on the full available experimental data. This framework can be utilized for two promising applications: (i) Guidance of the further experimental work based on the ORR mechanism detailing, which the collected experimental dataset provides. (ii) Enabling the quantitative treatment of uncertainty propagation within the multiscale modeling approach. The MF-MKM parameters are constrained by the experimental data. Their values and uncertainties are additionally estimated from *ab initio* simulations. The simultaneous treatment of the model parameters uncertainties from two independent sources helps to further elucidate the ORR mechanism, thus improving its predictive capability. The uncertainties of the parameters within MF-MKM are to be estimated from the intersection of the constraints on the model parameters obtained from both experiments and *ab initio* calculations and used as the quantitative criteria for the mechanism discrimination.

Finally, the uncertainty propagation from *ab initio* calculations was enabled by a more accurate description of effective multi-electron transfer steps within MF-MKM using the RDS approximation. It reduces the model form uncertainty by the cost of an acceptable number of additional model parameters. Therefore, the hierarchy of the considered MF-MKM models can be directly linked with the likely elementary-step models which are addressed by *ab initio* simulations. The microscale parameters (e.g. Gibbs free energy change for reaction steps) can be used to reduce the number of independent model parameters (e.g. through the equilibrium constants and their uncertainties). The importance of the objective function choice for the model discrimination was also demonstrated.

The obtained mechanistic insights for ORR on the TMO/C composite materials are in a good agreement with the reported literature data. Indeed, the probed inner-sphere mechanisms for ORR on  $\text{Mn}_2\text{O}_3$ ,  $\text{MnOOH}$ , and LSCO are excessively applied to explain the origins of the catalytic activity trends for the TMO materials [68], [72], [73], [199],

[226], [227]. The alternative outer-sphere ORR mechanism on  $\text{Mn}_2\text{O}_3$  and  $\text{MnOOH}$  is supported by the computational studies of ORR on Pt and Au in alkaline media [205], [206]. The concept of oxygen spillover is well known in literature for the composite catalytic materials [228], [236]. It worth noting that it calls for additional verification for LSCO/NC. The effective ORR mechanisms on CNTs, used to study the inverse uncertainty propagation, can be linked with the previously reported one-electron mechanisms [39], [51], [52] within the quasi-equilibrium and almost-empty surface approximations.

Summing up, a conclusive opinion about the ORR elementary-step mechanism on TMO/C catalysts still remains a matter of further research. It should be achieved by the iterative improvement of all components of the multiscale modeling approach. The extended experimental dataset together with the development of the more accurate physical description and numerical methods on both molecular and macroscale levels at some point should provide low uncertainty within the elementary step models. It worth noting that this work serves as the first step towards better coupling of the experiment and macroscale modeling through the quantitative inverse uncertainty propagation treatment. The additional efforts should be made to determine the ORR elementary-step mechanism on TMO/C. They include: (i) The accurate treatment of the solvent effects and charged surfaces by periodic DFT calculations (ii) The use of advanced methods for inverse uncertainty propagation quantification, which can deal with the increased dimensionality of the model parameters space for the elementary step models (iii) Collection of the more diverse experimental dataset, including the pH,  $p_{\text{O}_2}$ , T, and catalyst loading variations (iv) The use of the KMC simulations for the local coverage effects, which can be enabled by increased accuracy of *ab initio* calculations and the growth of computational resources.

## Bibliography

- [1] IEA, “Global Energy Review 2020,” 2020.
- [2] “Intergovernmental Panel on Climate Change. Global Warming of 1.5°C,” 2018.
- [3] IEA, “Tracking Transport,” Paris, 2019.
- [4] U. Lucia, “Overview on fuel cells,” *Renew. Sustain. Energy Rev.*, vol. 30, pp. 164–169, Feb. 2014, doi: 10.1016/j.rser.2013.09.025.
- [5] A. Simons and C. Bauer, “Life cycle assessment of hydrogen production,” in *Transition to Hydrogen*, no. January, A. Wokaun and E. Wilhelm, Eds. Cambridge: Cambridge University Press, 2011, pp. 13–57.
- [6] S. Liu, M. G. White, and P. Liu, “Mechanism of Oxygen Reduction Reaction on Pt(111) in Alkaline Solution: Importance of Chemisorbed Water on Surface,” *J. Phys. Chem. C*, vol. 120, no. 28, pp. 15288–15298, 2016, doi: 10.1021/acs.jpcc.6b05126.
- [7] X. Ge *et al.*, “Oxygen Reduction in Alkaline Media: From Mechanisms to Recent Advances of Catalysts,” *ACS Catal.*, vol. 5, no. 8, pp. 4643–4667, Aug. 2015, doi: 10.1021/acscatal.5b00524.
- [8] R. R. Adzic, *Recent advances in the kinetics of oxygen reduction*. New York: Wiley-VCH, 1998.
- [9] J. K. Nørskov *et al.*, “Origin of the Overpotential for Oxygen Reduction at a Fuel-Cell Cathode,” *J. Phys. Chem. B*, vol. 108, no. 46, pp. 17886–17892, Nov. 2004, doi: 10.1021/jp047349j.
- [10] J. Rossmeisl, Z.-W. Qu, H. Zhu, G.-J. Kroes, and J. K. Nørskov, “Electrolysis of water on oxide surfaces,” *J. Electroanal. Chem.*, vol. 607, no. 1–2, pp. 83–89, Sep. 2007, doi: 10.1016/j.jelechem.2006.11.008.
- [11] R. O’Hayre, S.-W. Cha, W. Colella, and F. B. Prinz, *Fuel Cell Fundamentals*. Hoboken, NJ, USA: John Wiley & Sons, Inc, 2016.
- [12] D. R. Dekel, “Review of cell performance in anion exchange membrane fuel cells,” *J. Power Sources*, vol. 375, pp. 158–169, 2018, doi: 10.1016/j.jpowsour.2017.07.117.

- [13] F. A. De Bruijn, V. A. T. Dam, and G. J. M. Janssen, "Review: Durability and degradation issues of PEM fuel cell components," *Fuel Cells*, vol. 8, no. 1, pp. 3–22, 2008, doi: 10.1002/face.200700053.
- [14] S. Gottesfeld *et al.*, "Anion exchange membrane fuel cells: Current status and remaining challenges," *J. Power Sources*, vol. 375, pp. 170–184, 2018, doi: 10.1016/j.jpowsour.2017.08.010.
- [15] H. A. Firouzjaie and W. E. Mustain, "Catalytic Advantages, Challenges, and Priorities in Alkaline Membrane Fuel Cells," *ACS Catal.*, vol. 10, no. 1, pp. 225–234, 2020, doi: 10.1021/acscatal.9b03892.
- [16] Y. Wang, D. Y. C. Leung, J. Xuan, and H. Wang, "A review on unitized regenerative fuel cell technologies, part-A: Unitized regenerative proton exchange membrane fuel cells," *Renew. Sustain. Energy Rev.*, vol. 65, pp. 961–977, 2016, doi: 10.1016/j.rser.2016.07.046.
- [17] Y. Wang, D. Y. C. Leung, J. Xuan, and H. Wang, "A review on unitized regenerative fuel cell technologies, part B: Unitized regenerative alkaline fuel cell, solid oxide fuel cell, and microfluidic fuel cell," *Renew. Sustain. Energy Rev.*, vol. 75, no. November, pp. 775–795, 2017, doi: 10.1016/j.rser.2016.11.054.
- [18] J. Christensen *et al.*, "A Critical Review of Li/Air Batteries," *J. Electrochem. Soc.*, vol. 159, no. 2, pp. R1–R30, 2011, doi: 10.1149/2.086202jes.
- [19] K. Kinoshita, "Carbon: electrochemical and physicochemical properties," 1988.
- [20] F. Jaouen and J.-P. Dodelet, "O<sub>2</sub> Reduction Mechanism on Non-Noble Metal Catalysts for PEM Fuel Cells. Part I: Experimental Rates of O<sub>2</sub> Electroreduction, H<sub>2</sub>O<sub>2</sub> Electroreduction, and H<sub>2</sub>O<sub>2</sub> Disproportionation," *J. Phys. Chem. C*, vol. 113, no. 34, pp. 15422–15432, Aug. 2009, doi: 10.1021/jp900837e.
- [21] A. Damjanovic, M. A. Genshaw, and J. O. Bockris, "The Role of Hydrogen Peroxide in Oxygen Reduction at Platinum in H<sub>2</sub>SO<sub>4</sub> Solution," *J. Electrochem. Soc.*, vol. 114, no. 5, p. 466, 1967, doi: 10.1149/1.2426629.
- [22] D. B. Sepa, M. V. Vojnovic, L. M. Vracar, and A. Damjanovic, "Different views regarding the kinetics and mechanisms of oxygen reduction at Pt and Pd electrodes,"

- Electrochim. Acta*, vol. 32, no. 1, pp. 129–134, Jan. 1987, doi: 10.1016/0013-4686(87)87021-4.
- [23] D. B. Sepa, M. V. Vojnovic, and A. Damjanovic, “Reaction intermediates as a controlling factor in the kinetics and mechanism of oxygen reduction at platinum electrodes,” *Electrochim. Acta*, vol. 26, no. 6, pp. 781–793, Jun. 1981, doi: 10.1016/0013-4686(81)90037-2.
- [24] M. Paucirova, D. M. Drazic, and A. Damjanovic, “The effect of surface coverage by adsorbed oxygen on the kinetics of oxygen reduction at oxide free platinum,” *Electrochim. Acta*, vol. 18, no. 12, pp. 945–951, Dec. 1973, doi: 10.1016/0013-4686(73)87026-4.
- [25] V. Jalan, “Importance of Interatomic Spacing in Catalytic Reduction of Oxygen in Phosphoric Acid,” *J. Electrochem. Soc.*, vol. 130, no. 11, p. 2299, 1983, doi: 10.1149/1.2119574.
- [26] A. A. Turovskii, R. V. Kucher, N. A. Turovskii, and V. V. Lobanov, “Quantum-chemical calculation of the gas-phase decomposition of H<sub>2</sub>O<sub>2</sub> and CH<sub>3</sub>OOCH<sub>3</sub>,” *Theor. Exp. Chem.*, vol. 12, no. 5, pp. 469–474, 1977, doi: 10.1007/BF00525169.
- [27] Q. He and S. Mukerjee, “Electrocatalysis of oxygen reduction on carbon-supported PtCo catalysts prepared by water-in-oil micro-emulsion,” *Electrochim. Acta*, vol. 55, no. 5, pp. 1709–1719, 2010, doi: 10.1016/j.electacta.2009.10.054.
- [28] J. X. Wang *et al.*, “Oxygen Reduction on Well-Defined Core–Shell Nanocatalysts: Particle Size, Facet, and Pt Shell Thickness Effects,” *J. Am. Chem. Soc.*, vol. 131, no. 47, pp. 17298–17302, Dec. 2009, doi: 10.1021/ja9067645.
- [29] S. Chen and A. Kucernak, “Electrocatalysis under Conditions of High Mass Transport: Investigation of Hydrogen Oxidation on Single Submicron Pt Particles Supported on Carbon,” *J. Phys. Chem. B*, vol. 108, no. 37, pp. 13984–13994, Sep. 2004, doi: 10.1021/jp048641u.
- [30] R. W. Lindström *et al.*, “Electrocatalysis and transport effects on nanostructured Pt/GC electrodes,” *J. Electroanal. Chem.*, vol. 644, no. 2, pp. 90–102, Jun. 2010, doi: 10.1016/j.jelechem.2009.04.034.

- [31] Y. E. Seidel, A. Schneider, Z. Jusys, B. Wickman, B. Kasemo, and R. J. Behm, “Mesoscopic mass transport effects in electrocatalytic processes,” *Faraday Discuss.*, vol. 140, pp. 167–184, 2009, doi: 10.1039/B806437G.
- [32] A. Schneider *et al.*, “Transport effects in the oxygen reduction reaction on nanostructured, planar glassy carbon supported Pt/GC model electrodes,” *Phys. Chem. Chem. Phys.*, vol. 10, no. 14, p. 1931, 2008, doi: 10.1039/b719775f.
- [33] E. Yeager, “Dioxygen electrocatalysis: mechanisms in relation to catalyst structure,” *J. Mol. Catal.*, vol. 38, no. 1–2, pp. 5–25, Nov. 1986, doi: 10.1016/0304-5102(86)87045-6.
- [34] A. Damjanovic and V. Brusic, “Electrode kinetics of oxygen reduction on oxide-free platinum electrodes,” *Electrochim. Acta*, vol. 12, no. 6, pp. 615–628, Jun. 1967, doi: 10.1016/0013-4686(67)85030-8.
- [35] R. R. Adžić and J. X. Wang, “Configuration and Site of O<sub>2</sub> Adsorption on the Pt(111) Electrode Surface,” *J. Phys. Chem. B*, vol. 102, no. 45, pp. 8988–8993, Nov. 1998, doi: 10.1021/jp981057z.
- [36] P. S. Ruvinskiy, A. Bonnefont, and E. R. Savinova, “Further Insight into the Oxygen Reduction Reaction on Pt Nanoparticles Supported on Spatially Structured Catalytic Layers,” *Electrocatalysis*, vol. 2, no. 2, pp. 123–133, Jun. 2011, doi: 10.1007/s12678-011-0046-1.
- [37] P. S. Ruvinskiy, A. Bonnefont, C. Pham-Huu, and E. R. Savinova, “Using Ordered Carbon Nanomaterials for Shedding Light on the Mechanism of the Cathodic Oxygen Reduction Reaction,” *Langmuir*, vol. 27, no. 14, pp. 9018–9027, Jul. 2011, doi: 10.1021/la2006343.
- [38] F. Cheng and J. Chen, “Metal–air batteries: from oxygen reduction electrochemistry to cathode catalysts,” *Chem. Soc. Rev.*, vol. 41, no. 6, p. 2172, 2012, doi: 10.1039/c1cs15228a.
- [39] I. Morcos and E. Yeager, “Kinetic studies of the oxygen—peroxide couple on pyrolytic graphite,” *Electrochim. Acta*, vol. 15, no. 6, pp. 953–975, Jun. 1970, doi: 10.1016/0013-4686(70)80037-8.

- [40] D. T. Sawyer and E. T. Seo, "One-electron mechanism for the electrochemical reduction of molecular oxygen," *Inorg. Chem.*, vol. 16, no. 2, pp. 499–501, Feb. 1977, doi: 10.1021/ic50168a059.
- [41] E. Yeager, "Electrocatalysts for O<sub>2</sub> reduction," *Electrochim. Acta*, vol. 29, no. 11, pp. 1527–1537, Nov. 1984, doi: 10.1016/0013-4686(84)85006-9.
- [42] A. J. Appleby and J. Marie, "Kinetics of oxygen reduction on carbon materials in alkaline solution," *Electrochim. Acta*, vol. 24, no. 2, pp. 195–202, Feb. 1979, doi: 10.1016/0013-4686(79)80024-9.
- [43] K. Vaik, "Electrochemical reduction of oxygen on anodically pre-treated and chemically grafted glassy carbon electrodes in alkaline solutions," *Electrochem. commun.*, vol. 6, no. 1, pp. 1–5, Jan. 2004, doi: 10.1016/j.elecom.2003.10.003.
- [44] J. Xu, W. Huang, and R. L. McCreery, "Isotope and surface preparation effects on alkaline dioxygen reduction at carbon electrodes," *J. Electroanal. Chem.*, vol. 410, no. 2, pp. 235–242, Jul. 1996, doi: 10.1016/0022-0728(96)04545-7.
- [45] R. J. Taylor and A. A. Humffray, "Electrochemical studies on glassy carbon electrodes," *J. Electroanal. Chem. Interfacial Electrochem.*, vol. 64, no. 1, pp. 63–84, Sep. 1975, doi: 10.1016/S0022-0728(75)80278-6.
- [46] M. Appel and A. J. Appleby, "A ring-disk electrode study of the reduction of oxygen on active carbon in alkaline solution," *Electrochim. Acta*, vol. 23, no. 11, pp. 1243–1246, Nov. 1978, doi: 10.1016/0013-4686(78)85080-4.
- [47] A. J. Appleby and M. Savy, "Kinetics of oxygen reduction reactions involving catalytic decomposition of hydrogen peroxide. Application to porous and rotating ring-disk electrodes," *J. Electroanal. Chem.*, vol. 92, no. 1, pp. 15–30, 1978, doi: 10.1016/S0022-0728(78)80113-2.
- [48] J. Mrha, "Study of catalysts for fuel cell electrodes. IV. Active carbon electrodes for oxygen in alkaline electrolyte," *Collect. Czechoslov. Chem. Commun.*, vol. 32, no. 2, pp. 708–719, 1967, doi: 10.1135/cccc19670708.
- [49] H.-H. Yang and R. L. McCreery, "Elucidation of the Mechanism of Dioxygen Reduction on Metal-Free Carbon Electrodes," *J. Electrochem. Soc.*, vol. 147, no. 9,

- p. 3420, 2000, doi: 10.1149/1.1393915.
- [50] B. H. J. Bielski and A. O. Allen, "Mechanism of the disproportionation of superoxide radicals," *J. Phys. Chem.*, vol. 81, no. 11, pp. 1048–1050, Jun. 1977, doi: 10.1021/j100526a005.
- [51] S. Maldonado and K. J. Stevenson, "Influence of Nitrogen Doping on Oxygen Reduction Electrocatalysis at Carbon Nanofiber Electrodes," *J. Phys. Chem. B*, vol. 109, no. 10, pp. 4707–4716, Mar. 2005, doi: 10.1021/jp044442z.
- [52] J. D. Wiggins-Camacho and K. J. Stevenson, "Mechanistic Discussion of the Oxygen Reduction Reaction at Nitrogen-Doped Carbon Nanotubes," *J. Phys. Chem. C*, vol. 115, no. 40, pp. 20002–20010, Oct. 2011, doi: 10.1021/jp205336w.
- [53] C. T. Alexander, A. M. Abakumov, R. P. Forslund, K. P. Johnston, and K. J. Stevenson, "Role of the Carbon Support on the Oxygen Reduction and Evolution Activities in LaNiO<sub>3</sub> Composite Electrodes in Alkaline Solution," *ACS Appl. Energy Mater.*, vol. 1, no. 4, pp. 1549–1558, Apr. 2018, doi: 10.1021/acsaem.7b00339.
- [54] H. Bin Yang *et al.*, "Identification of catalytic sites for oxygen reduction and oxygen evolution in N-doped graphene materials: Development of highly efficient metal-free bifunctional electrocatalyst," *Sci. Adv.*, vol. 2, no. 4, pp. 1–12, 2016, doi: 10.1126/sciadv.1501122.
- [55] Z. Luo *et al.*, "Pyridinic N doped graphene: synthesis, electronic structure, and electrocatalytic property," *J. Mater. Chem.*, vol. 21, no. 22, p. 8038, 2011, doi: 10.1039/c1jm10845j.
- [56] A. Damjanovic, M. A. Genshaw, and J. O. Bockris, "The Mechanism of Oxygen Reduction at Platinum in Alkaline Solutions with Special Reference to H<sub>2</sub>O<sub>2</sub>," *J. Electrochem. Soc.*, vol. 114, no. 11, p. 1107, 1967, doi: 10.1149/1.2426425.
- [57] D. B. Sepa, M. V. Vojnovic, and A. Damjanovic, "Kinetics and mechanism of O<sub>2</sub> reduction at Pt in alkaline solutions," *Electrochim. Acta*, vol. 25, no. 11, pp. 1491–1496, Nov. 1980, doi: 10.1016/0013-4686(80)87167-2.

- [58] N. M. Marković, H. A. Gasteiger, and P. N. Ross, "Oxygen Reduction on Platinum Low-Index Single-Crystal Surfaces in Alkaline Solution: Rotating Ring Disk Pt( hkl ) Studies," *J. Phys. Chem.*, vol. 100, no. 16, pp. 6715–6721, Apr. 1996, doi: 10.1021/jp9533382.
- [59] N. A. Anastasijević, V. Vesović, and R. R. Adžić, "Determination of the kinetic parameters of the oxygen reduction reaction using the rotating ring-disk electrode. Part II. Applications," *J. Electroanal. Chem.*, vol. 229, no. 1–2, pp. 317–325, 1987, doi: 10.1016/0022-0728(87)85149-5.
- [60] A. Bonnefont *et al.*, "Challenges in the understanding oxygen reduction electrocatalysis on transition metal oxides," *Curr. Opin. Electrochem.*, vol. 14, pp. 23–31, Apr. 2019, doi: 10.1016/j.coelec.2018.09.010.
- [61] A. S. Ryabova *et al.*, "Further insights into the role of carbon in manganese oxide/carbon composites in the oxygen reduction reaction in alkaline media," *Electrochim. Acta*, vol. 246, pp. 643–653, Aug. 2017, doi: 10.1016/j.electacta.2017.06.017.
- [62] S. Bag, K. Roy, C. S. Gopinath, and C. R. Raj, "Facile Single-Step Synthesis of Nitrogen-Doped Reduced Graphene Oxide-Mn<sub>3</sub>O<sub>4</sub> Hybrid Functional Material for the Electrocatalytic Reduction of Oxygen," *ACS Appl. Mater. Interfaces*, vol. 6, no. 4, pp. 2692–2699, Feb. 2014, doi: 10.1021/am405213z.
- [63] Y. Su *et al.*, "Enriched graphitic N-doped carbon-supported Fe<sub>3</sub>O<sub>4</sub> nanoparticles as efficient electrocatalysts for oxygen reduction reaction," *J. Mater. Chem. A*, vol. 2, no. 20, pp. 7281–7287, 2014, doi: 10.1039/C4TA00029C.
- [64] Y. Liang *et al.*, "Co<sub>3</sub>O<sub>4</sub> nanocrystals on graphene as a synergistic catalyst for oxygen reduction reaction," *Nat. Mater.*, vol. 10, no. 10, pp. 780–786, Oct. 2011, doi: 10.1038/nmat3087.
- [65] Y. Liang *et al.*, "Covalent Hybrid of Spinel Manganese–Cobalt Oxide and Graphene as Advanced Oxygen Reduction Electrocatalysts," *J. Am. Chem. Soc.*, vol. 134, no. 7, pp. 3517–3523, Feb. 2012, doi: 10.1021/ja210924t.
- [66] M. De Koninck and B. Marsan, "M<sub>n</sub>xCu<sub>1-x</sub>Co<sub>2</sub>O<sub>4</sub> used as bifunctional

- electrocatalyst in alkaline medium,” *Electrochim. Acta*, vol. 53, no. 23, pp. 7012–7021, Oct. 2008, doi: 10.1016/j.electacta.2008.02.002.
- [67] T. Hyodo, M. Hayashi, N. Miura, and N. Yamazoe, “Catalytic Activities of Rare-Earth Manganites for Cathodic Reduction of Oxygen in Alkaline Solution,” *J. Electrochem. Soc.*, vol. 143, no. 11, pp. L266–L267, Nov. 1996, doi: 10.1149/1.1837229.
- [68] T. Poux, A. Bonnefont, G. Kéranguéven, G. A. Tsirlina, and E. R. Savinova, “Electrocatalytic Oxygen Reduction Reaction on Perovskite Oxides: Series versus Direct Pathway,” *ChemPhysChem*, vol. 15, no. 10, pp. 2108–2120, Jul. 2014, doi: 10.1002/cphc.201402022.
- [69] K. A. Stoerzinger, W. Lü, C. Li, Ariando, T. Venkatesan, and Y. Shao-Horn, “Highly Active Epitaxial  $\text{La}(1-x)\text{Sr}_x\text{MnO}_3$  Surfaces for the Oxygen Reduction Reaction: Role of Charge Transfer,” *J. Phys. Chem. Lett.*, vol. 6, no. 8, pp. 1435–1440, Apr. 2015, doi: 10.1021/acs.jpcclett.5b00439.
- [70] D. Thiele and A. Züttel, “Electrochemical characterisation of air electrodes based on  $\text{La}_{0.6}\text{Sr}_{0.4}\text{CoO}_3$  and carbon nanotubes,” *J. Power Sources*, vol. 183, no. 2, pp. 590–594, Sep. 2008, doi: 10.1016/j.jpowsour.2008.05.042.
- [71] J. Sunarso, A. A. J. Torriero, W. Zhou, P. C. Howlett, and M. Forsyth, “Oxygen Reduction Reaction Activity of La-Based Perovskite Oxides in Alkaline Medium: A Thin-Film Rotating Ring-Disk Electrode Study,” *J. Phys. Chem. C*, vol. 116, no. 9, pp. 5827–5834, Mar. 2012, doi: 10.1021/jp211946n.
- [72] J. Suntivich, H. A. Gasteiger, N. Yabuuchi, H. Nakanishi, J. B. Goodenough, and Y. Shao-Horn, “Design principles for oxygen-reduction activity on perovskite oxide catalysts for fuel cells and metal–air batteries,” *Nat. Chem.*, vol. 3, no. 7, pp. 546–550, Jul. 2011, doi: 10.1038/nchem.1069.
- [73] T. Poux, A. Bonnefont, A. Ryabova, G. Kéranguéven, G. A. Tsirlina, and E. R. Savinova, “Electrocatalysis of hydrogen peroxide reactions on perovskite oxides: experiment versus kinetic modeling,” *Phys. Chem. Chem. Phys.*, vol. 16, no. 27, pp. 13595–13600, 2014, doi: 10.1039/C4CP00341A.

- [74] K. A. Stoerzinger, M. Risch, B. Han, and Y. Shao-Horn, "Recent Insights into Manganese Oxides in Catalyzing Oxygen Reduction Kinetics," *ACS Catal.*, vol. 5, no. 10, pp. 6021–6031, Oct. 2015, doi: 10.1021/acscatal.5b01444.
- [75] M. Risch *et al.*, "Redox Processes of Manganese Oxide in Catalyzing Oxygen Evolution and Reduction: An in Situ Soft X-ray Absorption Spectroscopy Study," *J. Phys. Chem. C*, vol. 121, no. 33, pp. 17682–17692, Aug. 2017, doi: 10.1021/acs.jpcc.7b05592.
- [76] F. H. B. Lima, M. L. Calegario, and E. A. Ticianelli, "Electrocatalytic activity of manganese oxides prepared by thermal decomposition for oxygen reduction," *Electrochim. Acta*, vol. 52, no. 11, pp. 3732–3738, Mar. 2007, doi: 10.1016/j.electacta.2006.10.047.
- [77] L. Mao, D. Zhang, T. Sotomura, K. Nakatsu, N. Koshiba, and T. Oshaka, "Mechanistic study of the reduction of oxygen in air electrode with manganese oxides as electrocatalysts," *Electrochim. Acta*, vol. 48, no. 8, pp. 1015–1021, Apr. 2003, doi: 10.1016/S0013-4686(02)00815-0.
- [78] F. Cheng, Y. Su, J. Liang, Z. Tao, and J. Chen, "MnO<sub>2</sub> -Based Nanostructures as Catalysts for Electrochemical Oxygen Reduction in Alkaline Media †," *Chem. Mater.*, vol. 22, no. 3, pp. 898–905, Feb. 2010, doi: 10.1021/cm901698s.
- [79] A. S. Ryabova *et al.*, "Rationalizing the Influence of the Mn(IV)/Mn(III) Red-Ox Transition on the Electrocatalytic Activity of Manganese Oxides in the Oxygen Reduction Reaction," *Electrochim. Acta*, vol. 187, no. Iv, pp. 161–172, Jan. 2016, doi: 10.1016/j.electacta.2015.11.012.
- [80] J. B. Goodenough and B. L. Cushing, *Handbook of Fuel Cells - Fundamentals, Technology and Applications 2*. Wiley, 2003.
- [81] T. Poux, "Study of the oxygen reduction on perovskite-type oxides in alkaline media," *PhD Thesis*, 2014.
- [82] T. Poux *et al.*, "Dual role of carbon in the catalytic layers of perovskite/carbon composites for the electrocatalytic oxygen reduction reaction," *Catal. Today*, vol. 189, no. 1, pp. 83–92, Jul. 2012, doi: 10.1016/j.cattod.2012.04.046.

- [83] A. J. Bard, L. R. Faulkner, J. Leddy, and C. G. Zoski, *Electrochemical methods: fundamentals and applications*, vol. 2. Wiley New York, 1980.
- [84] W. T. Hong, M. Risch, K. A. Stoerzinger, A. Grimaud, J. Suntivich, and Y. Shao-Horn, "Toward the rational design of non-precious transition metal oxides for oxygen electrocatalysis," *Energy Environ. Sci.*, vol. 8, no. 5, pp. 1404–1427, 2015, doi: 10.1039/C4EE03869J.
- [85] A. G. Oshchepkov *et al.*, "Exploring the Influence of the Nickel Oxide Species on the Kinetics of Hydrogen Electrode Reactions in Alkaline Media," *Top. Catal.*, vol. 59, no. 15–16, pp. 1319–1331, Sep. 2016, doi: 10.1007/s11244-016-0657-0.
- [86] S. Rangarajan, C. T. Maravelias, and M. Mavrikakis, "Sequential-Optimization-Based Framework for Robust Modeling and Design of Heterogeneous Catalytic Systems," *J. Phys. Chem. C*, vol. 121, no. 46, pp. 25847–25863, Nov. 2017, doi: 10.1021/acs.jpcc.7b08089.
- [87] J. K. Nørskov, T. Bligaard, J. Rossmeisl, and C. H. Christensen, "Towards the computational design of solid catalysts," *Nat. Chem.*, vol. 1, no. 1, pp. 37–46, Apr. 2009, doi: 10.1038/nchem.121.
- [88] A. A. Gokhale, S. Kandoi, J. P. Greeley, M. Mavrikakis, and J. A. Dumesic, "Molecular-level descriptions of surface chemistry in kinetic models using density functional theory," *Chem. Eng. Sci.*, vol. 59, no. 22–23, pp. 4679–4691, Nov. 2004, doi: 10.1016/j.ces.2004.09.038.
- [89] J. K. Nørskov, F. Abild-Pedersen, F. Studt, and T. Bligaard, "Density functional theory in surface chemistry and catalysis," *Proc. Natl. Acad. Sci.*, vol. 108, no. 3, pp. 937–943, Jan. 2011, doi: 10.1073/pnas.1006652108.
- [90] S. Matera, W. F. Schneider, A. Heyden, and A. Savara, "Progress in Accurate Chemical Kinetic Modeling, Simulations, and Parameter Estimation for Heterogeneous Catalysis," *ACS Catal.*, vol. 9, no. 8, pp. 6624–6647, Aug. 2019, doi: 10.1021/acscatal.9b01234.
- [91] H. Prats, F. Illas, and R. Sayós, "General concepts, assumptions, drawbacks, and misuses in kinetic Monte Carlo and microkinetic modeling simulations applied to

- computational heterogeneous catalysis,” *Int. J. Quantum Chem.*, vol. 118, no. 9, p. e25518, May 2018, doi: 10.1002/qua.25518.
- [92] B. Han, V. Viswanathan, and H. Pitsch, “First-Principles Based Analysis of the Electrocatalytic Activity of the Unreconstructed Pt(100) Surface for Oxygen Reduction Reaction,” *J. Phys. Chem. C*, vol. 116, no. 10, pp. 6174–6183, Mar. 2012, doi: 10.1021/jp2075379.
- [93] P. Christopher, “Surface-Mediated Processes for Energy Production and Conversion: Critical Considerations in Model System Design for DFT Calculations,” *ACS Energy Lett.*, vol. 3, no. 12, pp. 3015–3016, Dec. 2018, doi: 10.1021/acsenerylett.8b02213.
- [94] G. N. Simm, A. C. Vaucher, and M. Reiher, “Exploration of Reaction Pathways and Chemical Transformation Networks,” *J. Phys. Chem. A*, vol. 123, no. 2, pp. 385–399, 2019, doi: 10.1021/acs.jpca.8b10007.
- [95] O. Deutschmann, *Modeling and Simulation of Heterogeneous Catalytic Reactions*. Weinheim, Germany: Wiley-VCH Verlag GmbH & Co. KGaA, 2011.
- [96] H. Jacobsen, “A failure of DFT is not necessarily a DFT failure-performance dependencies on model system choices,” *J. Chem. Theory Comput.*, vol. 7, no. 9, pp. 3019–3025, 2011, doi: 10.1021/ct200476u.
- [97] S. Raimondeau and D. . Vlachos, “Recent developments on multiscale, hierarchical modeling of chemical reactors,” *Chem. Eng. J.*, vol. 90, no. 1–2, pp. 3–23, Nov. 2002, doi: 10.1016/S1385-8947(02)00065-7.
- [98] S. Matera *et al.*, “Evidence for the Active Phase of Heterogeneous Catalysts through In Situ Reaction Product Imaging and Multiscale Modeling,” *ACS Catal.*, vol. 5, no. 8, pp. 4514–4518, Aug. 2015, doi: 10.1021/acscatal.5b00858.
- [99] R. J. Baxter and P. Hu, “Insight into why the Langmuir–Hinshelwood mechanism is generally preferred,” *J. Chem. Phys.*, vol. 116, no. 11, pp. 4379–4381, Mar. 2002, doi: 10.1063/1.1458938.
- [100] V. G. Levich, *Physicochemical hydrodynamics*. Englewood Cliffs, N. J.: Prentice Hall, Scripta Technica, Inc., 1962.

- [101] L. Ma, D. B. Ingham, M. Pourkashanian, and E. Carcadea, "Review of the Computational Fluid Dynamics Modeling of Fuel Cells," *J. Fuel Cell Sci. Technol.*, vol. 2, no. 4, pp. 246–257, Nov. 2005, doi: 10.1115/1.2039958.
- [102] P. Stoltze, "Microkinetic simulation of catalytic reactions," *Prog. Surf. Sci.*, vol. 65, no. 3–4, pp. 65–150, Oct. 2000, doi: 10.1016/S0079-6816(00)00019-8.
- [103] J. O. Bockris, A. K. N. Reddy, and M. E. Gamboa-Aldeco, *Modern Electrochemistry 2A Fundamentals of Electrodics*, 2nd ed., vol. 2. New York: Kluwer Academic Publishers, 2002.
- [104] M. T. M. Koper and J. H. Sluyters, "Electrochemical oscillators: their description through a mathematical model," *J. Electroanal. Chem. Interfacial Electrochem.*, vol. 303, no. 1–2, pp. 73–94, Mar. 1991, doi: 10.1016/0022-0728(91)85117-8.
- [105] P. Stoltze and J. K. Nørskov, "Bridging the 'Pressure Gap' between Ultrahigh-Vacuum Surface Physics and High-Pressure Catalysis," *Phys. Rev. Lett.*, vol. 55, no. 22, pp. 2502–2505, Nov. 1985, doi: 10.1103/PhysRevLett.55.2502.
- [106] J. K. Nørskov and P. Stoltze, "Theoretical aspects of surface reactions," *Surf. Sci.*, vol. 189–190, no. C, pp. 91–105, Oct. 1987, doi: 10.1016/S0039-6028(87)80419-3.
- [107] P. Stoltze, "An interpretation of the high-pressure kinetics of ammonia synthesis based on a microscopic model," *J. Catal.*, vol. 110, no. 1, pp. 1–10, Mar. 1988, doi: 10.1016/0021-9517(88)90291-6.
- [108] P. Stoltze and J. K. Nørskov, "A description of the high-pressure ammonia synthesis reaction based on surface science," *J. Vac. Sci. Technol. A Vacuum, Surfaces, Film.*, vol. 5, no. 4, pp. 581–585, Jul. 1987, doi: 10.1116/1.574677.
- [109] C. V. Ovesen, P. Stoltze, J. K. Nørskov, and C. T. Campbell, "A kinetic model of the water gas shift reaction," *J. Catal.*, vol. 134, no. 2, pp. 445–468, Apr. 1992, doi: 10.1016/0021-9517(92)90334-E.
- [110] C. Stegelmann and P. Stoltze, "Microkinetic analysis of the oxygen–silver system," *Surf. Sci.*, vol. 552, no. 1–3, pp. 260–272, Mar. 2004, doi: 10.1016/j.susc.2004.01.028.
- [111] C. Stegelmann, N. C. Schiødt, C. T. Campbell, and P. Stoltze, "Microkinetic

- modeling of ethylene oxidation over silver,” *J. Catal.*, vol. 221, no. 2, pp. 630–649, Jan. 2004, doi: 10.1016/j.jcat.2003.10.004.
- [112] J. A. Dumesic *et al.*, “A kinetic modeling approach to the design of catalysts: formulation of a catalyst design advisory program,” *Ind. Eng. Chem. Res.*, vol. 26, no. 7, pp. 1399–1407, Jul. 1987, doi: 10.1021/ie00067a022.
- [113] R. D. Cortright, R. M. Watwe, B. E. Spiewak, and J. A. Dumesic, “Kinetics of ethane hydrogenolysis over supported platinum catalysts,” *Catal. Today*, vol. 53, no. 3, pp. 395–406, Nov. 1999, doi: 10.1016/S0920-5861(99)00133-9.
- [114] M. D. Amiridis, J. E. Rekoske, J. A. Dumesic, D. F. Rudd, N. D. Spencer, and C. J. Pereira, “Simulation of methane partial oxidation over silica-supported MoO<sub>3</sub> and V<sub>2</sub>O<sub>5</sub>,” *AIChE J.*, vol. 37, no. 1, pp. 87–97, Jan. 1991, doi: 10.1002/aic.690370108.
- [115] A. A. Gokhale, J. A. Dumesic, and M. Mavrikakis, “On the mechanism of low-temperature water gas shift reaction on copper,” *J. Am. Chem. Soc.*, vol. 130, no. 4, pp. 1402–1414, 2008, doi: 10.1021/ja0768237.
- [116] A. J. Medford *et al.*, “Thermochemistry and micro-kinetic analysis of methanol synthesis on ZnO (0 0 0 1),” *J. Catal.*, vol. 309, pp. 397–407, 2014, doi: 10.1016/j.jcat.2013.10.015.
- [117] R. J. Madon, D. Braden, S. Kandoi, P. Nagel, M. Mavrikakis, and J. A. Dumesic, “Microkinetic analysis and mechanism of the water gas shift reaction over copper catalysts,” *J. Catal.*, vol. 281, no. 1, pp. 1–11, Jul. 2011, doi: 10.1016/j.jcat.2011.03.008.
- [118] F. Jaouen, “O<sub>2</sub> Reduction Mechanism on Non-Noble Metal Catalysts for PEM Fuel Cells. Part II: A Porous-Electrode Model To Predict the Quantity of H<sub>2</sub>O<sub>2</sub> Detected by Rotating Ring-Disk Electrode,” *J. Phys. Chem. C*, vol. 113, no. 34, pp. 15433–15443, Aug. 2009, doi: 10.1021/jp900838x.
- [119] C. F. Dickens, C. Kirk, and J. K. Nørskov, “Insights into the Electrochemical Oxygen Evolution Reaction with ab Initio Calculations and Microkinetic Modeling: Beyond the Limiting Potential Volcano,” *J. Phys. Chem. C*, vol. 123, no. 31, pp. 18960–18977, Aug. 2019, doi: 10.1021/acs.jpcc.9b03830.

- [120] H. A. Hansen, V. Viswanathan, and J. K. Nørskov, “Unifying kinetic and thermodynamic analysis of 2 e<sup>-</sup> and 4 e<sup>-</sup> reduction of oxygen on metal surfaces,” *J. Phys. Chem. C*, vol. 118, no. 13, pp. 6706–6718, 2014, doi: 10.1021/jp4100608.
- [121] T. Shinagawa, A. T. Garcia-Esparza, and K. Takanebe, “Insight on Tafel slopes from a microkinetic analysis of aqueous electrocatalysis for energy conversion,” *Sci. Rep.*, vol. 5, no. May, pp. 1–21, 2015, doi: 10.1038/srep13801.
- [122] J. T. Mefford, Z. Zhao, M. Bajdich, and W. C. Chueh, “Interpreting Tafel behavior of consecutive electrochemical reactions through combined thermodynamic and steady state microkinetic approaches,” *Energy Environ. Sci.*, vol. 13, no. 2, pp. 622–634, 2020, doi: 10.1039/c9ee02697e.
- [123] P. S. Ruvinskiy, A. Bonnefont, and E. R. Savinova, “3D-ordered layers of vertically aligned carbon nanofilaments as a model approach to study electrocatalysis on nanomaterials,” *Electrochim. Acta*, vol. 84, pp. 174–186, Dec. 2012, doi: 10.1016/j.electacta.2012.03.134.
- [124] Zinola and C. Fernando, *Electrocatalysis: Computational, Experimental, and Industrial Aspects*. Boca Raton: CRC Press, 2010.
- [125] M. Born and R. Oppenheimer, “Zur Quantentheorie der Molekeln,” *Ann. Phys.*, vol. 389, no. 20, pp. 457–484, 1927, doi: 10.1002/andp.19273892002.
- [126] P. Hohenberg and W. Kohn, “Inhomogeneous Electron Gas,” *Phys. Rev.*, vol. 136, no. 3B, pp. B864–B871, Nov. 1964, doi: 10.1103/PhysRev.136.B864.
- [127] W. Kohn and L. J. Sham, “Self-Consistent Equations Including Exchange and Correlation Effects,” *Phys. Rev.*, vol. 140, no. 4A, pp. A1133–A1138, Nov. 1965, doi: 10.1103/PhysRev.140.A1133.
- [128] D. Vanderbilt, “Soft self-consistent pseudopotentials in a generalized eigenvalue formalism,” *Phys. Rev. B*, vol. 41, no. 11, pp. 7892–7895, Apr. 1990, doi: 10.1103/PhysRevB.41.7892.
- [129] G. Kresse and D. Joubert, “From ultrasoft pseudopotentials to the projector augmented-wave method,” *Phys. Rev. B*, vol. 59, no. 3, pp. 1758–1775, Jan. 1999, doi: 10.1103/PhysRevB.59.1758.

- [130] D. R. Hamann, M. Schlüter, and C. Chiang, “Norm-Conserving Pseudopotentials,” *Phys. Rev. Lett.*, vol. 43, no. 20, pp. 1494–1497, Nov. 1979, doi: 10.1103/PhysRevLett.43.1494.
- [131] R. Car and M. Parrinello, “Unified Approach for Molecular Dynamics and Density-Functional Theory,” *Phys. Rev. Lett.*, vol. 55, no. 22, pp. 2471–2474, Nov. 1985, doi: 10.1103/PhysRevLett.55.2471.
- [132] J. P. Perdew and Y. Wang, “Accurate and simple analytic representation of the electron-gas correlation energy,” *Phys. Rev. B*, vol. 45, no. 23, pp. 13244–13249, Jun. 1992, doi: 10.1103/PhysRevB.45.13244.
- [133] J. P. Perdew, K. Burke, and M. Ernzerhof, “Generalized Gradient Approximation Made Simple,” *Phys. Rev. Lett.*, vol. 77, no. 18, pp. 3865–3868, Oct. 1996, doi: 10.1103/PhysRevLett.77.3865.
- [134] B. Hammer, L. B. Hansen, and J. K. Nørskov, “Improved adsorption energetics within density-functional theory using revised Perdew-Burke-Ernzerhof functionals,” *Phys. Rev. B*, vol. 59, no. 11, pp. 7413–7421, Mar. 1999, doi: 10.1103/PhysRevB.59.7413.
- [135] M. T. M. Koper, “Theory of multiple proton-electron transfer reactions and its implications for electrocatalysis,” *Chem. Sci.*, vol. 4, no. 7, pp. 2710–2723, 2013, doi: 10.1039/c3sc50205h.
- [136] H. A. Hansen, J. Rossmeisl, and J. K. Nørskov, “Surface Pourbaix diagrams and oxygen reduction activity of Pt, Ag and Ni(111) surfaces studied by DFT,” *Phys. Chem. Chem. Phys.*, vol. 10, no. 25, p. 3722, 2008, doi: 10.1039/b803956a.
- [137] A. Michaelides, A. Alavi, and D. A. King, “Different Surface Chemistries of Water on Ru{0001}: From Monomer Adsorption to Partially Dissociated Bilayers,” *J. Am. Chem. Soc.*, vol. 125, no. 9, pp. 2746–2755, Mar. 2003, doi: 10.1021/ja028855u.
- [138] V. Tripković, E. Skúlason, S. Siahrostami, J. K. Nørskov, and J. Rossmeisl, “The oxygen reduction reaction mechanism on Pt(111) from density functional theory calculations,” *Electrochim. Acta*, vol. 55, no. 27, pp. 7975–7981, Nov. 2010, doi: 10.1016/j.electacta.2010.02.056.

- [139] J. Rossmeisl, J. K. Nørskov, C. D. Taylor, M. J. Janik, and M. Neurock, “Calculated Phase Diagrams for the Electrochemical Oxidation and Reduction of Water over Pt(111),” *J. Phys. Chem. B*, vol. 110, no. 43, pp. 21833–21839, Nov. 2006, doi: 10.1021/jp0631735.
- [140] M. T. M. Koper, “Blank voltammetry of hexagonal surfaces of Pt-group metal electrodes: Comparison to density functional theory calculations and ultra-high vacuum experiments on water dissociation,” *Electrochim. Acta*, vol. 56, no. 28, pp. 10645–10651, Dec. 2011, doi: 10.1016/j.electacta.2011.02.001.
- [141] T. Bligaard, J. K. Nørskov, S. Dahl, J. Matthiesen, C. H. Christensen, and J. Sehested, “The Brønsted–Evans–Polanyi relation and the volcano curve in heterogeneous catalysis,” *J. Catal.*, vol. 224, no. 1, pp. 206–217, May 2004, doi: 10.1016/j.jcat.2004.02.034.
- [142] B. Hammer and J. K. Nørskov, “Theoretical surface science and catalysis—calculations and concepts,” in *Advances in Catalysis*, vol. 45, 2000, pp. 71–129.
- [143] Y. Matsumoto, H. Yoneyama, and H. Tamura, “Influence of the nature of the conduction band of transition metal oxides on catalytic activity for oxygen reduction,” *J. Electroanal. Chem. Interfacial Electrochem.*, vol. 83, no. 2, pp. 237–243, Oct. 1977, doi: 10.1016/S0022-0728(77)80169-1.
- [144] M. Otani and O. Sugino, “First-principles calculations of charged surfaces and interfaces: A plane-wave nonrepeated slab approach,” *Phys. Rev. B*, vol. 73, no. 11, p. 115407, Mar. 2006, doi: 10.1103/PhysRevB.73.115407.
- [145] O. Sugino, I. Hamada, M. Otani, Y. Morikawa, T. Ikeshoji, and Y. Okamoto, “First-principles molecular dynamics simulation of biased electrode/solution interface,” *Surf. Sci.*, vol. 601, no. 22, pp. 5237–5240, Nov. 2007, doi: 10.1016/j.susc.2007.04.208.
- [146] S. Schnur and A. Groß, “Challenges in the first-principles description of reactions in electrocatalysis,” *Catal. Today*, vol. 165, no. 1, pp. 129–137, May 2011, doi: 10.1016/j.cattod.2010.11.071.
- [147] C. D. Taylor, S. A. Wasileski, J. S. Filhol, and M. Neurock, “First principles reaction

- modeling of the electrochemical interface: Consideration and calculation of a tunable surface potential from atomic and electronic structure,” *Phys. Rev. B - Condens. Matter Mater. Phys.*, vol. 73, no. 16, pp. 1–16, 2006, doi: 10.1103/PhysRevB.73.165402.
- [148] K. Chan and J. K. Nørskov, “Electrochemical Barriers Made Simple,” *J. Phys. Chem. Lett.*, vol. 6, no. 14, pp. 2663–2668, Jul. 2015, doi: 10.1021/acs.jpcllett.5b01043.
- [149] J. Rossmeisl, E. Skúlason, M. E. Björketun, V. Tripkovic, and J. K. Nørskov, “Modeling the electrified solid–liquid interface,” *Chem. Phys. Lett.*, vol. 466, no. 1–3, pp. 68–71, Nov. 2008, doi: 10.1016/j.cplett.2008.10.024.
- [150] J. A. Gauthier *et al.*, “Challenges in Modeling Electrochemical Reaction Energetics with Polarizable Continuum Models,” *ACS Catal.*, vol. 9, no. 2, pp. 920–931, 2019, doi: 10.1021/acscatal.8b02793.
- [151] Z. Da He, S. Hanselman, Y. X. Chen, M. T. M. Koper, and F. Calle-Vallejo, “Importance of Solvation for the Accurate Prediction of Oxygen Reduction Activities of Pt-Based Electrocatalysts,” *J. Phys. Chem. Lett.*, vol. 8, no. 10, pp. 2243–2246, 2017, doi: 10.1021/acs.jpcllett.7b01018.
- [152] J. J. Mortensen, K. Kaasbjerg, S. L. Frederiksen, J. K. Nørskov, J. P. Sethna, and K. W. Jacobsen, “Bayesian error estimation in density-functional theory,” *Phys. Rev. Lett.*, vol. 95, no. 21, pp. 1–5, 2005, doi: 10.1103/PhysRevLett.95.216401.
- [153] L. G. V. Briquet, M. Sarwar, J. Mugo, G. Jones, and F. Calle-Vallejo, “A New Type of Scaling Relations to Assess the Accuracy of Computational Predictions of Catalytic Activities Applied to the Oxygen Evolution Reaction,” *ChemCatChem*, vol. 9, no. 7, pp. 1261–1268, Apr. 2017, doi: 10.1002/cctc.201601662.
- [154] S. Deshpande, J. R. Kitchin, and V. Viswanathan, “Quantifying Uncertainty in Activity Volcano Relationships for Oxygen Reduction Reaction,” *ACS Catal.*, vol. 6, no. 8, pp. 5251–5259, 2016, doi: 10.1021/acscatal.6b00509.
- [155] W. L. Oberkampf and C. J. Roy, *Verification and Validation in Scientific Computing*. Cambridge: Cambridge University Press, 2010.

- [156] H. Wang and D. A. Sheen, “Combustion kinetic model uncertainty quantification, propagation and minimization,” *Prog. Energy Combust. Sci.*, vol. 47, pp. 1–31, Apr. 2015, doi: 10.1016/j.pecs.2014.10.002.
- [157] M. F. Bugallo, V. Elvira, L. Martino, D. Luengo, J. Miguez, and P. M. Djuric, “Adaptive Importance Sampling: The past, the present, and the future,” *IEEE Signal Process. Mag.*, vol. 34, no. 4, pp. 60–79, Jul. 2017, doi: 10.1109/MSP.2017.2699226.
- [158] S. H. Lee and W. Chen, “A comparative study of uncertainty propagation methods for black-box-type problems,” *Struct. Multidiscip. Optim.*, vol. 37, no. 3, pp. 239–253, 2009, doi: 10.1007/s00158-008-0234-7.
- [159] M. Iskandarani, S. Wang, A. Srinivasan, W. Carlisle Thacker, J. Winokur, and O. M. Knio, “An overview of uncertainty quantification techniques with application to oceanic and oil-spill simulations,” *J. Geophys. Res. Ocean.*, vol. 121, no. 4, pp. 2789–2808, Apr. 2016, doi: 10.1002/2015JC011366.
- [160] L. Cai and H. Pitsch, “Mechanism optimization based on reaction rate rules,” *Combust. Flame*, vol. 161, no. 2, pp. 405–415, 2014, doi: 10.1016/j.combustflame.2013.08.024.
- [161] N. Wiener, “The Homogeneous Chaos,” *Am. J. Math.*, vol. 60, no. 4, p. 897, Oct. 1938, doi: 10.2307/2371268.
- [162] D. Xiu and G. E. Karniadakis, “The Wiener--Askey Polynomial Chaos for Stochastic Differential Equations,” *SIAM J. Sci. Comput.*, vol. 24, no. 2, pp. 619–644, Jan. 2002, doi: 10.1137/S1064827501387826.
- [163] R. H. Cameron and W. T. Martin, “The Orthogonal Development of Non-Linear Functionals in Series of Fourier-Hermite Functionals,” *Ann. Math.*, vol. 48, no. 2, p. 385, Apr. 1947, doi: 10.2307/1969178.
- [164] M. I. Sobol’, “On sensitivity estimation for nonlinear mathematical models,” *Mat. Model.*, vol. 2, no. 1, pp. 112–118, 1990.
- [165] G. Li, C. Rosenthal, and H. Rabitz, “High Dimensional Model Representations,” *J. Phys. Chem. A*, vol. 105, no. 33, pp. 7765–7777, Aug. 2001, doi: 10.1021/jp010450t.

- [166] M. T. Reagan, H. N. Najm, B. J. Debusschere, O. P. Le Maître, O. M. Knio, and R. G. Ghanem, “Spectral stochastic uncertainty quantification in chemical systems,” *Combust. Theory Model.*, vol. 8, no. 3, pp. 607–632, Sep. 2004, doi: 10.1088/1364-7830/8/3/010.
- [167] S. G. Davis, A. B. Mhadeshwar, D. G. Vlachos, and H. Wang, “A new approach to response surface development for detailed gas-phase and surface reaction kinetic model optimization,” *Int. J. Chem. Kinet.*, vol. 36, no. 2, pp. 94–106, 2003, doi: 10.1002/kin.10177.
- [168] M. Frenklach, “Systematic optimization of a detailed kinetic model using a methane ignition example,” *Combust. Flame*, vol. 58, no. 1, pp. 69–72, Oct. 1984, doi: 10.1016/0010-2180(84)90079-8.
- [169] I. G. Zsély, J. Zádor, and T. Turányi, “Uncertainty analysis of updated hydrogen and carbon monoxide oxidation mechanisms,” *Proc. Combust. Inst.*, vol. 30, no. 1, pp. 1273–1281, Jan. 2005, doi: 10.1016/j.proci.2004.08.172.
- [170] L. Biegler *et al.*, *Large-Scale Inverse Problems and Quantification of Uncertainty*. Wiley, 2010.
- [171] N. Metropolis, A. W. Rosenbluth, M. N. Rosenbluth, A. H. Teller, and E. Teller, “Equation of State Calculations by Fast Computing Machines,” *J. Chem. Phys.*, vol. 21, no. 6, pp. 1087–1092, Jun. 1953, doi: 10.1063/1.1699114.
- [172] W. K. Hastings, “Monte Carlo sampling methods using Markov chains and their applications,” *Biometrika*, vol. 57, no. 1, pp. 97–109, Apr. 1970, doi: 10.1093/biomet/57.1.97.
- [173] C. P. Robert, “Monte Carlo statistical methods.” 2004.
- [174] R. Feeley, M. Frenklach, M. Onsum, T. Russi, A. Arkin, and A. Packard, “Model Discrimination Using Data Collaboration †,” *J. Phys. Chem. A*, vol. 110, no. 21, pp. 6803–6813, Jun. 2006, doi: 10.1021/jp056309s.
- [175] P. Seiler, M. Frenklach, A. Packard, and R. Feeley, “Numerical approaches for collaborative data processing,” *Optim. Eng.*, vol. 7, no. 4, pp. 459–478, Dec. 2006, doi: 10.1007/s11081-006-0350-4.

- [176] J. Bergstra, R. Bardenet, Y. Bengio, and B. Kégl, “Algorithms for hyper-parameter optimization,” in *NIPS Workshop on Bayesian optimization*, 2011, vol. 29, pp. 2546–2554.
- [177] F. Madrigal, C. Maurice, and F. Lerasle, “Hyper-parameter optimization tools comparison for multiple object tracking applications,” *Mach. Vis. Appl.*, vol. 30, no. 2, pp. 269–289, Mar. 2019, doi: 10.1007/s00138-018-0984-1.
- [178] A. S. Abbott, J. M. Turney, B. Zhang, D. G. A. Smith, D. Altarawy, and H. F. Schaefer, “PES-Learn: An Open-Source Software Package for the Automated Generation of Machine Learning Models of Molecular Potential Energy Surfaces,” *J. Chem. Theory Comput.*, vol. 15, no. 8, pp. 4386–4398, Aug. 2019, doi: 10.1021/acs.jctc.9b00312.
- [179] J. N. Wei, D. Duvenaud, and A. Aspuru-Guzik, “Neural Networks for the Prediction of Organic Chemistry Reactions,” *ACS Cent. Sci.*, vol. 2, no. 10, pp. 725–732, Oct. 2016, doi: 10.1021/acscentsci.6b00219.
- [180] A. Nandy, C. Duan, J. P. Janet, S. Gugler, and H. J. Kulik, “Strategies and Software for Machine Learning Accelerated Discovery in Transition Metal Chemistry,” *Ind. Eng. Chem. Res.*, vol. 57, no. 42, pp. 13973–13986, Oct. 2018, doi: 10.1021/acs.iecr.8b04015.
- [181] D. Rappoport and A. Aspuru-Guzik, “Predicting Feasible Organic Reaction Pathways Using Heuristically Aided Quantum Chemistry,” *J. Chem. Theory Comput.*, vol. 15, no. 7, pp. 4099–4112, Jul. 2019, doi: 10.1021/acs.jctc.9b00126.
- [182] V. M. B. Crisostomo *et al.*, “New Synthetic Route, Characterization, and Electrocatalytic Activity of Nanosized Manganite,” *Chem. Mater.*, vol. 19, no. 7, pp. 1832–1839, Apr. 2007, doi: 10.1021/cm062871z.
- [183] X. Cao *et al.*, “A novel non-enzymatic hydrogen peroxide biosensor based on ultralong manganite MnOOH nanowires,” *Sensors Actuators B Chem.*, vol. 147, no. 2, pp. 730–734, Jun. 2010, doi: 10.1016/j.snb.2010.03.087.
- [184] G. Kresse and J. Furthmüller, “Efficient iterative schemes for ab initio total-energy calculations using a plane-wave basis set,” *Phys. Rev. B*, vol. 54, no. 16, pp. 11169–

- 11186, Oct. 1996, doi: 10.1103/PhysRevB.54.11169.
- [185] P. E. Blöchl, “Projector augmented-wave method,” *Phys. Rev. B*, vol. 50, no. 24, pp. 17953–17979, Dec. 1994, doi: 10.1103/PhysRevB.50.17953.
- [186] E. Cockayne, I. Levin, H. Wu, and A. Llobet, “The magnetic structure of bixbyite  $\alpha$ -Mn<sub>2</sub>O<sub>3</sub>: A combined density functional theory DFT +U and neutron diffraction study,” *Phys. Rev. B*, vol. 87, no. 18, p. 184413, May 2013, doi: 10.1103/PhysRevB.87.184413.
- [187] S. Geller, “Structure of  $\alpha$ -Mn<sub>2</sub>O<sub>3</sub>, (Mn<sub>0.983</sub>Fe<sub>0.017</sub>)<sub>2</sub>O<sub>3</sub> and (Mn<sub>0.37</sub>Fe<sub>0.63</sub>)<sub>2</sub>O<sub>3</sub> and relation to magnetic ordering,” *Acta Crystallogr. Sect. B Struct. Crystallogr. Cryst. Chem.*, vol. 27, no. 4, pp. 821–828, Apr. 1971, doi: 10.1107/S0567740871002966.
- [188] T. Kohler, T. Armbruster, and E. Libowitzky, “Hydrogen Bonding and Jahn–Teller Distortion in Groutite, $\alpha$ -MnOOH, and Manganite, $\gamma$ -MnOOH, and Their Relations to the Manganese Dioxides Ramsdellite and Pyrolusite,” *J. Solid State Chem.*, vol. 133, no. 2, pp. 486–500, Nov. 1997, doi: 10.1006/jssc.1997.7516.
- [189] C. Franchini, R. Podloucky, J. Paier, M. Marsman, and G. Kresse, “Ground-state properties of multivalent manganese oxides: Density functional and hybrid density functional calculations,” *Phys. Rev. B*, vol. 75, no. 19, p. 195128, May 2007, doi: 10.1103/PhysRevB.75.195128.
- [190] C. W. M. Castleton, J. Kullgren, and K. Hermansson, “Tuning LDA+U for electron localization and structure at oxygen vacancies in ceria,” *J. Chem. Phys.*, vol. 127, no. 24, p. 244704, Dec. 2007, doi: 10.1063/1.2800015.
- [191] J. L. F. Da Silva, M. V. Ganduglia-Pirovano, J. Sauer, V. Bayer, and G. Kresse, “Hybrid functionals applied to rare-earth oxides: The example of ceria,” *Phys. Rev. B*, vol. 75, no. 4, p. 045121, Jan. 2007, doi: 10.1103/PhysRevB.75.045121.
- [192] M. Stöhr, T. Van Voorhis, and A. Tkatchenko, “Theory and practice of modeling van der Waals interactions in electronic-structure calculations,” *Chem. Soc. Rev.*, vol. 48, no. 15, pp. 4118–4154, 2019, doi: 10.1039/C9CS00060G.
- [193] K. Berland *et al.*, “van der Waals forces in density functional theory: a review of the

- vdW-DF method,” *Reports Prog. Phys.*, vol. 78, no. 6, p. 066501, Jun. 2015, doi: 10.1088/0034-4885/78/6/066501.
- [194] R. Christensen, H. A. Hansen, C. F. Dickens, J. K. Nørskov, and T. Vegge, “Functional Independent Scaling Relation for ORR/OER Catalysts,” *J. Phys. Chem. C*, vol. 120, no. 43, pp. 24910–24916, Nov. 2016, doi: 10.1021/acs.jpcc.6b09141.
- [195] D. S. Sholl and J. A. Steckel, *Density Functional Theory*. Hoboken, NJ, USA: John Wiley & Sons, Inc., 2009.
- [196] I. Chorkendorff and J. W. Niemantsverdriet, *Concepts of Modern Catalysis and Kinetics, 3rd Edition*. Wiley-VCH Verlag, 2017.
- [197] M. Frisch *et al.*, “Gaussian 09 Revision D. 01,” 2014.
- [198] V. A. Nikitina *et al.*, “ORR on Simple Manganese Oxides: Molecular-Level Factors Determining Reaction Mechanisms and Electrocatalytic Activity,” *J. Electrochem. Soc.*, vol. 165, no. 15, pp. J3199–J3208, Oct. 2018, doi: 10.1149/2.0261815jes.
- [199] A. S. Ryabova *et al.*, “Study of Hydrogen Peroxide Reactions on Manganese Oxides as a Tool To Decode the Oxygen Reduction Reaction Mechanism,” *ChemElectroChem*, vol. 3, no. 10, pp. 1667–1677, Oct. 2016, doi: 10.1002/celec.201600236.
- [200] Y. Gorlin and T. F. Jaramillo, “Investigation of Surface Oxidation Processes on Manganese Oxide Electrocatalysts Using Electrochemical Methods and Ex Situ X-ray Photoelectron Spectroscopy,” *J. Electrochem. Soc.*, vol. 159, no. 10, pp. H782–H786, Jan. 2012, doi: 10.1149/2.017210jes.
- [201] H.-Y. Su *et al.*, “Identifying active surface phases for metal oxide electrocatalysts: a study of manganese oxide bi-functional catalysts for oxygen reduction and water oxidation catalysis,” *Phys. Chem. Chem. Phys.*, vol. 14, no. 40, p. 14010, 2012, doi: 10.1039/c2cp40841d.
- [202] V. Viswanathan, H. A. Hansen, J. Rossmeisl, and J. K. Nørskov, “Universality in Oxygen Reduction Electrocatalysis on Metal Surfaces,” *ACS Catal.*, vol. 2, no. 8, pp. 1654–1660, Aug. 2012, doi: 10.1021/cs300227s.
- [203] K. S. Exner and H. Over, “Kinetics of Electrocatalytic Reactions from First-

- Principles: A Critical Comparison with the Ab Initio Thermodynamics Approach,” *Acc. Chem. Res.*, vol. 50, no. 5, pp. 1240–1247, May 2017, doi: 10.1021/acs.accounts.7b00077.
- [204] J. P. McClure, O. Borodin, M. Olguin, D. Chu, and P. S. Fedkiw, “Sensitivity of Density Functional Theory Methodology for Oxygen Reduction Reaction Predictions on Fe–N<sub>4</sub>-Containing Graphitic Clusters,” *J. Phys. Chem. C*, vol. 120, no. 50, pp. 28545–28562, Dec. 2016, doi: 10.1021/acs.jpcc.6b08498.
- [205] A. Ignaczak *et al.*, “Oxygen Reduction in Alkaline Media—a Discussion,” *Electrocatalysis*, vol. 8, no. 6, pp. 554–564, Nov. 2017, doi: 10.1007/s12678-017-0365-y.
- [206] A. Ignaczak *et al.*, “A scenario for oxygen reduction in alkaline media,” *Nano Energy*, vol. 26, pp. 558–564, Aug. 2016, doi: 10.1016/j.nanoen.2016.06.001.
- [207] C. Zhang, F.-R. F. Fan, and A. J. Bard, “Electrochemistry of Oxygen in Concentrated NaOH Solutions: Solubility, Diffusion Coefficients, and Superoxide Formation,” *J. Am. Chem. Soc.*, vol. 131, no. 1, pp. 177–181, Jan. 2009, doi: 10.1021/ja8064254.
- [208] M. Hayyan, M. A. Hashim, and I. M. AlNashef, “Superoxide Ion: Generation and Chemical Implications,” *Chem. Rev.*, vol. 116, no. 5, pp. 3029–3085, Mar. 2016, doi: 10.1021/acs.chemrev.5b00407.
- [209] M. V. Lebedeva *et al.*, “Effect of the chemical order on the electrocatalytic activity of model PtCo electrodes in the oxygen reduction reaction,” *Electrochim. Acta*, vol. 108, pp. 605–616, Oct. 2013, doi: 10.1016/j.electacta.2013.07.038.
- [210] R. R. Nazmutdinov, M. D. Bronshtein, T. T. Zinkicheva, and D. V. Glukhov, “Modeling of electron transfer across electrochemical interfaces: State-of-the art and challenges for quantum and computational chemistry,” *Int. J. Quantum Chem.*, vol. 116, no. 3, pp. 189–201, Feb. 2016, doi: 10.1002/qua.25035.
- [211] Y. Cui, X. Shao, M. Baldofski, J. Sauer, N. Nilius, and H.-J. Freund, “Adsorption, Activation, and Dissociation of Oxygen on Doped Oxides,” *Angew. Chemie Int. Ed.*, vol. 52, no. 43, pp. 11385–11387, Oct. 2013, doi: 10.1002/anie.201305119.

- [212] D. Halwidl *et al.*, “A full monolayer of superoxide: oxygen activation on the unmodified Ca<sub>3</sub>Ru<sub>2</sub>O<sub>7</sub> (001) surface,” *J. Mater. Chem. A*, vol. 6, no. 14, pp. 5703–5713, 2018, doi: 10.1039/C8TA00265G.
- [213] X. Wang, J. S. Lee, Q. Zhu, J. Liu, Y. Wang, and S. Dai, “Ammonia-Treated Ordered Mesoporous Carbons as Catalytic Materials for Oxygen Reduction Reaction,” *Chem. Mater.*, vol. 22, no. 7, pp. 2178–2180, Apr. 2010, doi: 10.1021/cm100139d.
- [214] J. T. Mefford *et al.*, “Water electrolysis on La<sub>1-x</sub>Sr<sub>x</sub>CoO<sub>3-δ</sub> perovskite electrocatalysts,” *Nat. Commun.*, vol. 7, no. 1, p. 11053, Apr. 2016, doi: 10.1038/ncomms11053.
- [215] W. G. Hardin, D. A. Slanac, X. Wang, S. Dai, K. P. Johnston, and K. J. Stevenson, “Highly Active, Nonprecious Metal Perovskite Electrocatalysts for Bifunctional Metal–Air Battery Electrodes,” *J. Phys. Chem. Lett.*, vol. 4, no. 8, pp. 1254–1259, Apr. 2013, doi: 10.1021/jz400595z.
- [216] W. G. Hardin *et al.*, “Tuning the Electrocatalytic Activity of Perovskites through Active Site Variation and Support Interactions,” *Chem. Mater.*, vol. 26, no. 11, pp. 3368–3376, Jun. 2014, doi: 10.1021/cm403785q.
- [217] J. T. Mefford, W. G. Hardin, S. Dai, K. P. Johnston, and K. J. Stevenson, “Anion charge storage through oxygen intercalation in LaMnO<sub>3</sub> perovskite pseudocapacitor electrodes,” *Nat. Mater.*, vol. 13, no. 7, pp. 726–732, Jul. 2014, doi: 10.1038/nmat4000.
- [218] J. T. Mefford *et al.*, “Decoupling the roles of carbon and metal oxides on the electrocatalytic reduction of oxygen on La<sub>1-x</sub>Sr<sub>x</sub>CoO<sub>3-δ</sub> perovskite composite electrodes,” *Phys. Chem. Chem. Phys.*, vol. 21, no. 6, pp. 3327–3338, 2019, doi: 10.1039/C8CP06268D.
- [219] F. Calle-Vallejo, J. I. Martínez, J. M. García-Lastra, M. Mogensen, and J. Rossmeisl, “Trends in Stability of Perovskite Oxides,” *Angew. Chemie Int. Ed.*, vol. 49, no. 42, pp. 7699–7701, Oct. 2010, doi: 10.1002/anie.201002301.
- [220] X. Rong, J. Parolin, and A. M. Kolpak, “A Fundamental Relationship between

- Reaction Mechanism and Stability in Metal Oxide Catalysts for Oxygen Evolution,” *ACS Catal.*, vol. 6, no. 2, pp. 1153–1158, Feb. 2016, doi: 10.1021/acscatal.5b02432.
- [221] E. Fabbri, R. Mohamed, P. Levecque, O. Conrad, R. Kötz, and T. J. Schmidt, “Composite Electrode Boosts the Activity of Ba<sub>0.5</sub>Sr<sub>0.5</sub>Co<sub>0.8</sub>Fe<sub>0.2</sub>O<sub>3-δ</sub> Perovskite and Carbon toward Oxygen Reduction in Alkaline Media,” *ACS Catal.*, vol. 4, no. 4, pp. 1061–1070, Apr. 2014, doi: 10.1021/cs400903k.
- [222] V. Hermann, D. Dutriat, S. Müller, and C. Comninellis, “Mechanistic studies of oxygen reduction at La<sub>0.6</sub>Ca<sub>0.4</sub>CoO<sub>3</sub>-activated carbon electrodes in a channel flow cell,” *Electrochim. Acta*, vol. 46, no. 2–3, pp. 365–372, Nov. 2000, doi: 10.1016/S0013-4686(00)00593-4.
- [223] G. Kéranguéven, S. Royer, and E. Savinova, “Synthesis of efficient Vulcan–LaMnO<sub>3</sub> perovskite nanocomposite for the oxygen reduction reaction,” *Electrochem. commun.*, vol. 50, pp. 28–31, Jan. 2015, doi: 10.1016/j.elecom.2014.10.019.
- [224] S. Malkhandi, B. Yang, A. K. Manohar, A. Manivannan, G. K. S. Prakash, and S. R. Narayanan, “Electrocatalytic Properties of Nanocrystalline Calcium-Doped Lanthanum Cobalt Oxide for Bifunctional Oxygen Electrodes,” *J. Phys. Chem. Lett.*, vol. 3, no. 8, pp. 967–972, Apr. 2012, doi: 10.1021/jz300181a.
- [225] Y. Shimizu, K. Uemura, H. Matsuda, N. Miura, and N. Yamazoe, “Bi-Functional Oxygen Electrode Using Large Surface Area La<sub>1-x</sub>Ca<sub>x</sub>CoO<sub>3</sub> for Rechargeable Metal-Air Battery,” *J. Electrochem. Soc.*, vol. 137, no. 11, pp. 3430–3433, Nov. 1990, doi: 10.1149/1.2086234.
- [226] Z.-L. Wang, D. Xu, J.-J. Xu, and X.-B. Zhang, “Oxygen electrocatalysts in metal–air batteries: from aqueous to nonaqueous electrolytes,” *Chem. Soc. Rev.*, vol. 43, no. 22, pp. 7746–7786, 2014, doi: 10.1039/C3CS60248F.
- [227] Y. Wang and H.-P. Cheng, “Oxygen Reduction Activity on Perovskite Oxide Surfaces: A Comparative First-Principles Study of LaMnO<sub>3</sub>, LaFeO<sub>3</sub>, and LaCrO<sub>3</sub>,” *J. Phys. Chem. C*, vol. 117, no. 5, pp. 2106–2112, Feb. 2013, doi: 10.1021/jp309203k.

- [228] W. C. Conner and J. L. Falconer, “Spillover in Heterogeneous Catalysis,” *Chem. Rev.*, vol. 95, no. 3, pp. 759–788, May 1995, doi: 10.1021/cr00035a014.
- [229] J. J. Moré, B. S. Garbow, and K. E. Hillstrom, “User guide for MINPACK-1,” ANL-80-74, CM-P00068642, 1980.
- [230] J. Bergstra, B. Komer, C. Eliasmith, D. Yamins, and D. D. Cox, “Hyperopt: a Python library for model selection and hyperparameter optimization,” *Comput. Sci. Discov.*, vol. 8, no. 1, p. 014008, Jul. 2015, doi: 10.1088/1749-4699/8/1/014008.
- [231] R.E. Davis, G.L. Horvath, and C.W. Tobias, “The solubility and diffusion coefficient of oxygen in potassium hydroxide solutions,” *Electrochim. Acta*, vol. 12, no. May 1965, pp. 287–297, 1967.
- [232] G. P. López, D. G. Castner, and B. D. Ratner, “XPS O 1s binding energies for polymers containing hydroxyl, ether, ketone and ester groups,” *Surf. Interface Anal.*, vol. 17, no. 5, pp. 267–272, May 1991, doi: 10.1002/sia.740170508.
- [233] D. G. Truhlar, B. C. Garrett, and S. J. Klippenstein, “Current Status of Transition-State Theory,” *J. Phys. Chem.*, vol. 100, no. 31, pp. 12771–12800, Jan. 1996, doi: 10.1021/jp953748q.
- [234] A. A. Kurilovich, C. T. Alexander, E. M. Pazhetnov, and K. J. Stevenson, “Active learning-based framework for optimal reaction mechanism selection from microkinetic modeling: a case study of electrocatalytic oxygen reduction reaction on carbon nanotubes,” *Phys. Chem. Chem. Phys.*, vol. 22, no. 8, pp. 4581–4591, 2020, doi: 10.1039/C9CP06190H.
- [235] M. Frenklach, A. Packard, P. Seiler, and R. Feeley, “Collaborative data processing in developing predictive models of complex reaction systems,” *Int. J. Chem. Kinet.*, vol. 36, no. 1, pp. 57–66, 2004, doi: 10.1002/kin.10172.
- [236] Z. Zhang, J. Liu, J. Gu, L. Su, and L. Cheng, “An overview of metal oxide materials as electrocatalysts and supports for polymer electrolyte fuel cells,” *Energy Environ. Sci.*, vol. 7, no. 8, pp. 2535–2558, Jan. 2014, doi: 10.1039/C3EE43886D.